NUMERICAL MODELING OF SPECIES TRANSPORT IN TURBULENT FLOW AND EXPERIMENTAL STUDY ON AEROSOL SAMPLING

A Dissertation

by

VISHNU KARTHIK VIJAYARAGHAVAN

Submitted to the Office of Graduate Studies of
Texas A&M University
in partial fulfillment of the requirements for the degree of

DOCTOR OF PHILOSOPHY

December 2006

Major Subject: Mechanical Engineering

NUMERICAL MODELING OF SPECIES TRANSPORT IN TURBULENT FLOW AND EXPERIMENTAL STUDY ON AEROSOL SAMPLING

A Dissertation

by

VISHNU KARTHIK VIJAYARAGHAVAN

Submitted to the Office of Graduate Studies of
Texas A&M University
in partial fulfillment of the requirements for the degree of

DOCTOR OF PHILOSOPHY

Approved by:

Co-Chairs of Committee,	Andrew R. McFarland
	Yassin A. Hassan
Committee Members,	John S. Haglund
	Sharath Girimaji
Head of Department,	Dennis O'Neal

December 2006

Major Subject: Mechanical Engineering

ABSTRACT

Numerical Modeling of Species Transport in Turbulent Flow and Experimental Study on Aerosol Sampling. (December 2006)

Vishnu Karthik Vijayaraghavan, B.Tech., Indian Institute of Technology, Madras, India;

M.S., Texas A&M University

Co-Chairs of Advisory Committee: Dr. A. R. McFarland
Dr. Y. A. Hassan

Numerical simulations were performed to study the turbulent mixing of a scalar species in straight tube, single and double elbow flow configurations. Different Reynolds Averaged Navier Stokes (RANS) and Large Eddy Simulation (LES) models were used to model the turbulence in the flow. Conventional and dynamic Smagorinsky sub-grid scale models were used for the LES simulations. Wall functions were used to resolve the near wall boundary layer. These simulations were run with both two-dimensional and three-dimensional geometries. The velocity and tracer gas concentration Coefficient of Variations were compared with experimental results. The results from the LES simulations compared better with experimental results than the results from the RANS simulations. The level of mixing downstream of a S-shaped double elbow was higher than either the single elbow or the U-shaped double elbow due to the presence of counter rotating vortices. Penetration of neutralized and non-neutralized aerosol particles through three different types of tubing was studied. The tubing used included standard PVC pipes, aluminum conduit and flexible vacuum hose. Penetration through the

aluminum conduit was unaffected by the presence or absence of charge neutralization, whereas particle penetrations through the PVC pipe and the flexible hosing were affected by the amount of particle charge. The electric field in a space enclosed by a solid conductor is zero. Therefore charged particles within the conducting aluminum conduit do not experience any force due to ambient electric fields, whereas the charged particles within the non-conducting PVC pipe and flexible hose experience forces due to the ambient electric fields. This increases the deposition of charged particles compared to neutralized particles within the 1.5" PVC tube and 1.5" flexible hose. Deposition 2001a (McFarland et al. 2001) software was used to predict the penetration through transport lines. The prediction from the software compared well with experiments for all cases except when charged particles were transported through non-conducting materials. A Stairmand cyclone was designed for filtering out large particles at the entrance of the transport section.

DEDICATION

To my parents.

ACKNOWLEDGEMENTS

I would like to thank Dr. A. R. McFarland for his constant guidance, motivation and support through every stage of my graduate life at Texas A&M University and Dr. Y. A. Hassan for his guidance and encouragement throughout my graduate studies. I wish to thank Dr. John Haglund for the many fruitful discussions and for his guidance. Dr. Girimaji's suggestions and insight into my research were very helpful and I want to thank him for that. I would like to thank Mr. Carlos Ortiz for guiding and helping me with my experimental studies. I would like to thank Dr. Sridhar Hari for his encouragement and motivation. Thanks to John Vaughn and Gary Bradley for their help with drawings. Thanks to all other members of the Aerosol Technology Laboratory for making the lab a cheerful and lively place to work in.

TABLE OF CONTENTS

Page

LIST OF FIGURES

FIGURE Page

FIGURE Page

FIGURE Page

FIGURE Page

FIGURE Page

FIGURE Page

FIGURE Page

LIST OF TABLES

TABLE Page

1. INTRODUCTION

The application under consideration for the present study is the single point representative sampling of effluents from nuclear stacks and ducts. The advantage of this approach to sampling is reduced deployment and maintenance costs due to the use of a single sampling transport system (sampling probe and associated flow components like the pump, flow meter, etc.) as opposed to multiple sampling transport systems that would be required for multipoint sampling. For single point sampling (Han et al. 2003) to be representative of the mean effluent concentration in the flow, the effluent has to be well mixed at the sampling location. The American National Standard (ANSI/HPS-N13.1-1999 1999) specifies the various requirements for single point sampling, including the requirement that the momentum, tracer gas concentration and 10 μm AD aerosol particle concentration should be relatively uniform at the sampling location. The effluent concentration will become uniform across the cross-section at long distances from the entrance of the effluent, but due to space constraints we may have to actively enhance the mixing, so that we can achieve suitable conditions for single point sampling in short ducts. To achieve uniformity of momentum, tracer gas and particle concentration various mixing elements such as a generic mixers (McFarland et al. 1999a), bends, static mixers (McFarland et al. 1999b), tee mixers (Han et al. 2005), etc. have been used.

This dissertation follows the style of *Health Physics Journal*.

The mixing element can be chosen based on the amount of mixing it achieves and the power requirements of the mixer. Ideally, we would like to decrease the pressure drop and therefore the power requirements and increase the mixing. When a mixing element achieves greater mixing usually the associated pressure loss across the mixing element is also higher. Therefore we need to choose the appropriate mixing element based on space and power constraints. Currently, the design of the flow system and the mixing elements is performed using experimental guidance (e.g. (Gupta et al. 1998), (Ramakrishna et al. 2001), (Rodgers et al. 1996)). Experiments, while often providing accurate results for the design criteria, can also be expensive and time consuming, especially when conducted in the field. Therefore if reliable models could be used to predict the mixing patterns of various mixing elements it would be of considerable value to the nuclear industry.

An objective of this study is to develop such models for the *a priori* prediction of mixing generated by different mixing elements. Such models can be developed using results from experiments conducted in the lab as well as those conducted in the field. To develop such models we require higher order statistics (e.g. skewness and kurtosis) and probability density functions of velocities and species concentration. Experimentally obtaining these quantities for different combinations of flow configurations and mixing elements is a prohibitively time consuming and expensive proposition. Therefore the approach that will be employed is to use Computational Fluid Dynamics (CFD) to solve the momentum and species transport equations and obtain the statistics for the species

mixing downstream of various mixing elements. The results from the numerical simulations will be compared with experimental results to validate the CFD simulations.

As we are predominantly dealing with turbulent flows, models need to be used to simulate the turbulence. Different modeling or solving approaches, such as Reynolds Averaged Navier-Stokes (RANS), Large Eddy Simulation (LES) or Direct Numerical Simulation (DNS) can be utilized. The numerical complexity increases from the RANS to the LES to DNS schemes. The feasibility of using RANS and LES schemes to model the turbulence in the flow through an elbow was analyzed in the current study. Water analog flow visualization experiments were conducted by introducing a dye into a turbulent water flow. The flow structures obtained from the visualization experiments will be compared to the turbulent structures and statistics obtained from the numerical simulations.

In addition to the requirement on the uniformity of the momentum and concentration at the sampling location, the standards specify requirements for the sampling transport system. One requirement is that the total transport of 10 µm AD particles and vapor contaminants shall be greater than 50% from the free stream to the collector or analyzer. A sampling transport system was designed and the effect of particle charge and transport line conductivity on particle transport was studied experimentally. The transport system was optimized to maximize the penetration of particles through it.

2. BACKGROUND AND THEORY

Solving momentum and scalar transport

The Navier–Stokes equations and the scalar transport equation are either averaged (RANS) or filtered (LES) to solve for the velocities and species concentration respectively (Biswas and Eswaran 2002). The scalar transport equation is a generic equation that can be applied to different scalars such as species concentration or temperature. The generic equation is given in Equation [2.1]:

$$\underbrace{\frac{\partial \rho\phi}{\partial t}}_{Transient\ \ term} + \underbrace{\nabla.\left(\rho\vec{u}\phi\right)}_{Convection\ \ term} = \underbrace{\nabla.\left(\Gamma\nabla\phi\right)}_{Diffusion\ \ term} + \underbrace{S_{\phi}}_{Source\ \ term} \qquad [2.1]$$

Depending on the constants, the equation can either be a species transport equation, heat transfer equation, etc. In the current study the focus was on species transport, though with minor modifications, the same study can be applied to equivalent heat transfer problems.

Subgrid scale modeling for LES

Results from static and dynamic Smagorinsky subgrid scale models are compared in the LES of flow through an elbow. The difference between the static and dynamic subgrid scale model lies in the calculation method for the Smagorinsky constant. The Smagorinsky constant relates the length scale to the filter width. The

characteristic length scale is used to calculate the eddy viscosity from the resolved strain rate magnitude. The static subgrid scale model assumes a uniform Smagorinsky constant throughout the domain, whereas, in the dynamic model, the Smagorinsky constant is calculated based on the local turbulence characteristics.

Calculation of near wall grid size

While using near wall modeling the node closest to the wall needs to have a y^+ value between 30 and 60 for the node to be in the log layer. We do not know the value of y^+ prior to solving the flow as it is a flow dependent parameter. Therefore we need to make a best estimate for the value of y^+. This estimate is based on the fully developed flow through a straight tube with a circular cross-section. The expression for wall shear stress, τ_w for a fully developed flow through a straight tube (Fox and McDonald 2001) for bulk flow Reynolds number, *Re* values less than 10^5 is given by equation [2.2].

$$\tau_w = 0.0332\rho V^2 \left(\frac{2\nu}{DV}\right)^{0.25} \qquad [2.2]$$

where v is the kinematic viscosity and D is the tube diameter. From equation [2.2] the expression given in equation [2.3] for the friction velocity, u can be obtained.

$$u_\tau = \sqrt{\frac{\tau_w}{\rho}} = 0.199V\,\mathrm{Re}^{0.125} \qquad [2.3]$$

Further from equation [2.3] the first grid cell size, y_{FC} in terms of the y^+ value can be obtained (equation [2.4]).

$$y_{FC} = \frac{y^+ \nu}{u_\tau} = \frac{y^+ D}{0.199\,\mathrm{Re}^{0.875}} \qquad [2.4]$$

Using equation [2.4], the first cell size can be estimated using a y^+ value between 30 and 60. As the analysis is based on the fully developed flow through a pipe, the y^+ value obtained after numerically solving the flow can be different from the assumed y^+ value. Therefore, once the flow is solved, we need to check for the y^+ values of the near wall cells. If the y^+ values do not lie between 30 and 60, then we will have to either refine the mesh if the y^+ value is greater than 60 or coarsen the mesh if the y^+ value is lesser than 30.

Measures for uniformity

The widely used measure for demonstrating the uniformity of momentum or concentration at a cross-section of the flow is the co-efficient of variation (COV). COV is defined as the standard deviation over the mean for a given set of data points.

$$COV = \frac{\text{Standard Deviation}}{\text{Mean}} \qquad [2.5]$$

Usually a discrete measure is used for COV. The formula for the discrete measure of COV is

$$COV = \frac{\sqrt{\frac{1}{N-1}\sum_{i=1}^{N}\left(x_i - \overline{x}\right)^2}}{\overline{x}} \qquad [2.6]$$

where $\overline{x}$ is the mean and N is the number of data points. Measurements used to calculate a COV are performed at a specified number of grid points in the duct cross section (perpendicular to the mean flow). Usually the measurement points are those suggested by EPA (U.S.EPA 2001). The cross-section is divided into N equal area sections. The measurement point is located at the centroid of these sections. Figure 2.1 shows examples of such a grid for both circular and rectangular cross-sections. The cross-section has been divided into 12 equal areas in the figures. For the experiments and numerical simulations while measuring the COV usually the center 12 points of a 16 point EPA grid are used. The outer points in the circular geometry ducts were not used, as accurate measurements at these points are hindered by their proximity to the wall, so in most situations, these points are excluded by ANSI in the calculation of COVs.

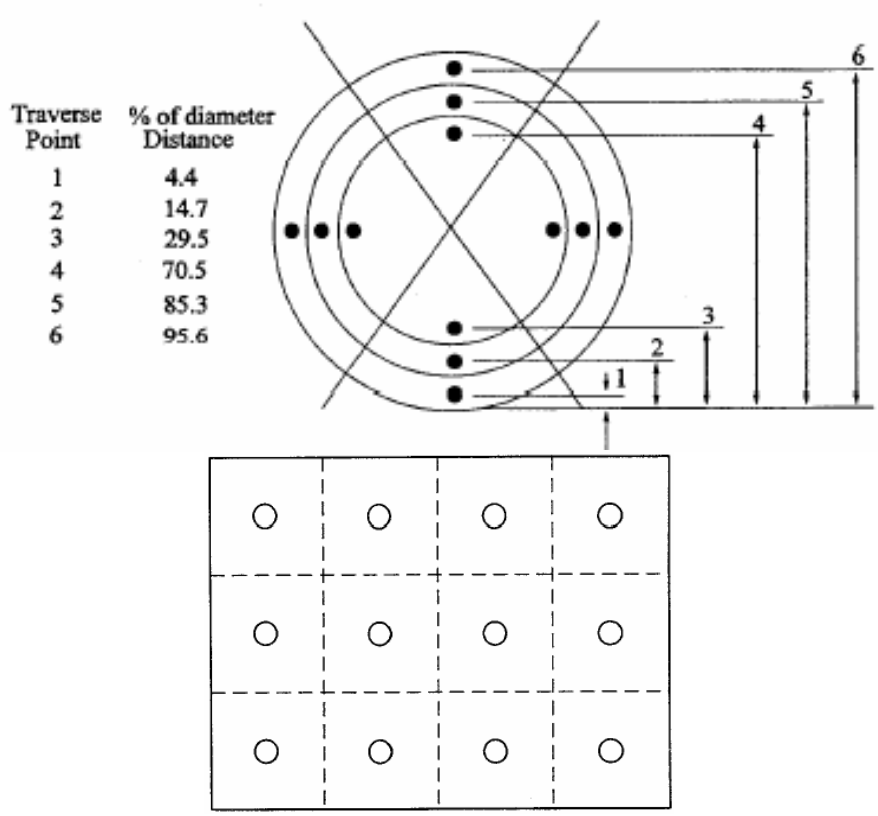

Figure 2.1: Example of circular and rectangular EPA grids.

While such a discrete measure is acceptable for fairly regular or symmetric flow, in the case of a highly irregular flow, the discrete metric might fail to capture the non-uniformity in the flow. For example, consider an axi-symmetric concentration profile such as the one shown in Figure 2.2. Though a COV measure based on the 12 point EPA grid indicates a fairly uniform profile, we know that in reality that the profile has a high degree of non-uniformity. One way to avoid this problem is to increase the number of grid points used for the calculation of the COV. In the limit, we can use an integral measure for the COV.

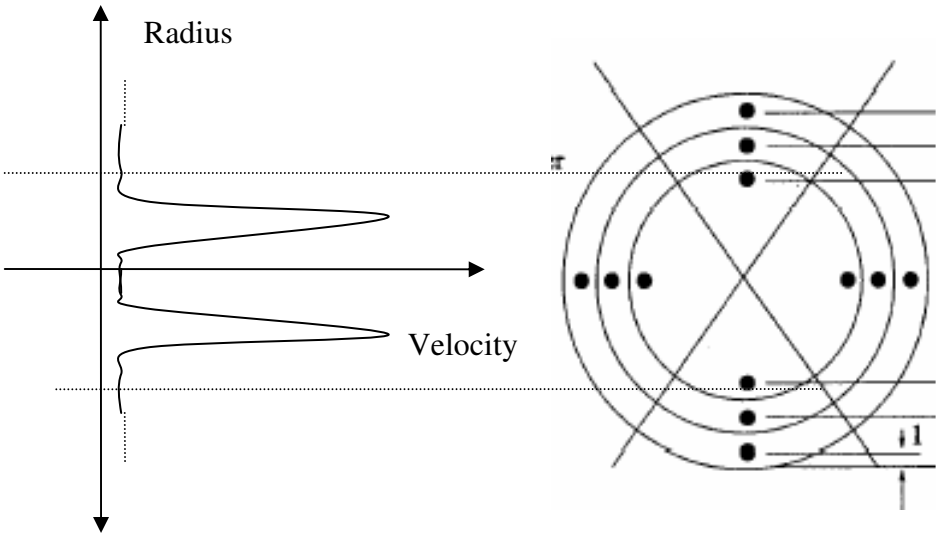

Figure 2.2: Example of a profile whose non-uniformity is not captured by a 12 point EPA grid.

The equation for the integral measure for COV is as follows:

$$COV = \frac{\sqrt{\frac{1}{A}\iint_S (x-\bar{x})^2 \, dA}}{\bar{x}}, \quad \text{mean}, \bar{x} = \frac{1}{A}\iint_S x dA \qquad [2.7]$$

where A is the area of the surface, S over which the COV is calculated and N is the number of data points. To illustrate the differences between the integral and discrete measure a hypothetical profile is chosen. The hypothetical profile chosen is an axi-symmetric profile with a normal distribution in the r direction. The mean and the standard deviation of the distribution are chosen as variables. In Figure 2.3a, the normal

distribution profile has a mean of 0.25 and the standard deviation of the profile is varied from 0.02 to 0.3.

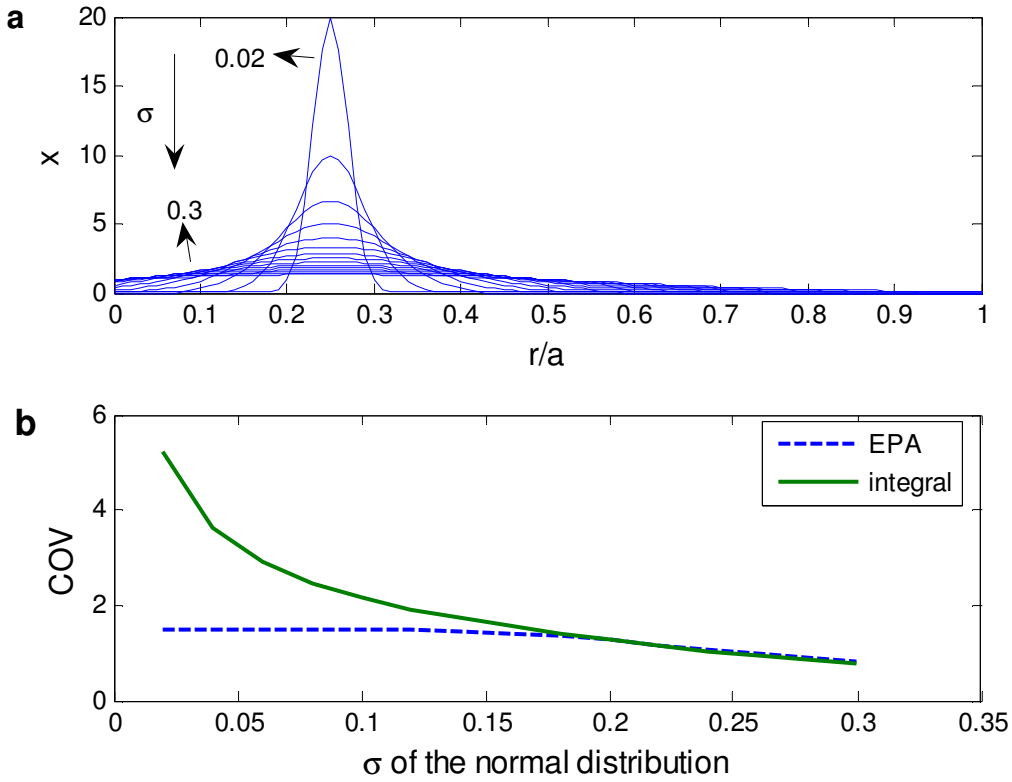

Figure 2.3: a.) The normal distribution has a mean of 0.25 and the standard deviation (σ) of the distribution is varied from 0.02 to 0.3; b.) The EPA and integral COVs are plotted as a function of the standard deviation of the normal distribution.

The EPA and integral COVs are plotted as a function of the standard deviation of the normal distribution in Figure 2.3b. The Simpson quadrature rule was used to numerically evaluate the integral COV. From a profile standard deviation of 0.02 to around 0.12 the EPA COV is constant and unable to capture the change in profile. The two measures of COV show a closer match after a profile standard deviation of around 0.18, at which point the COV is 135%.

Figure 2.4 is similar to Figure 2.3 except for the mean of the normal distribution that has been changed to 0.5 from the previous value of 0.25. From Figure 2.4b we can see that the EPA and integral COV curves match each other after a profile standard deviation of around 0.25. This value of the profile standard deviation corresponds to a COV value of around 0.6. We can conclude from these analyses that the discrete measure for COV cannot capture the change in profiles for extremely non-uniform profiles. After certain uniformity is achieved, the discrete and integral measures for COV follow the same trend.

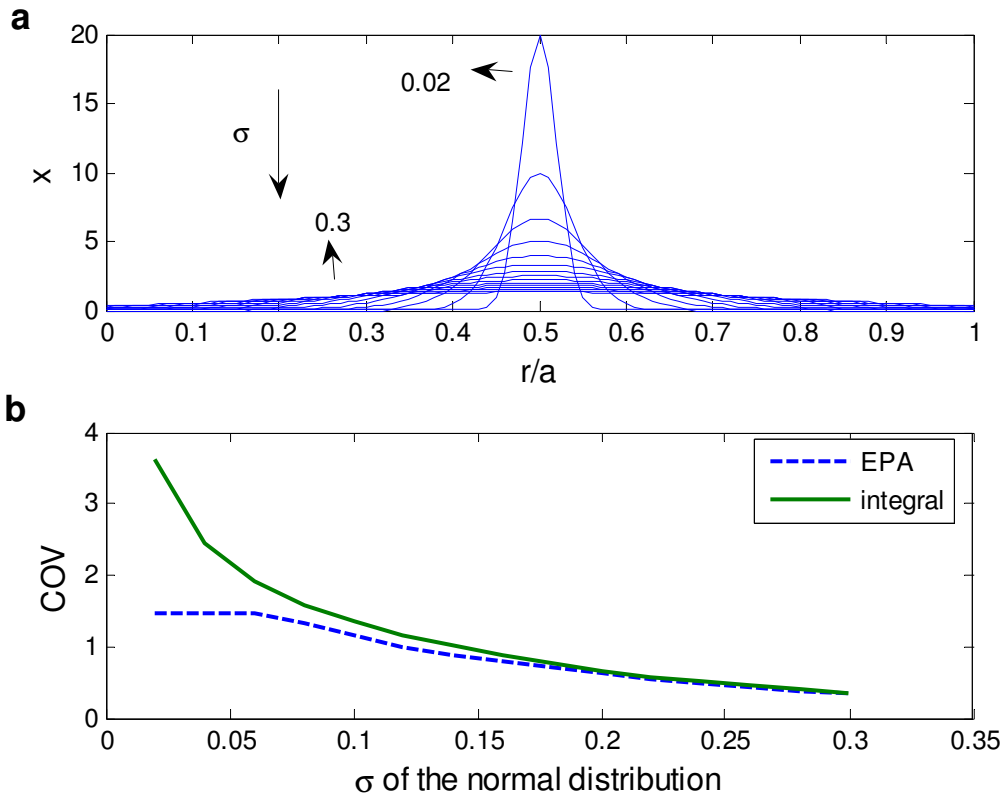

Figure 2.4: a.) The normal distribution has a mean of 0.5 and the standard deviation (σ) of the distribution is varied from 0.02 to 0.3; b.) The EPA and integral COVs are plotted as a function of the standard deviation of the normal distribution.

Figure 2.5 shows the COV of concentration plotted against the dimensionless distance downstream from the exit plane of a single elbow. Three different measures were used for calculating the COV, *viz.* integral measure, 12 point EPA grid and center 12 points of a 16 point EPA grid. However, the integral measure used is not a true integral measure based on Equation [2.7]. For simplicity, the projected areas of all the elements on a given surface are assumed to be equal. It can be seen from Figure 2.5 that while the integral measure of COV and the COV based on 12 point EPA grid

monotonically decrease, the measure based on the center 12 points of a 16 point EPA grid does not increase or decrease monotonically. The COV decreases in general except for the region where the L/D value varies between 5 and 7.

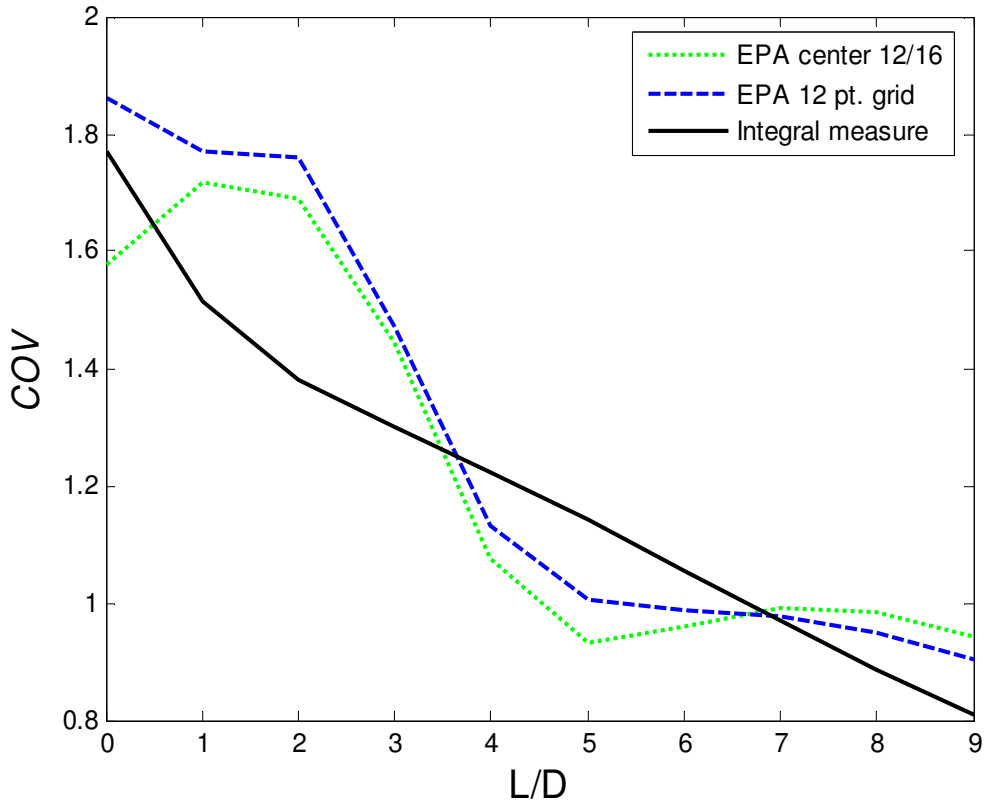

Figure 2.5: The COV of concentration downstream of a single elbow is plotted against the dimensionless distance downstream from the exit plane of the elbow.

In this region the COV increases, implying that the non-uniformity in the concentration across cross-section increases as the flow develops, while the integral

COV still decreases. Such an increase in the non-uniformity is highly unlikely considering that the convection is by the mean flow and not the instantaneous flow. Though the COV calculated using the 12 point EPA grid does not follow the same trend as the integral, it does monotonically decrease. Therefore, in comparison with the COV calculated using the center 12 points of a 16 point EPA grid, the COV calculated using a 12 point EPA grid has relatively better behavior. From this we can conclude that neglecting near wall sampling points leads to reduction in the quality of the measure for non-uniformity.

Predictive mixing

A predictive mixing model could be used to *a priori* estimate the level of mixing of gaseous tracers and 10 µm AD aerosol particles in different flow geometries. For this purpose, a model needs to be developed based on physical reasoning as well as correlations from experimental and numerical data. The different parameters upon which the mixing could depend are:

- Geometry of the flow path (e.g. in an elbow, the radius of curvature may be important)
- The kind of mixing elements present (e.g. a static mixer or a mixing chamber).
- Properties of the substance being mixed (i.e. viscosity, density, state of matter, etc.)

- The characteristic of the flow at the place where the contaminants are introduced (this will depend on how the flow is driven, e.g. by blowers, and also on what kind of flow conditioners are present)
- The degree of turbulence in the flow. In general the larger the amount of turbulence, the greater will be the mixing.

Gupta (1999) used experimental results to obtain a correlation for the coefficient of variation in a straight tube as a function of dimensionless downstream distance:

$$COV = 148.93e^{-0.0938(L/D)} \quad [2.8]$$

Any mixing element is replaced with an equivalent length of straight pipe that would produce the same degree of mixing as the original elements. For two elbows in series (either U- or S-configuration) the two consecutive elbows are replaced with an equivalent length of straight pipe and extra length of pipe is added to account for the interaction effect between the two elbows.

COV data from various studies on mixing were compiled and the data were fit with an exponential curve and a power law curve. It was seen that the exponential curve was a better fit in cases where there was low turbulence intensities just after the mixing element. In cases where there was high turbulence intensities just after the mixing element a power law profile seemed to fit the data much better. These profiles were used to model the development of velocity, tracer gas concentration and particle concentration

COVs downstream of a generic Tee-mixer (Han et al. 2005). The schematic of the generic Tee-mixer is shown in Figure 2.6.

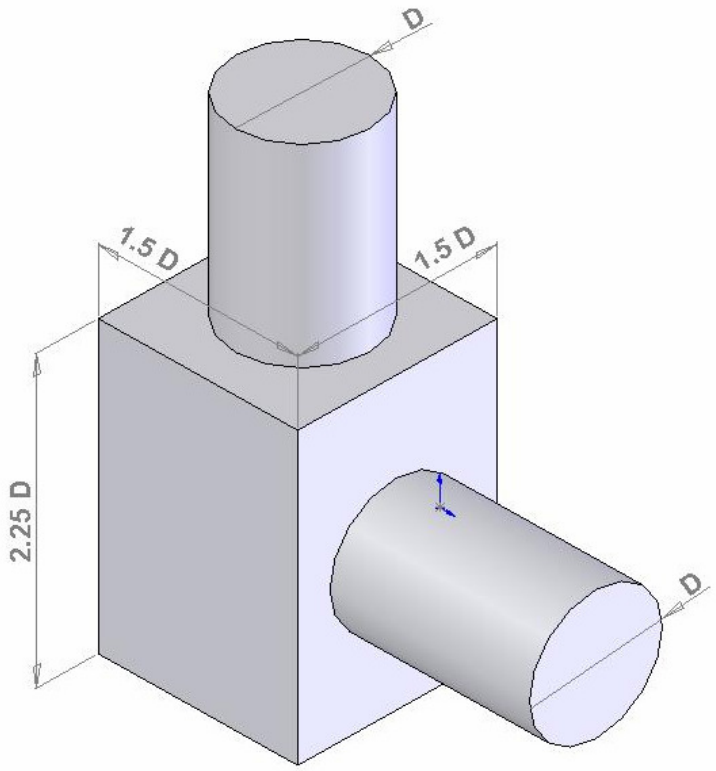

Figure 2.6: Schematic of a Tee-mixer.

The development of the COVs and the corresponding exponential and power law profiles are plotted in Figure 2.7. From the plots in Figure 2.7 it can be seen that for a Tee-mixer the power law and exponential profile fit the development of velocity COV equally well. The tracer gas and particle mixing show a pronounced power law behavior and the exponential profile does not fit the development of tracer gas and particle concentration COVs as well as the power law profile. The same conclusion can be reached by looking at the R^2 values for the two fits shown in Table 2.1. The R^2 value for the power law fit is 0.99 and 0.97 for the tracer gas concentration COV and particle concentration COV respectively. These values are closer to the ideal R^2 value of 1 than the R^2 values of 0.86 and 0.74 from the exponential fit for the tracer gas concentration COV and particle concentration COV respectively.

It can also be seen from Table 2.1 that in the case of a power law fit, the value of the exponent, b is very close to the value of -2/3 suggested in literature (Monclova and Forney 1995) for the development of COV of aerosol particle concentration after a Tee junction.

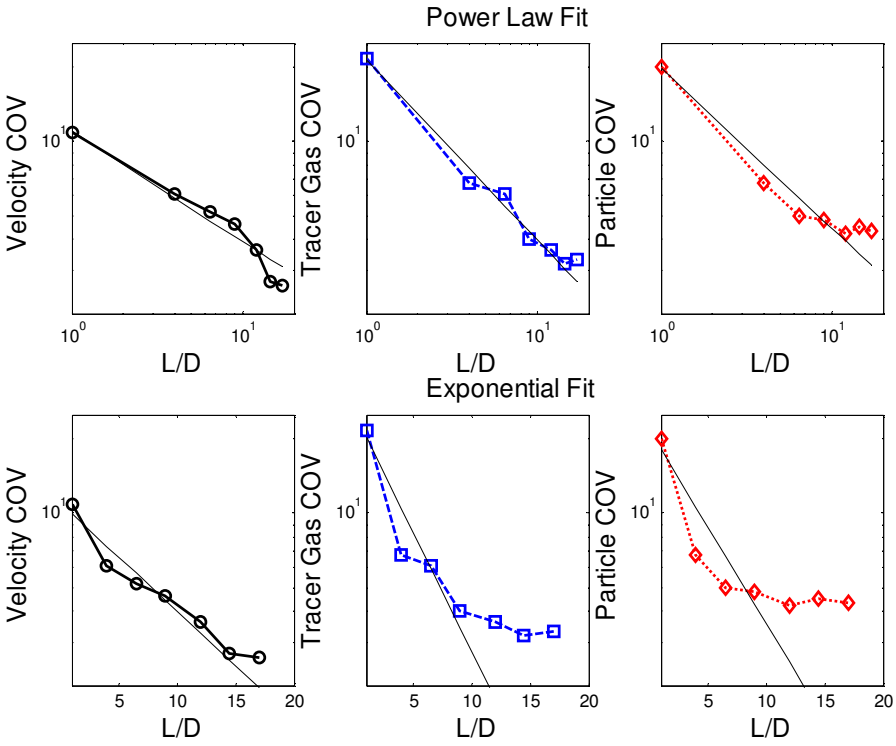

Figure 2.7: Velocity, tracer gas and particle COVs as a function of distance downstream of the Tee-mixer. Exponential and power law fits are plotted along with the experimental data.

Table 2.1: The coefficients and the adjusted-R^2 for exponential and power law fits.

COV	**Power Law Fit**			**Exponential Fit**		
	$COV = a(L/D)^b$		**Adjusted R^2**	**$COV = ae^{b(L/D)}$**		**Adjusted R^2**
	a	***b***		***A***	***b***	
Velocity	10.95	-0.4459	0.9716	11	-0.1011	0.9229
Tracer Gas	21.36	-0.7292	0.9914	25.14	-0.2213	0.8593
Particle	19.78	-0.6501	0.9713	21.68	-0.1805	0.7419

The plots in Figure 2.8 show the tracer gas concentration COVs as a function of the distance downstream of the entrance to the straight tube for three different inlet turbulent intensities, *viz.* 1.5%, 10% and 20% (Anand et al. 2003).

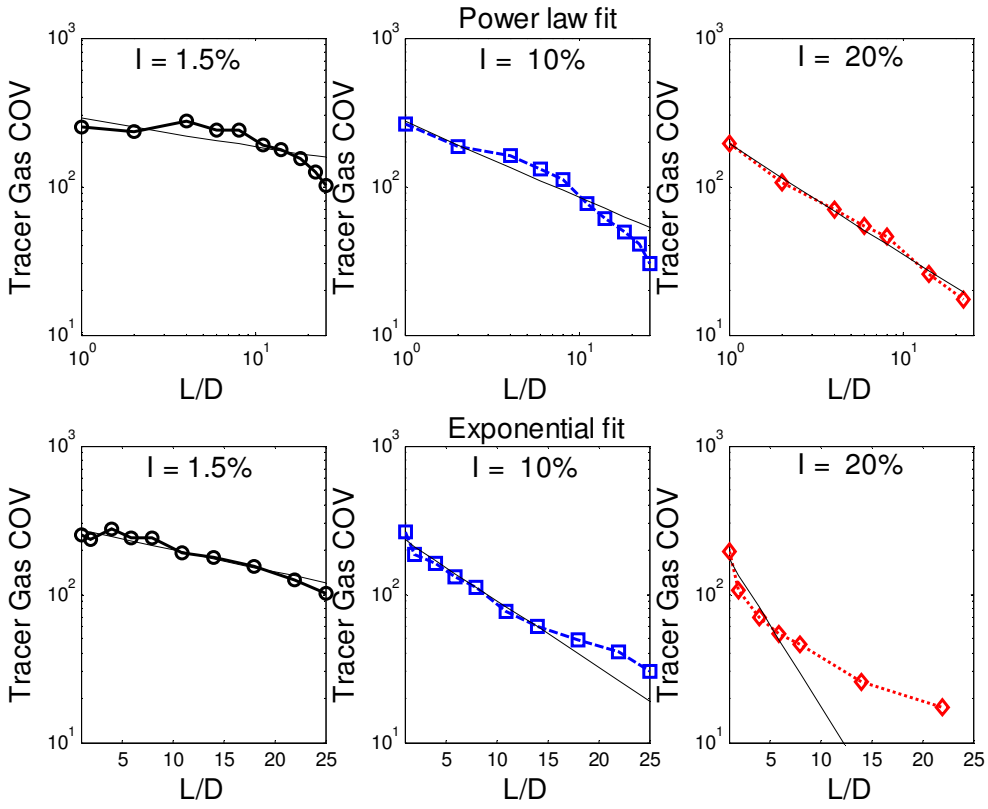

Figure 2.8: Tracer gas concentration COVs as a function of distance downstream of the tube entrance for different inlet turbulence intensities. Exponential and power law fits are plotted along with the experimental data.

The model coefficients and the adjusted R^2 values for the exponential and power law fit for the development of COVs in a straight tube has been tabulated in Table 2.2. We can see from the plots in Figure 2.8 and the adjusted R^2 in Table 2.2 that the exponential fit works somewhat better at lower turbulent intensities and the power law fit works better at higher turbulent intensities.

Table 2.2: The coefficients and adjusted-R^2 for the exponential and power law fits for tracer gas COVs downstream of the tube inlet for different inlet turbulence intensities.

COV	**Power Law Fit**			**Exponential Fit**		
	COV = a(L/D)^b		**Adjusted R^2**	**COV = ae$^{b(L/D)}$**		**Adjusted R^2**
	a	***b***		***A***	***b***	
I = 1.5%	284.9	-0.1868	0.5356	280.0	-0.034	0.8785
I = 10%	272.1	-0.5090	0.9425	257.9	-0.1041	0.9533
I = 20%	192.4	-0.7455	0.9932	222.7	-0.2523	0.8787

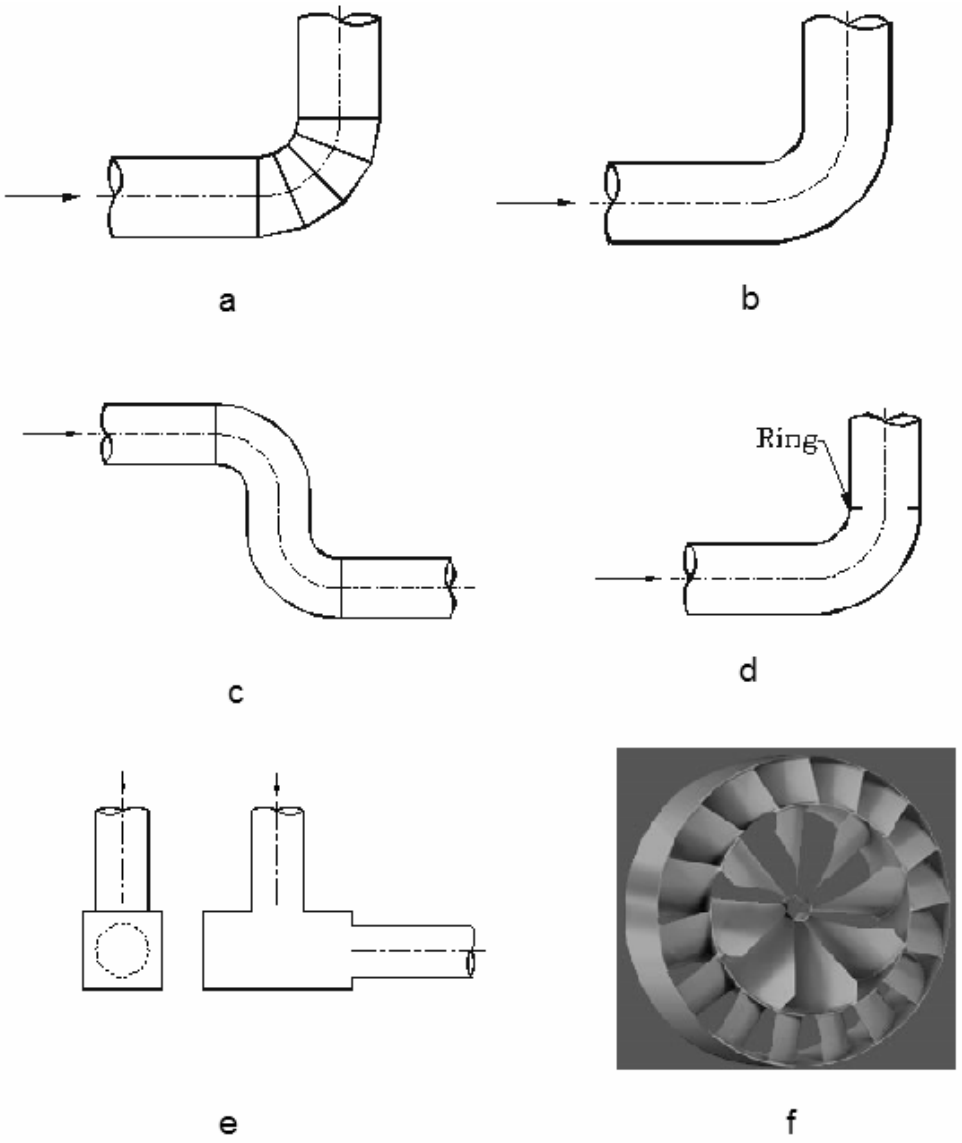

Figure 2.9: Schematics of mixing elements: a.) 90 degree segmented elbow, b.) 90 degree elbow, c.) S-shaped elbow, d.) Annular plate, e.) Mixing box and f.) Air blender.

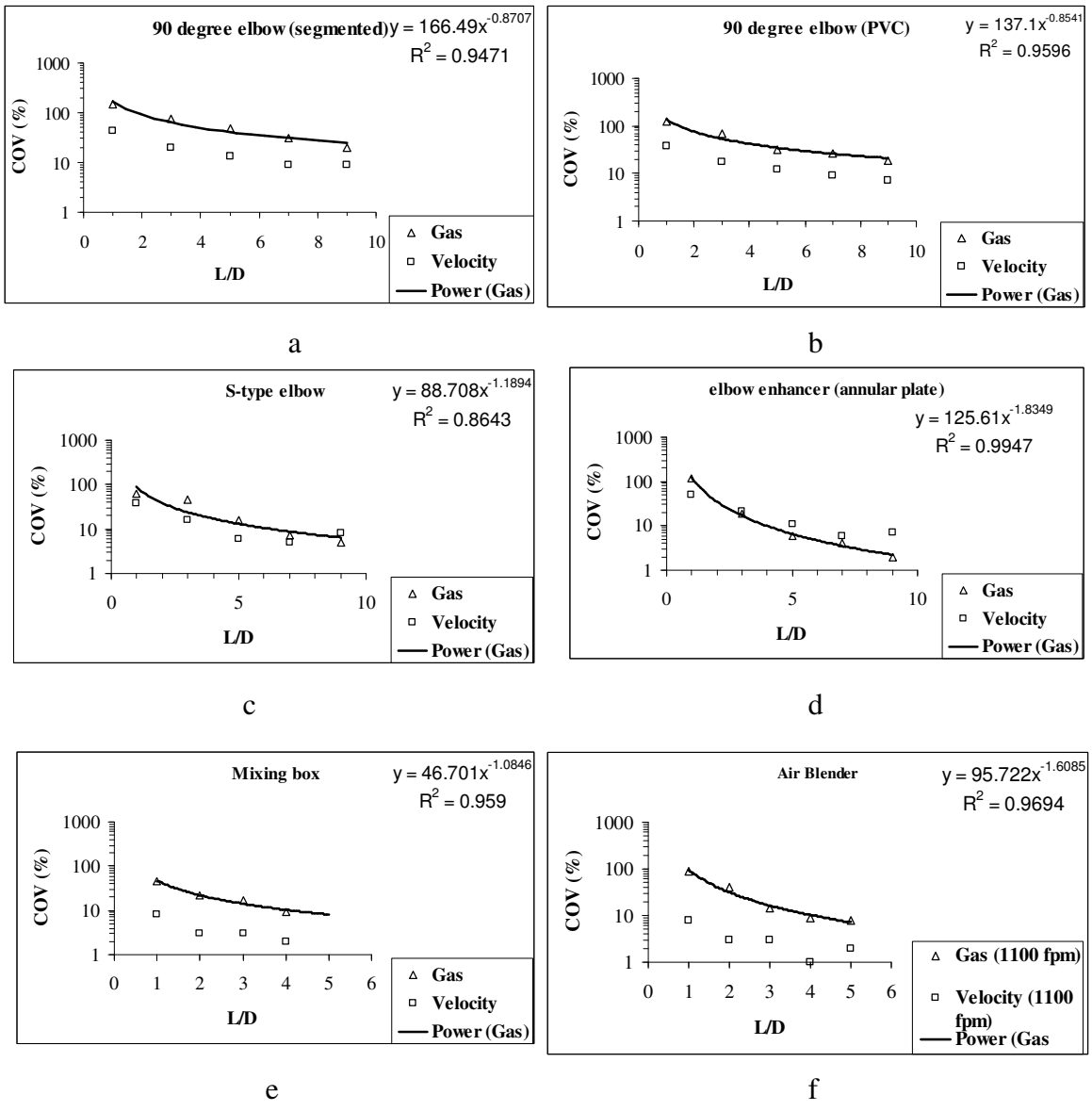

Figure 2.10: Velocity and tracer gas concentration COVs as a function of distance downstream of the mixing elements for six different mixing elements: a.) 90 degree segmented elbow, b.) 90 degree elbow, c.) S-shaped elbow, d.) Annular plate, e.) Mixing box and f.) Air blender. Power law fits are plotted along with the experimental data.

The mixing downstream of various mixing elements (Gupta 1999) was modeled using the power law profiles. The different mixing elements modeled included a 90°

segmented elbow, a 90° elbow , an S-shaped elbow, a 90° elbow with an annular plate, a generic mixing box and an air blender. The schematics for the mixing elements are shown in Figure 2.9. The plots in Figure 2.10 show the tracer gas and velocity COVs and the corresponding power law fits for these mixing elements. The R^2 values for the power law fits are also shown in Figure 2.10.

The R^2 values for the power law profile is generally above 0.95 except for the S-shaped double elbow for which the power law fit has a R^2 value of 0.86. This indicates that the power law profile models are satisfactory for most mixing elements.

3. MIXING IN TURBULENT FLOW THROUGH STRAIGHT TUBES

Introduction

Turbulent flow through a straight pipe has been considered in a number of previous studies. The focus of these studies has been the fully-developed flow through a tube (Laufer 1954, Ramaprian 1984, Eggels et al. 1994, Rudman and Blackburn 1999, Vijiapurapu and Cui 2004). Developing flows though straight tubes have also been studied (Richman and Azad 1973, Lin and Chang 1996, Wang and Derksen 1999), though not as comprehensively as fully developed flow. These studies include both experimental and numerical investigations. In the numerical investigations, various turbulence models were used for representing the turbulence. In this study we use RANS and LES for modeling turbulence.

Effect of grid structure on LES

Two different types of grids were used for the straight tube simulations. The cells in the grid shown in Figure 3.1a are more uniformly sized, but controlling the structure of the grid is difficult. For example, selectively refining the grid in a particular area is not possible. The grid in Figure 3.1b uses a multi-block structure with five blocks being used in this case. We can selectively refine each of the blocks; therefore we have more control over the structure of the grid. The disadvantage with this grid is that the aspect ratio of the cells varies significantly from the wall to the center of the pipe. The aspect

ratio of the near wall cells is large; this leads to larger convergence times (Buelow et al. 1993) and lesser accuracy for the numerical simulations. Different monitors such as the wall shear stress and axial velocity for LES simulation with the new grid are plotted in Figure 3.2.

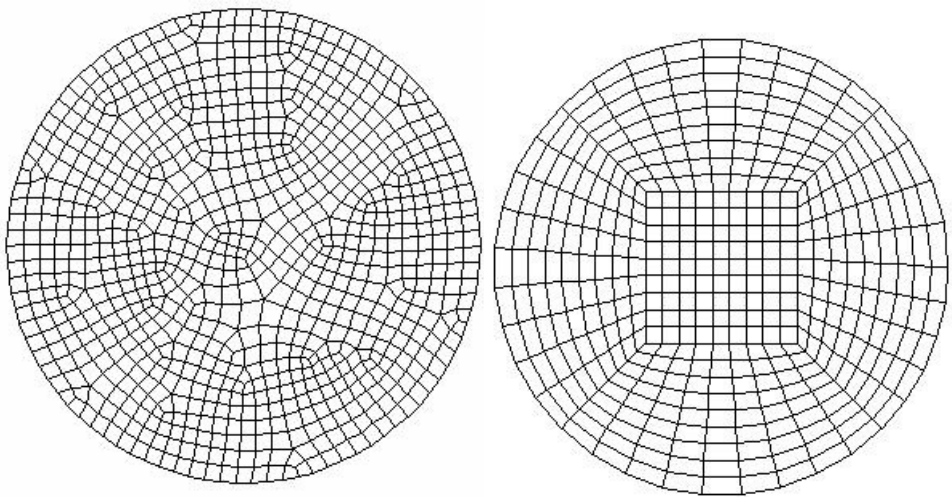

(a) (b)

Figure 3.1: The structure of the grid; a) Unstructured b) Block structured.

It can be seen from Figure 3.2 that the flow is statistically stationary after a flow time of around 3.2 s. A *k-ε* realizable model simulation was also run with the new grid. Comparison was made between the RANS and LES models for the flow through a straight tube. The flow statistics that were compared include the mean velocities, kinetic energy and dissipation.

The results from the LES simulations on the new grid showed that the grid is extremely diffusive. The initial conditions for the simulations on the new grid were taken from the simulations using the old grid. The turbulent fluctuations diminished and finally died out when the simulations were run using the block structured grid.

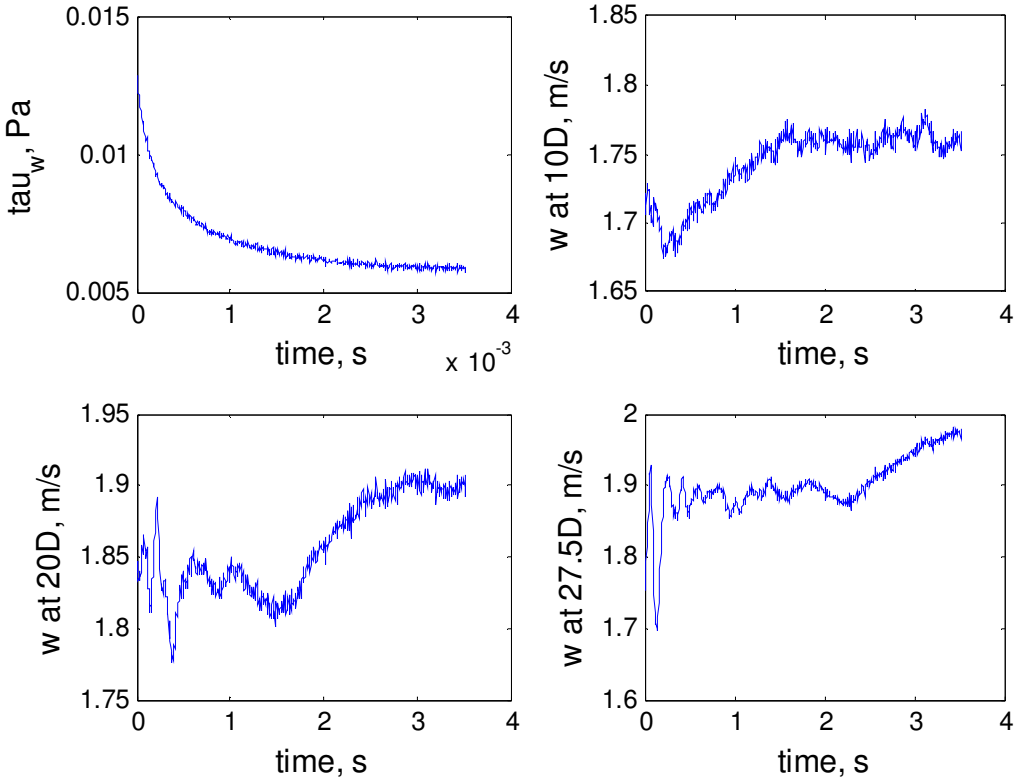

Figure 3.2: Monitors for LES simulations using the new refined grid.

The diffusive nature of the block-structured grid can be seen from Figure 3.3, which shows the mean velocity profile at a distance of 27.5*D* downstream of the

entrance. At a distance of 27.5*D* from the entrance we expect the flow to be nearly fully developed. Compared with the fully developed mean flow profile measured in experiments (Laufer 1954), the velocity profile from the current simulations exhibit a plug flow like behavior. The flat nature of the mid part of the profile is a manifestation of the highly diffusive nature of the grid. While LES simulations on the block structured grid leads to the above mentioned problems, using the block structured grid to run RANS simulations did not lead to any such issues.

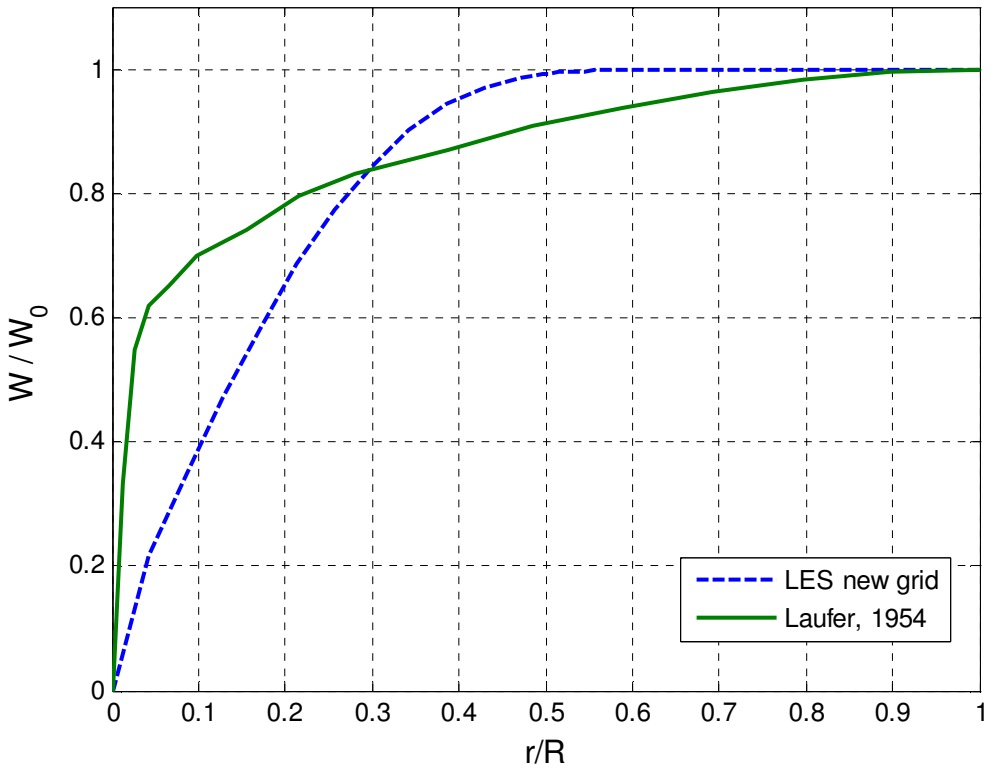

Figure 3.3: Mean axial velocity profile at 27.5D from the entrance for LES simulations using the new grid compared with the fully developed flow profile (Laufer, 1954).

Therefore, for LES simulations the unstructured grid as shown in Figure 3.1a was used, and for the RANS simulations either the unstructured or the block structured grids were used.

Geometry

Diameter of the pipe, D = 0.1 m
Length of the pipe, L = 1.5 D = 0.15 m

Scales of Turbulence

The Taylor micro-scale, $\lambda = D\left(\frac{15}{\mathrm{Re}}\right)^{0.5} = 1.87e-3$ m

The Kolmogorov scale, $\eta = D\left(\frac{1}{\mathrm{Re}}\right)^{0.75} = 3.36e-5$ m

Mesh

Hexahedral mesh elements were used.
Characteristic length of mesh edge = 0.0015 m (smaller than the Taylor micro-scale)
Total number of nodes = 100 (along the length) x 3824 (on the face)
Number of nodes along a vertical line through the center of a face = 66

Flow Characteristics

Average Velocity = 6.236 m/s
Average Reynolds Number = 42700
Centerline velocity = 7.7 m/s
Reynolds number based on centerline velocity = 52700
Friction velocity for fully developed flow profile (ref: Fox & McDonalds) = 0.32 m/s

Time

Value of each time step = 0.0002 s
Equivalent length scale = 1.4e-3 m (smaller than Taylor micro-scale)
Time taken for the fluid to pass once through the domain = 0.024 s = 120 time steps
Time for which simulation was run = 3980 time steps = 0.8 s = 33 turnovers
The time statistics were taken between time steps 2100 and 3980

Convergence criteria

Should be less than 1e-4.

Monitors

The average wall shear stress, velocities at the midpoint and the average centerline velocity were monitored to check whether the flow has become statistically stationary with respect to time.

Figure 3.4: The simulation parameters for periodic flow through a straight tube.

Periodic flow through a straight tube

LES simulations were performed on a straight circular tube with translationally periodic conditions at the inlet and outlet. The data obtained from these simulations were compared to experimental data (Laufer 1954). The primary aim of this simulation was to validate the implementation of LES in the commercial CFD software, Fluent. Periodic flow through a straight pipe is a canonical problem, for which extensive experimental and numerical (Eggels et al. 1994) data are available. Therefore this particular simulation was chosen to validate the code. The simulation parameters are given in Figure 3.4.

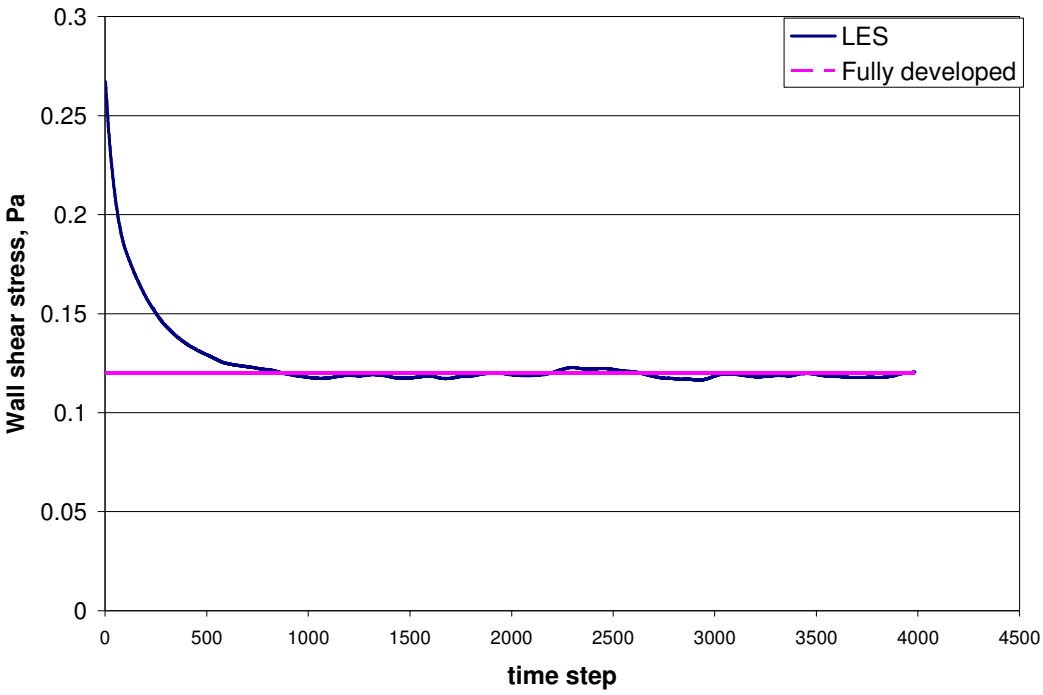

Figure 3.5: The temporal evolution of the wall shear stress averaged over the entire wall.

The temporal evolution of the wall shear stress (Figure 3.5), axial velocity (Figure 3.6b) and transverse velocities (Figure 3.6c and Figure 3.6d) are plotted. These quantities were plotted to monitor the flow. We can see from Figure 3.5 that the average wall shear stress oscillates with very small amplitude around the value expected for a fully developed flow profile. This indicates that the flow has developed from the initially isotropic field into a fully developed turbulent flow field (Figure 3.6a). The fluctuations of the axial and transverse velocity fields are also fairly constant about a constant mean value. This provides further validation to our conclusion that the flow has converged.

The upwinding scheme was found to be unsuitable for LES simulations due to its highly diffusive nature. This leads to the diminishing of the effects of the smaller scales. The central differencing scheme is more suited for LES simulations as it is less diffusive and also more accurate because it is a second order scheme.

In Figure 3.7a the mean axial velocity across the cross-section is plotted as a function of radial distance from the wall. We can see from the figure that the mean axial velocity from the LES compares very well with the experimental data. In Figure 3.7b, Figure 3.7c and Figure 3.7d the *rms* value of the axial and transverse velocity fluctuations are plotted. The second order statistics (*rms* values) also compare well with the experimental values.

The LES simulations match well with the experimental results for the periodic flow through a straight tube at a Reynolds number of around 50,000. This validates the use of LES in simulations run using Fluent.

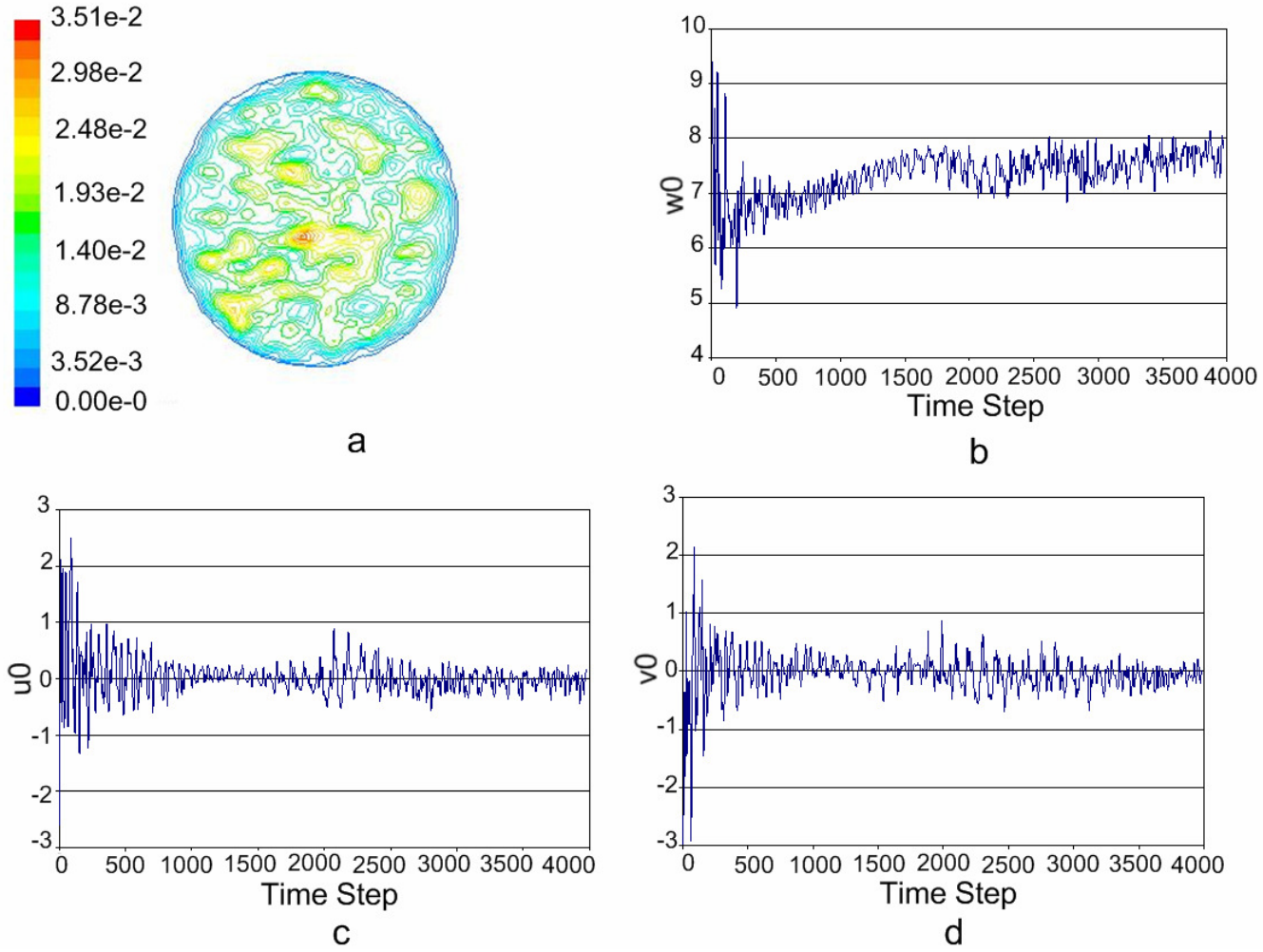

Figure 3.6: a.) *rms* transverse velocity contours; b.) Temporal evolution of the axial velocity (z-axis) at the midpoint in the domain. c.) Temporal evolution of u (x-velocity) at the midpoint in the domain; d.) Temporal evolution of v (y-velocity) at the midpoint in the domain.

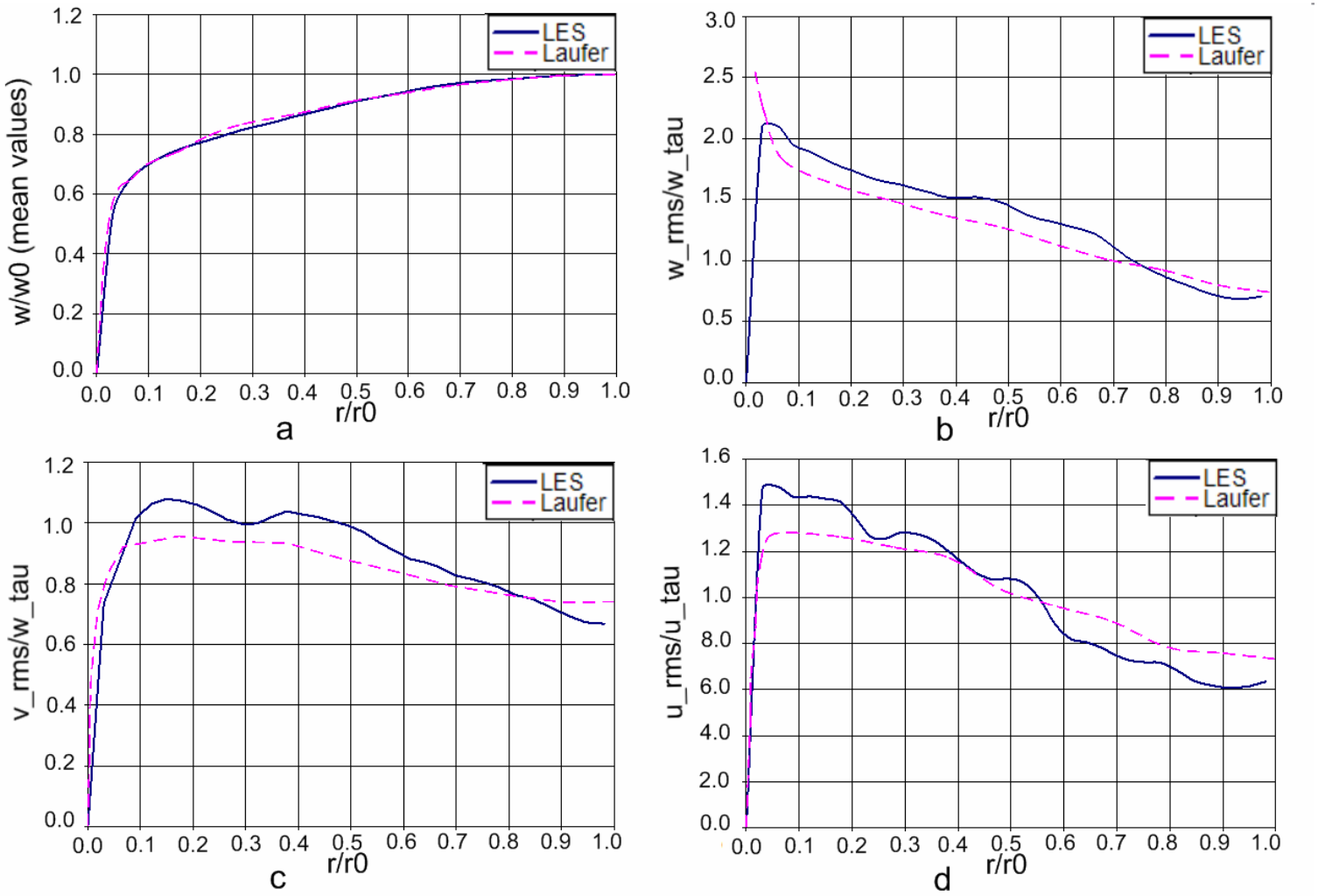

Figure 3.7: a.) Comparison of mean velocity profiles along a line parallel to the y-axis.; b.) Axial (w; z-direction) *rms* profiles are plotted along a line parallel to the y-axis.; c.) v; y-direction *rms* profiles are plotted along a line parallel to the y-axis.; d.) u; x-direction *rms* profiles are plotted along a line parallel to the y-axis.

Initial conditions and boundary conditions for LES

Turbulent wall functions were used to account for the flow close to the wall. The use of the log wall function is acceptable in geometries without considerable curvature. In geometries with considerable curvature (such as an elbow), the wall function has to be modified to reflect actual flow physics. In all the simulations in the study, the log wall law was used to model the near wall region. Therefore, simulations need to be run resolving the near wall region to study how the use of the log wall law affects the core flow.

The boundary conditions at the inlet were specified using velocity profile and turbulence intensity. A random Gaussian field is calculated by Fluent (Equation [3.1]) based on the inlet turbulent intensity provided.

$$\overline{u}_i = \left\langle \overline{u}_i \right\rangle + I\psi \left| \overline{u} \right| \qquad [3.1]$$

where I is the intensity of fluctuation, ψ is a random number with a Gaussian distribution (mean = 0, standard deviation = 1).

The turbulence propagates from inlet (Figure 3.8), where the inlet turbulence intensity is specified, into the interior domain. The turbulence dissipates after some axial distance if the initial velocity field specified is non-turbulent. The simulations have to be iterated for a long time for the non-turbulent flow field to develop into a turbulent flow field. Therefore it is important to specify a turbulent flow field as an initial condition for

faster convergence. The choice of the initial turbulent flow field will have a large influence on the final flow field if the flow is statistically unsteady. For statistically stationary flow, whatever be the initial turbulent flow field, it will develop into the final stationary field (given a sufficient amount of simulation time). The closer the initially turbulent flow field is to the final solution, the faster the solution will converge. An isotropic initial field was used as the initial condition for the present simulations.

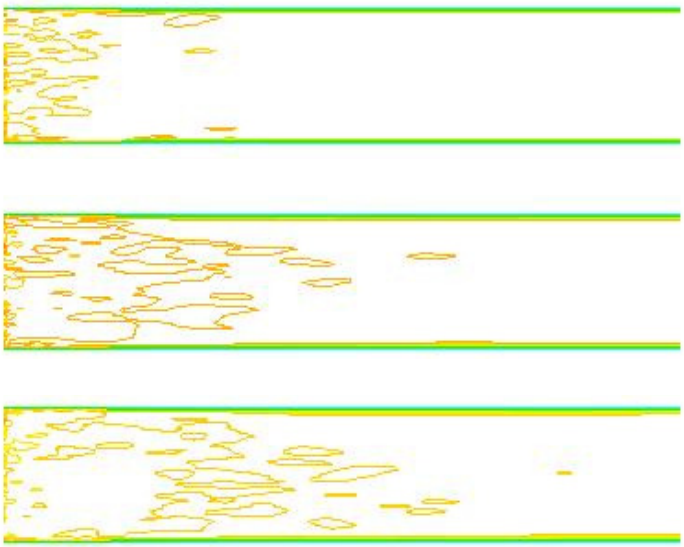

Figure 3.8: Propagation of turbulence from the inlet to the interior region of the pipe.

In Figure 3.9 the contours of velocity magnitude for an isotropic initial velocity field are plotted at a cross-section of the tube. As the flow field is homogeneous in all directions, it does not matter at which cross-section the contours are plotted. For the early simulations of turbulent flow through a straight tube, this isotropic flow field was

used as the initial condition. For the later simulation, the converged flow field from the earlier simulation was used as the initial condition, which helped in decreasing the time taken for the flow to become statistically stationary. A FORTRAN code was used to generate the isotropic velocity field.

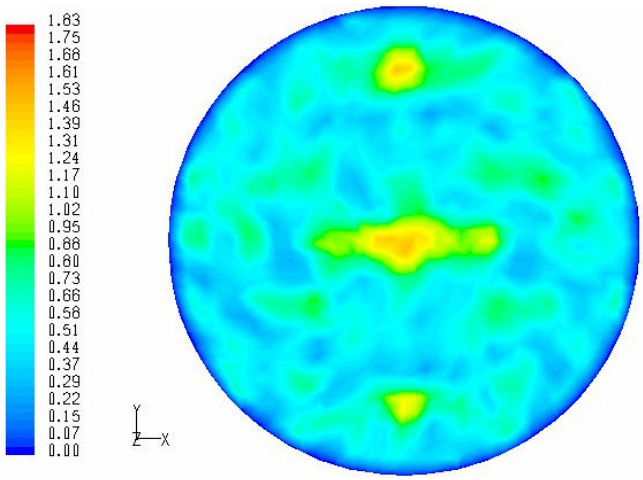

Figure 3.9: The contours of velocity magnitude (isotropic initial velocity field) for a cross-section of the pipe.

Developing flow through a straight tube

The scalar transport through a straight tube and a 90 degree elbow section was modeled using different RANS models and an LES model with a Smagorinsky sub-grid scale model. The various RANS models used included the standard, realizable and RNG k-ε models and the nine-equation Reynolds Stress model. These simulations were done on both two-dimensional axi-symmetric geometries and three dimensional geometries.

All the RANS simulations were steady simulations. The unsteady LES simulations were done on a three dimensional geometry using a static Smagorinsky sub-grid scale model. The simulations for a straight tube were run with three inlet turbulence intensities, i.e., 1.5%, 10% and 20%. The curvature ratio of an elbow is defined as the ratio of the radius of curvature of the elbow to the diameter of the pipe. For the studies with a 90° elbow, the curvature ratio was equal to unity. RANS simulations were also performed for two elbows in series in S- and U-configurations. The velocity and tracer gas concentration coefficients of variation (COVs) were compared with experimental results.

Numerical prediction of mixing through a straight tube

The numerical simulations were run for a straight tube. The straight tube geometry was chosen because of the simplicity of the geometry and the availability of experimental data (Anand et al. 2003) to validate the simulations. The experimental data are available for inlet turbulent intensities of 1.5%, 10% and 20%. The shape of the inlet velocity profile and the turbulent intensity profile are not uniform although for some simulations a uniform profile was assumed. At the entrance, a biplane grid (two arrays of parallel, uniformly spaced cylinders) was used in the experiments to generate turbulence at the entrance to increase the turbulence intensity. The flow in the entrance section including the biplane grid was studied numerically. The flow through the straight tube entrance is discussed in the next section.

Entrance to the straight tube

The schematic of the entrance section is shown in Figure 3.10. The flow enters through the bell-mouth section and then passes through the biplane grid (Figure 3.10). When the flow enters the bell mouth the Reynolds number of the flow is approximately 5000. As the turbulent fluctuations are a function of the Reynolds number, the *rms* value of fluctuating velocities is lower at lower Reynolds numbers. At the exit of the converging bell-mouth section, biplane grids are used to achieve the desired level of the turbulence intensity.

The experimental setup that was numerically modeled consisted of a bell mouth at the entrance of a Schedule 40, PVC straight duct of 152 mm inner diameter. Biplane grids were designed with a spacing-to-diameter ratio of 5. Grids with spacing of 25 mm and 50 mm were used to generate turbulence intensities of 10% and 20% respectively. In the absence of the biplane grid, the turbulence intensity at the entrance of the tube was 1.5%. The parameters for the numerical simulation through the entrance of the straight tube are given in Figure 3.11. Layout of the experimental setup is given in Figure 3.12.

The instantaneous velocity contour along center plane at a time of 6 s is shown in Figure 3.13. We can see the variation of velocity from zero to a maximum between the legs of the grid. This in turn leads to steep velocity gradients between the grids. Therefore, there is a large production of turbulent kinetic energy near the grids which results in large turbulent intensities at the plane of the biplane grids.

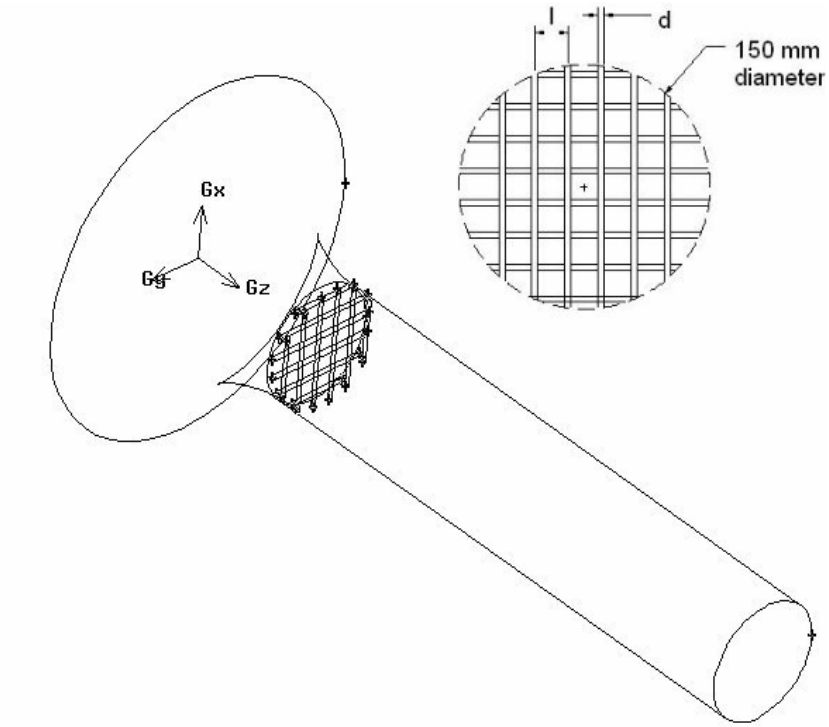

Figure 3.10: Schematic of the tube entrance section. The flow enters through the bell-mouth and is in the positive Z direction. The schematic of the biplane grids is shown as well.

Boundary Conditions

Velocity Inlet – Inlet Turbulent Intensity = 2 %
Outflow boundary condition

Geometry

Diameter of the entrance = 0.45 m
Diameter of the pipe, D = 0.15 m
L/D = 5

Scales of Turbulence

The Taylor micro-scale, $\lambda = D\left(\frac{15}{\mathrm{Re}}\right)^{0.5} = 4.76e-3 \text{ m}$

The Kolmogorov scale, $\eta = D\left(\frac{1}{\mathrm{Re}}\right)^{0.75} = 1.11e-5 \text{ m}$

Mesh

Tetrahedral mesh elements were used.
Characteristic length of mesh edge = 0.0075 m (slightly less than the Taylor micro-scale)

Flow Characteristics

Average Velocity in pipe = 1.45 m/s
Average Reynolds Number = 14890
Wall shear stress, u_p = 0.0087 Pa
Friction velocity for fully developed flow profile (ref: Fox & McDonalds) = 0.084 m/s

Time

Maximum value of time step = 0.005 s
Equivalent length scale = 7.25e-3 m
Time taken for the fluid to pass once through the domain = 3.1 s
Time for which simulation was run till now = 14 s = 4.5 turnovers

Convergence criteria

1e-4

Numerical Scheme

Central difference schemes were used except for pressure for which a second order scheme was used. SIMPLE pressure – velocity coupling was used.

Figure 3.11: The simulation parameters for developing flow through a straight tube.

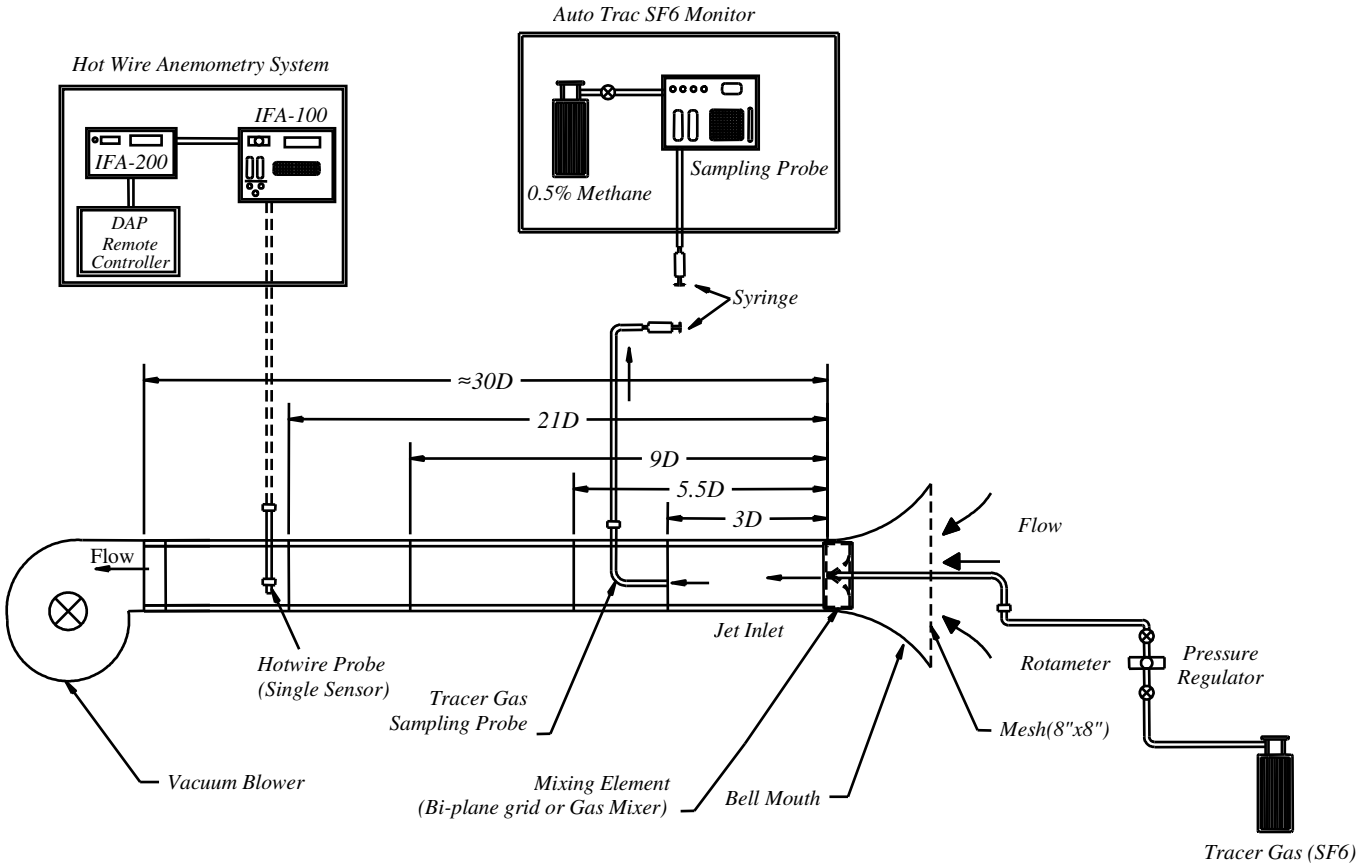

Figure 3.12: Layout of apparatus used to test various mixing elements with a straight pipe (Anand et al. 2003).

Figure 3.14 shows the development of the axial *rms* velocity along the centerline. Figure 3.14a shows the profile for the whole tube, in this case a turbulence intensity of 10% was artificially produced according to Equation [3.1] at the entrance. Figure 3.14b shows the development of the turbulence intensity in the entrance section of the tube, where the turbulence intensity created is due to the physical presence of biplane grids in the geometry of the model. We can see that in both the cases there is a rapid decrease in the turbulence intensity. From the turbulence intensity plotted at the centerline for the whole tube we can see that the turbulence intensity starts rising towards the fully developed flow value.

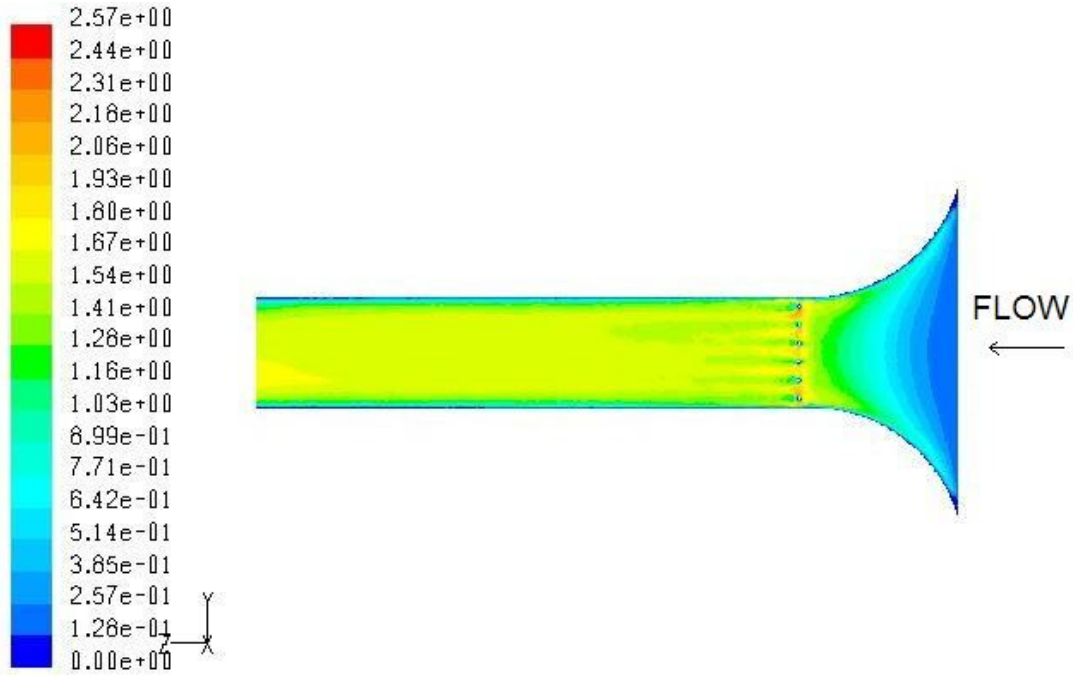

Figure 3.13: Axial instantaneous velocity (m/s) contours along a center plane at a time t = 6 s.

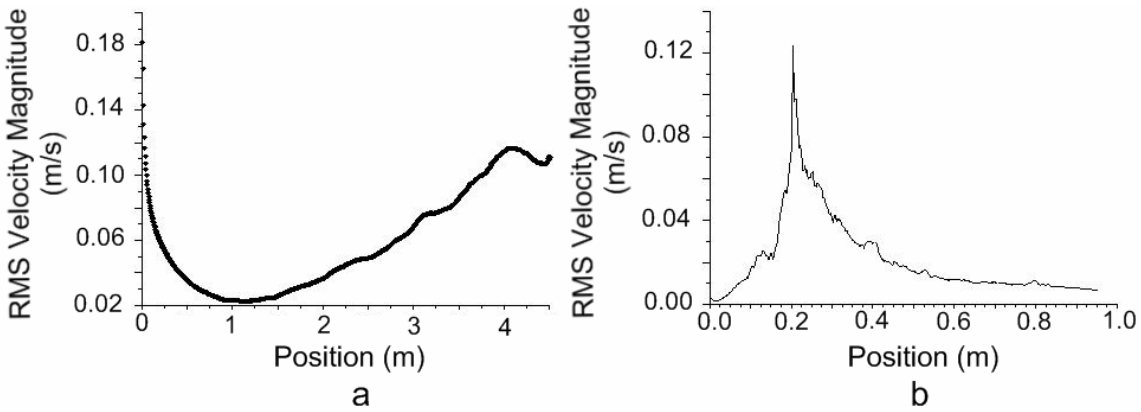

Figure 3.14: *rms* axial velocity along centerline for a.) The whole tube and b.) Entrance section.

Figure 3.15 shows the *rms* velocity (turbulence intensity) contours at the plane of release of tracer gas (SF_6). We can see that in case of the artificially induced turbulence (Figure 3.15a) the intensity is uniform across the plane whereas it varies in the case of the actual entrance (Figure 3.15b). Also, the average turbulence intensity at the SF_6 plane release is 11 % which is close to the experimentally determined value of 10 %.

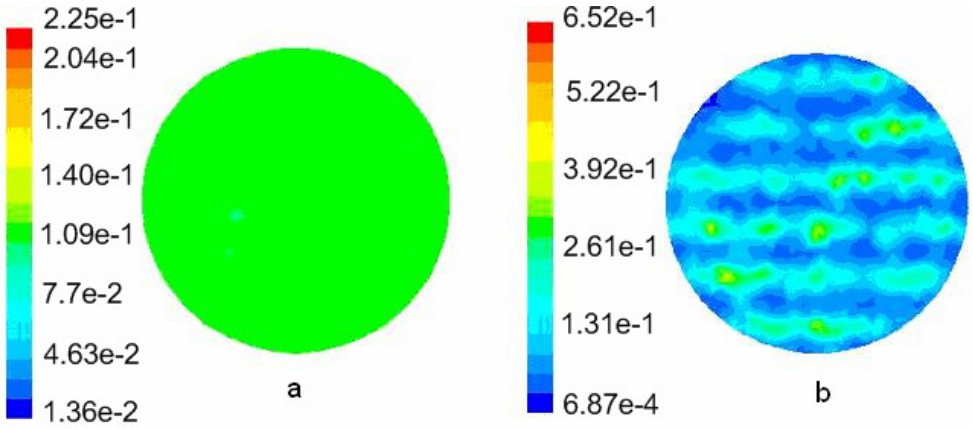

Figure 3.15: Turbulence intensity for a.) Artificial turbulence and b.) Simulated entrance

Developing flow in a straight tube

Numerical simulations were performed for developing flow through a straight tube using different RANS models (standard, realizable, RNG k-ε and Reynolds Stress Transport model) and LES. These numerical simulations were compared to results from two different experiments. For the first set of the experiments (Gupta 1999) the entrance turbulence intensity is unknown, however it is assumed herein to be 5%. In the other set of experiments (Anand et al. 2003) the inlet turbulent intensity was measured. These set of experiments were run at three different inlet turbulence intensities, viz., 1.5%, 10% and 20%. The experimental setup for these set of experiments is shown in Figure 3.12.

$D = 0.152$ m
$L / D = 20$
$\Delta t = 0.01$ s for first 5 time steps, $\Delta t = 0.01$ s thereafter
$t = 10$ s
$u_{air} = 10$ m/s, $u_{SF_6} = 2$ m/s
Number of cells = 126124
Inlet turbulence intensity = 5%

Figure 3.16: Parameters for LES simulations.

The various parameters used for the LES simulation performed for comparison with the first set of experiments are given in Figure 3.16. The COV of concentration as a function of downstream distance is plotted in Figure 3.17. Tracer gas concentration COVs from the numerical simulations were compared with a curve fit obtained from experimental data (Gupta 1999). The COVs in the figure have been normalized with the entrance COV for each of the different numerical simulations. Therefore, the normalized COV at the entrance for the different simulations is unity.

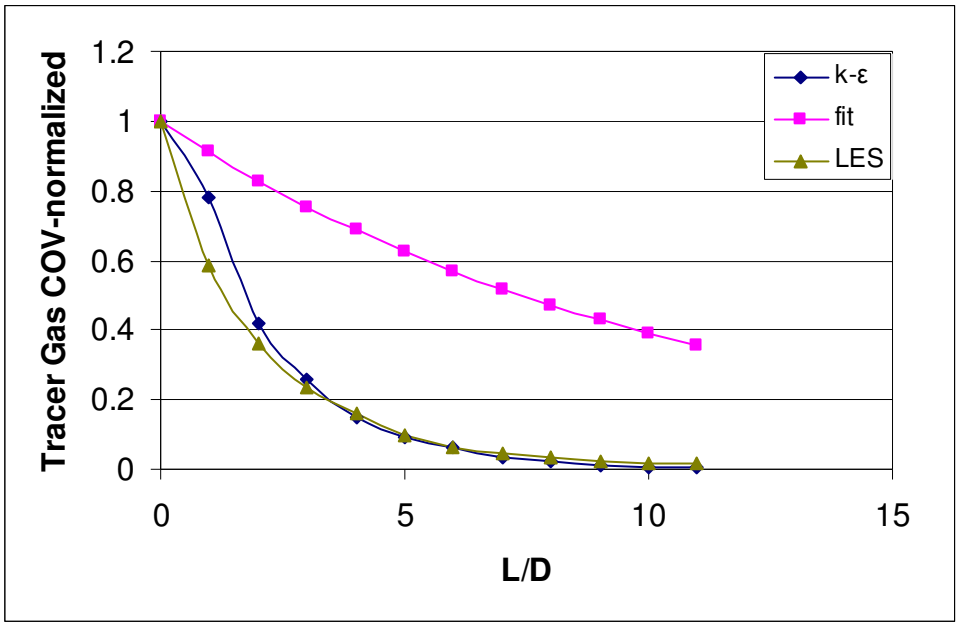

Figure 3.17: COV of tracer gas concentration as a function of downstream diameter for the tube at the inlet turbulence intensity of 5%.

We can see from Figure 3.17 that the numerical results from LES and k-ε models match quite well. The experimentally obtained exponential curve fit (Gupta 1999) predicts a lower rate of concentration COV decay. The higher value of dispersion in the LES simulations can be attributed to the coarse nature of the grids used. A disadvantage with the present simulation was that the value of the inlet turbulent intensity in the experiments was unknown. An inlet turbulence intensity of 5% was used in the numerical simulations, whereas in the experiments the inlet turbulence intensity could have been lower. However, in the next set of simulations, the experimental value (Anand et al., 2003) for the inlet turbulent intensity was a known quantity and equal to 10%.

Figure 3.18 shows instantaneous velocity and concentration contours from the LES simulations and the mean velocity and concentration contours from a *k-ε* simulation. These figures have been included to graphically bring out the difference between averaged RANS solutions and instantaneous time-dependent LES solutions.

Figure 3.19 and Figure 3.20 show the development of velocity and tracer gas concentration COVs along the axial direction of the tube. We can see that while the velocity COV predictions using LES or RANS are equally good, the concentration COV development prediction using LES is more accurate. The prediction from the Reynolds Stress model is shown in the figure. The predictions from other RANS models were similar to the prediction from the Reynolds stress model. The RANS simulation over-predicts the dispersion of the scalar as compared to the LES model.

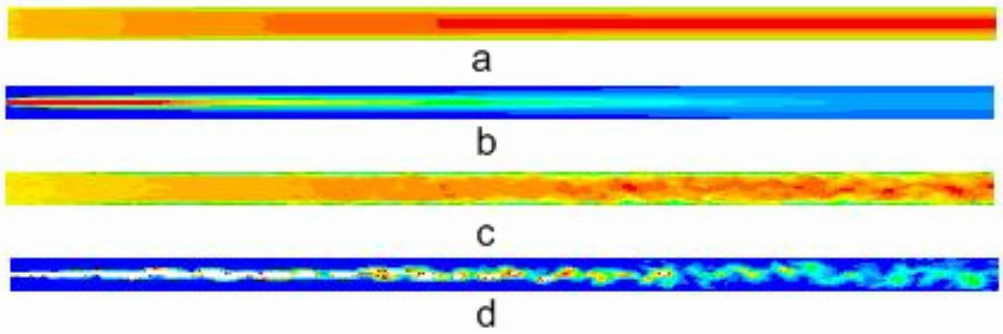

Figure 3.18: The instantaneous fields from LES and the mean flow field from the k-ε simulations are compared. a.) Mean velocity field from k-ε. b.) Mean concentration field from k-ε. c.) Instantaneous velocity field from LES and d.) Instantaneous concentration field from LES.

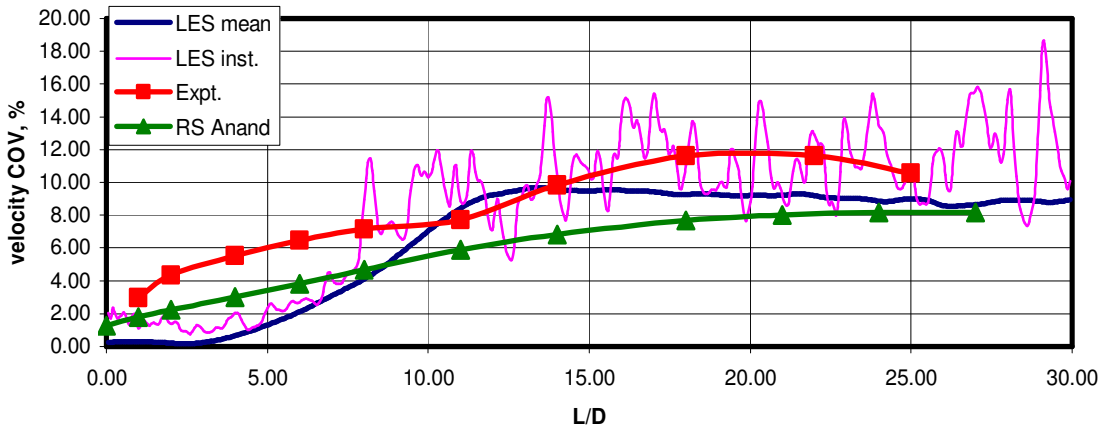

Figure 3.19: Velocity COV as a function of distance downstream from the inlet of the straight. The turbulence intensity at the inlet is 10%.

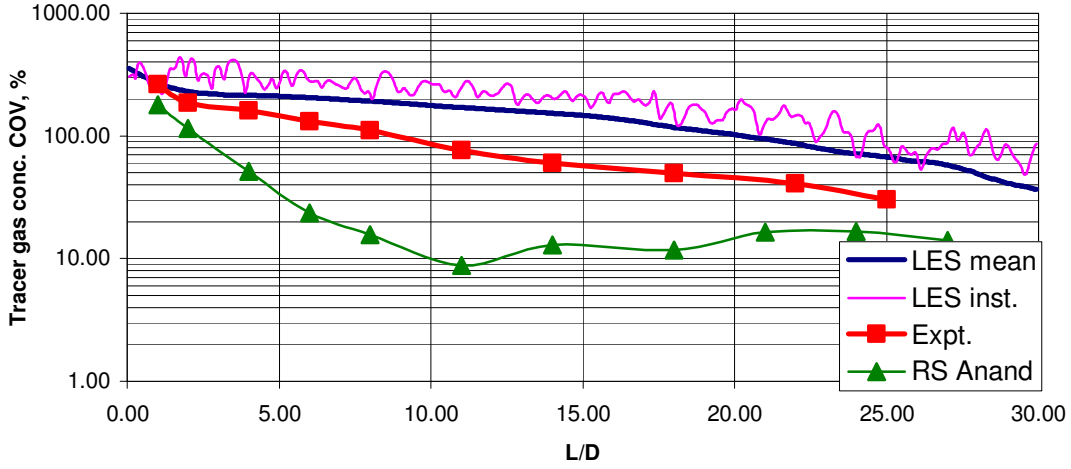

Figure 3.20: Concentration COV as a function of distance downstream from the inlet of the straight. The turbulence intensity at the inlet is 10%.

4. DEVELOPING FLOW THROUGH ELBOWS

Introduction

Numerical simulations were performed on elbow configurations. Both RANS and LES models were used to model the turbulence. Simulation was run on a two dimensional geometry using a k-ε model for the single elbow and double elbows in U- and S-configurations with the in-plane bends. Other RANS models were used to model a three dimensional elbow. A comparison was made between the RANS and LES simulations for the three-dimensional elbow geometry.

The two-dimensional simulations were limited by the fact that it is not possible to run an axi-symmetric simulation with the elbow geometry. Due to this the two-dimensional simulations do not truly represent the round pipe elbow geometry. Therefore RANS (k-ε RNG) simulations were performed with three-dimensional geometries of the U- and S-shaped double elbows. Selected results for the development of momentum in these three-dimensional geometries are presented.

2-D simulations

Presented in Figure 4.1 and Figure 4.2 are the results for numerical simulation of mixing of tracer gas in a single elbow and two elbows paired together in an S-configuration. In the single elbow configuration three different release points of the tracer gas were simulated. The numerical model used was a standard two dimensional k-

ε model. The concentration COVs have been normalized by the COV just downstream of the mixing element.

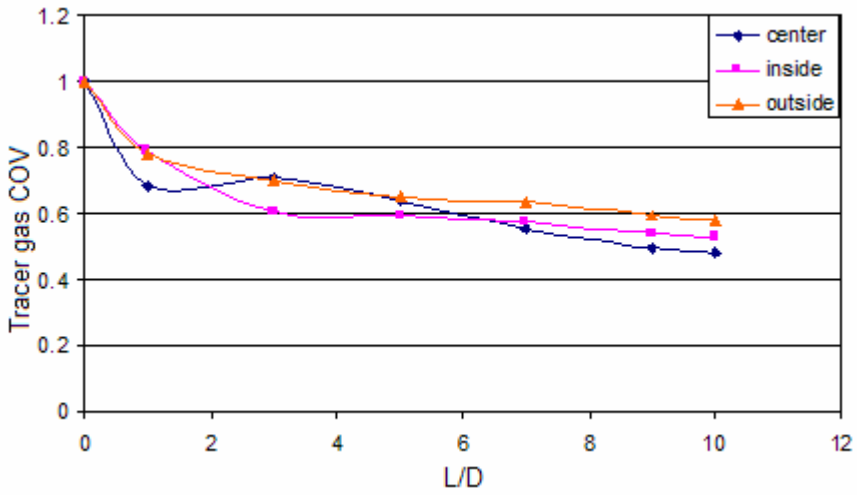

Figure 4.1: Concentration COV comparison for the inside, center and outside release points for a single elbow.

We can see a general trend from the comparison in Figure 4.2 between experimental and numerical data that the species mixing is greatly under predicted. This is due to the use of a two dimensional model in which the three dimensional rotational motion of the turbulent eddies cannot be modeled, therefore bulk mixing is greatly reduced.

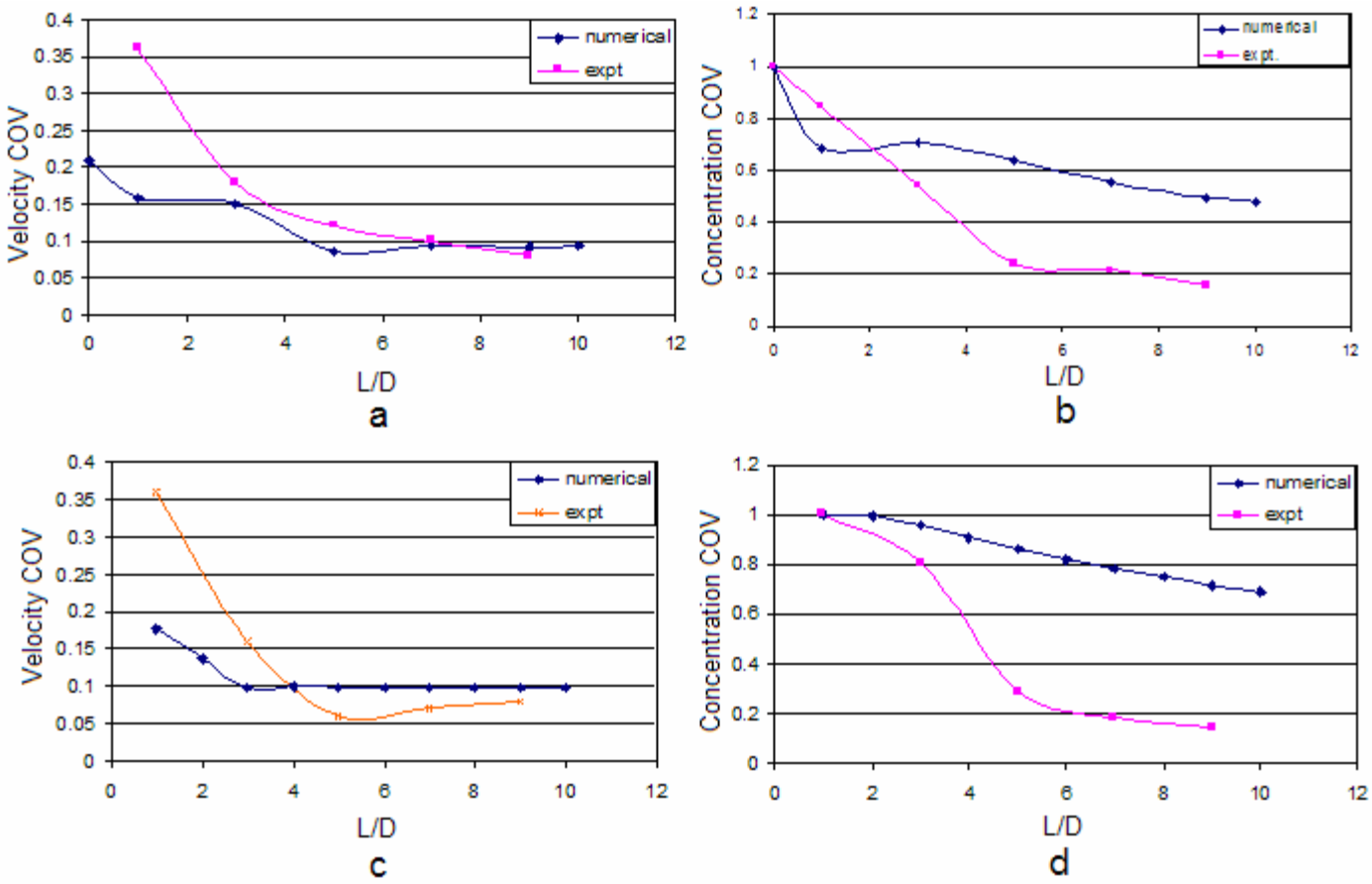

Figure 4.2: a.) Velocity COV for a single elbow; b.) Concentration COV for a single elbow with center release; c.) Velocity COV for the S-configuration of a double elbow; d.) Concentration COV for the S-configuration of a double elbow. A 2 D standard k-ε model was employed for the numerical simulations.

We can also see that the numerically predicted velocity COV just downstream of the element is much less than the experimentally observed value. This is probably because in the numerical simulation we are measuring the mean flow variation, whereas experimentally the instantaneous velocity field is measured. Due to the high amount of turbulence generated in the elbows, the instantaneous velocity field just downstream of the elbow will have a lot of variation. The schematic of a single elbow is shown in Figure 4.3.

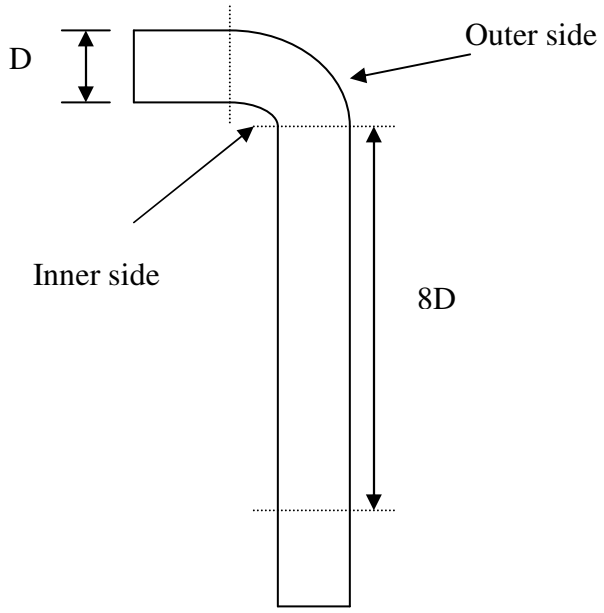

Figure 4.3: Schematic of the elbow, the size of the diameter, D = 0.15 m.

Figure 4.4 shows the velocity profile across a cross section (from the inner to the outer side of the elbow) at distances of 0, 3, 6 and 9 diameters downstream of the exit plane of the elbow. The inner side of the elbow has a z/D value of 0 and the outer side of the elbow has a z/D value of 1. At the exit plane of the elbow, velocity at the inner side of the elbow is higher than the velocity at the outer side. This is due to the creation of an adverse pressure gradient on the outer side due to centrifugal force. At this stage two secondary flow vortices are formed which transfer the high momentum from the inner side to the outer side of the elbow. This results in a higher velocity at the outer side of the elbow at a distance of 3 D from the exit plane of the elbow. Further downstream the velocity profile becomes more uniform due to turbulent diffusion.

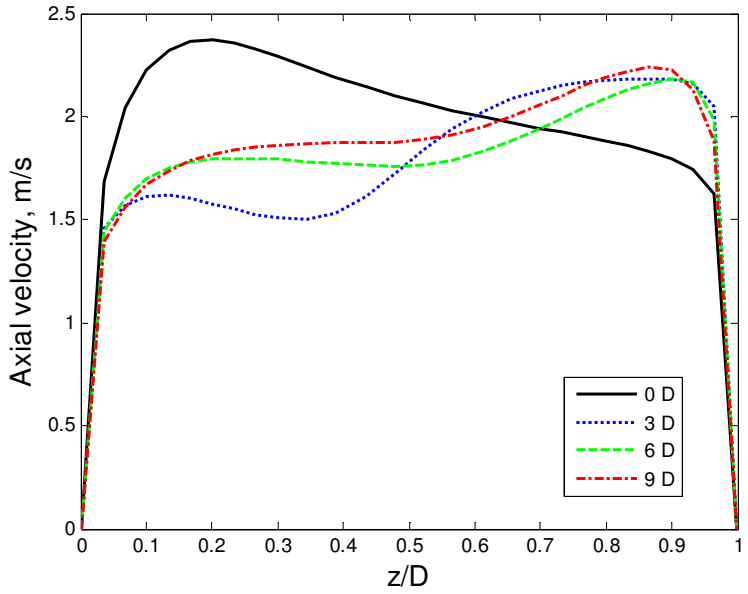

Figure 4.4: Axial velocity profile across the tube at distances of 0, 3, 6 and 9 diameters downstream of the exit plane of the elbow.

Scalar transport through the elbow – LES

The turbulent flow through a 90º elbow was simulated using LES in Fluent (version 6.1.22) CFD software. The various monitors for the flow are shown in Figure 4.5 and Figure 4.6. It can be seen from Figure 4.5 wall shear stress has converged to a steady value. Figure 4.6 shows the axial velocity and tracer gas concentration at distances 0 D, 4 D and 8 D downstream of the elbow as a function of time. It can be seen from the figure that the mean and variance of velocity and tracer gas concentration is nearly constant. In other words the first and second order statistics have converged. This indicates that the flow has become statistically stationary.

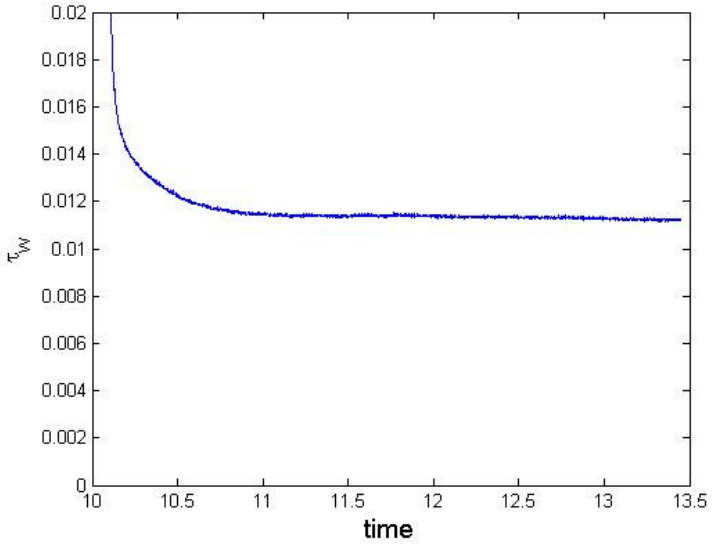

Figure 4.5: The average wall shear stress over the entire domain as a function of time.

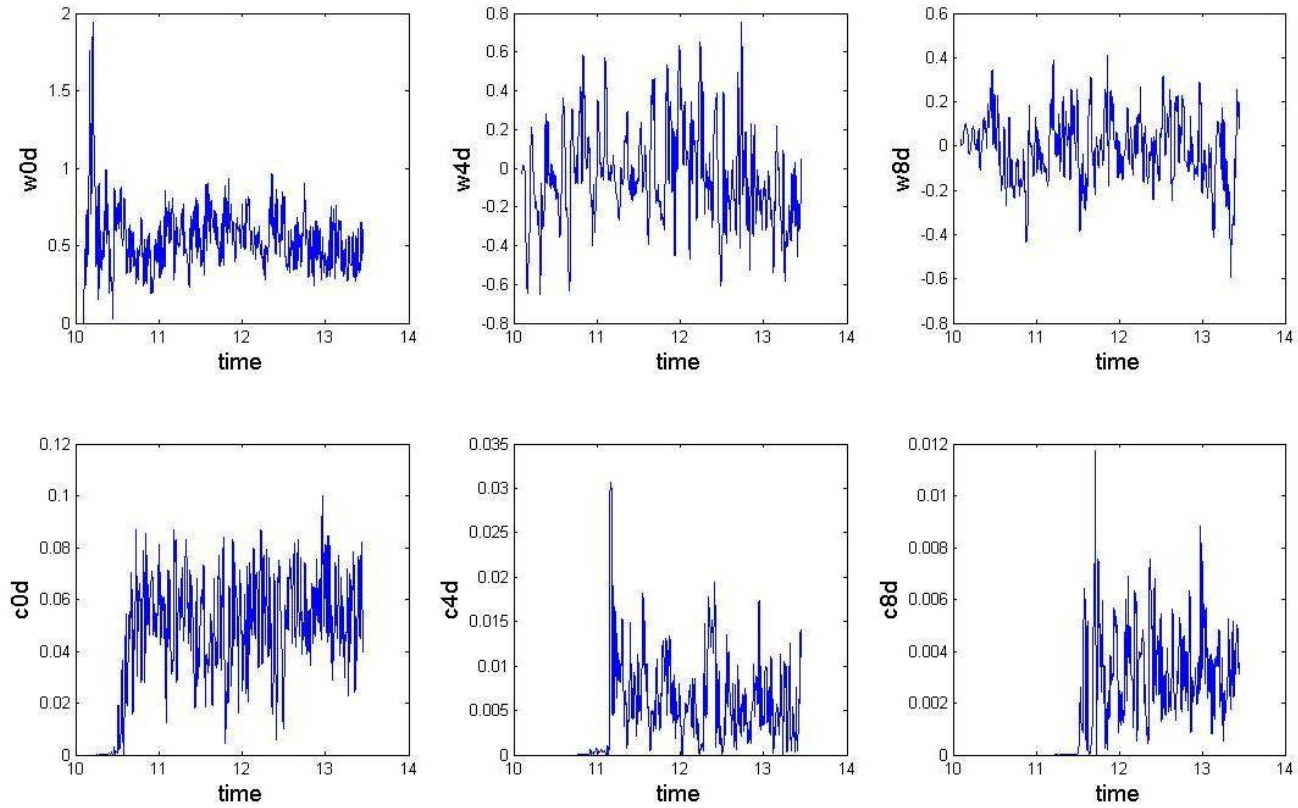

Figure 4.6: The axial velocity and concentration at various downstream distances (0D, 4D and 8D) of the elbow as a function of time.

The mean and instantaneous velocity and tracer gas concentration COVs are shown in Figure 4.7 and Figure 4.8 respectively. We can see from Figure 4.7 that the velocity COVs from LES are slightly lower than those observed experimentally. The tracer gas concentration COV calculation from LES gives a slightly higher value than the experimental data. There is a high likelihood that the COV values from the numerical simulation are within the uncertainty bounds of the experimental data. Also the concentration values are uniformly higher than experimental data, as sampling using a syringe smoothens the concentration profile across the cross section, thus resulting in lower COV values.

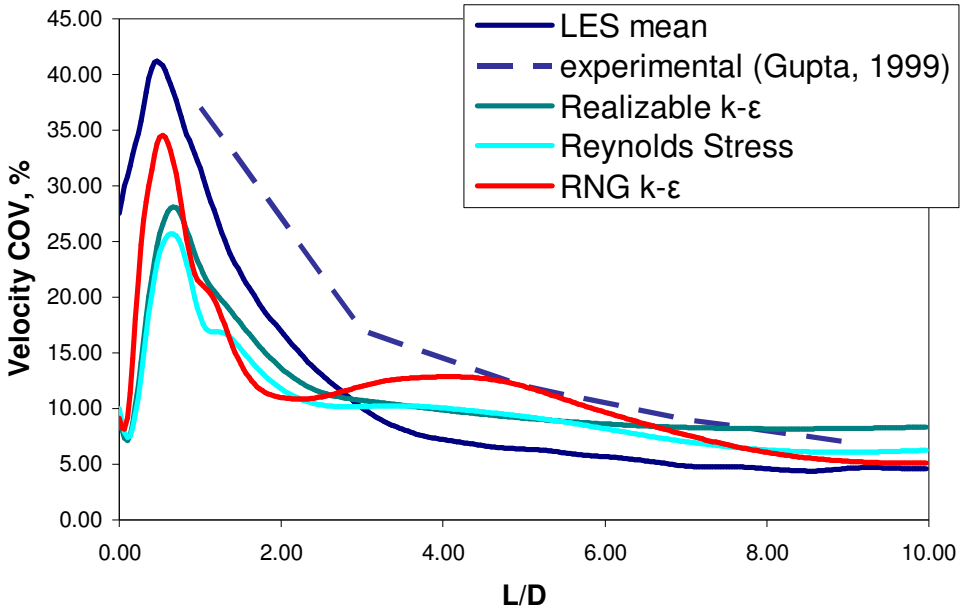

Figure 4.7: Velocity COVs are plotted against the downstream distance from the exit plane of the elbow.

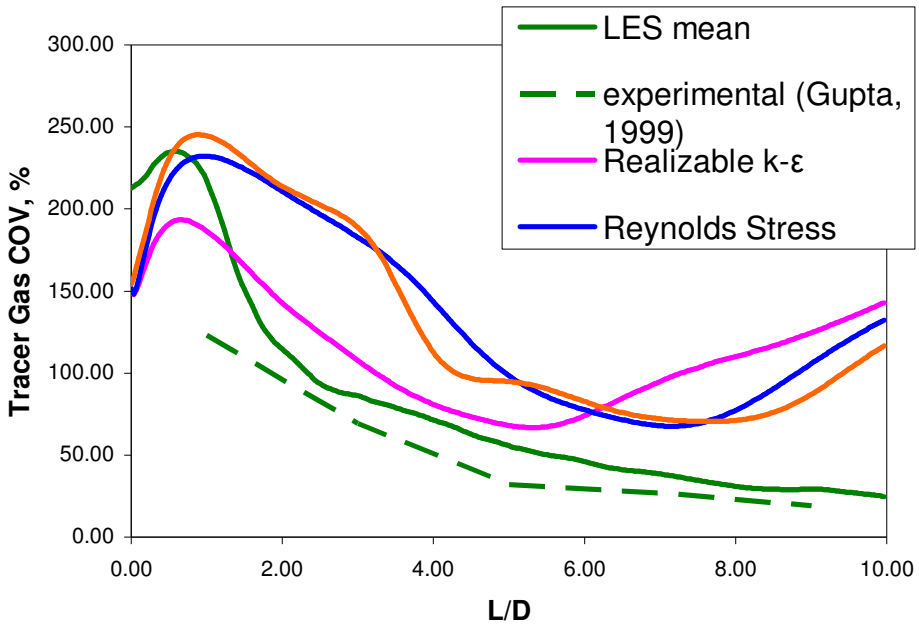

Figure 4.8: Concentration COVs are plotted against the downstream distance from the exit plane of the elbow.

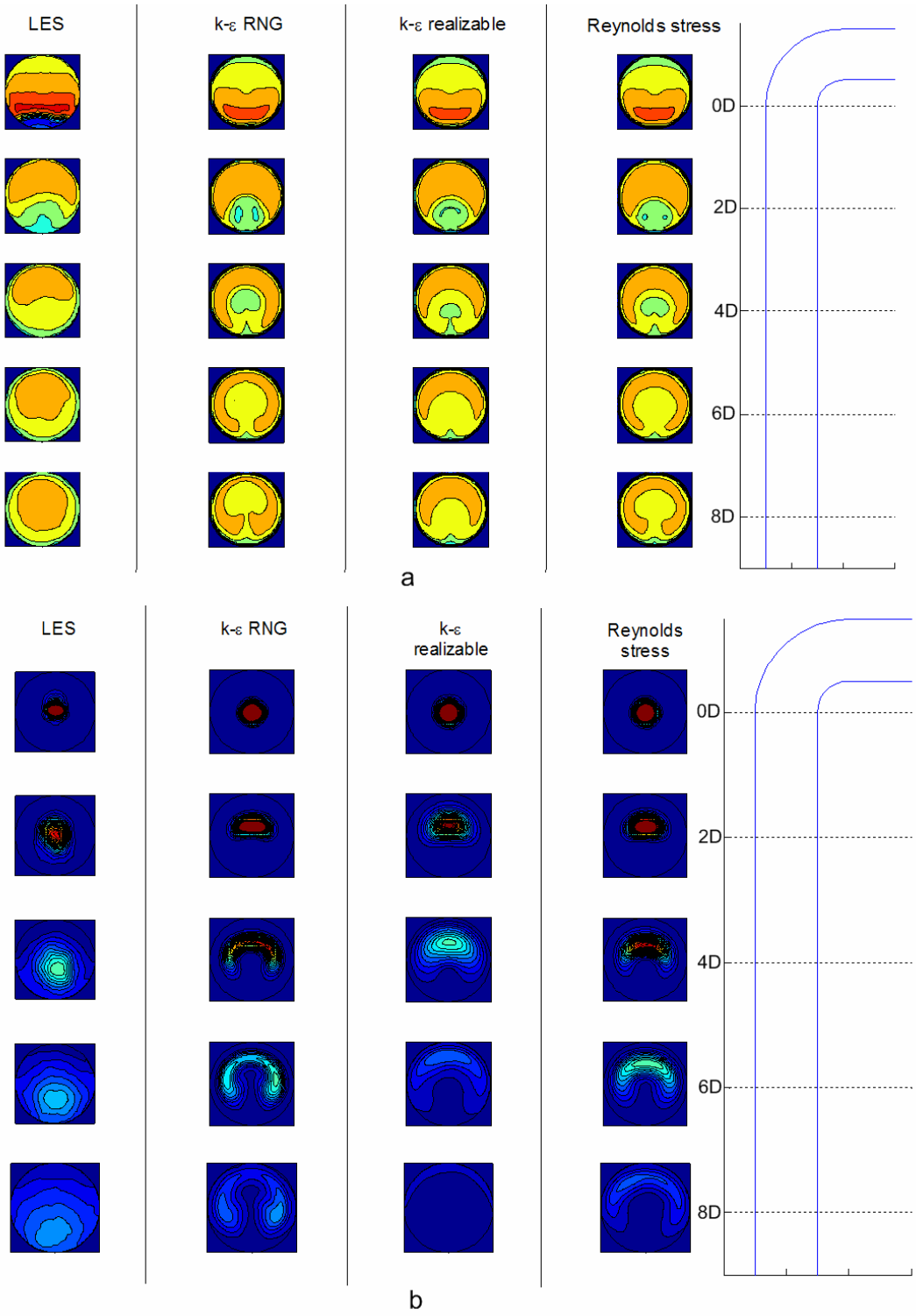

Figure 4.9: The contours of: a.) Velocity and b.) Concentration obtained from different turbulence models are plotted as a function of distance downstream of the elbow

Figure 4.9a and Figure 4.9b show the velocity and concentration profiles at different distances downstream of the elbow for the following turbulence models: LES, k-ε RNG, k-ε realizable and 9-equation Reynolds stress model. We can see from the figures that there is a strong similarity in the velocity and concentration profiles for the RANS models. However, there is a substantial difference between the RANS and LES simulations. The momentum transfer and therefore the dispersion of the tracer gas happen in a toroidal crescent shaped fashion for all the RANS simulations. The transport of momentum and tracer gas seems to happen in a much more uniform fashion for the LES simulations, which cause the results from the LES simulations to compare better with the experimental results.

Comparison between single elbow and S-shaped double elbow

A k-ε (RNG) RANS model was used to model the flow through a single elbow and an S-shaped double elbow. For the steady simulation, a first order upwind scheme was used to solve for the momentum and the pressure velocity coupling was handled using the SIMPLE scheme. In the flow through a single elbow there was a pair of secondary counter rotating vortices setup in the elbow. In the flow through an S-shaped double elbow there are two pairs of counter rotating vortices. The contours of velocity magnitude in the single and S-shaped double elbows at the mid-plane are shown in Figure 4.10a and Figure 4.10b respectively.

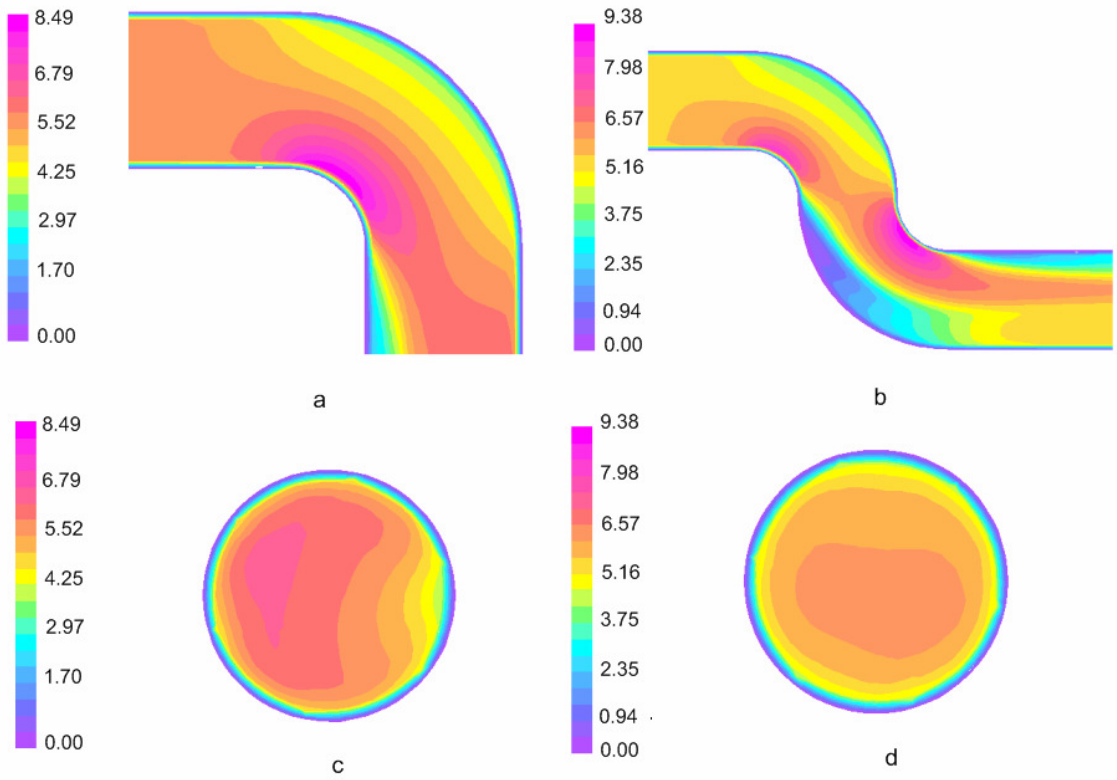

Figure 4.10: The velocity magnitude contours at the mid-plane of a.) Single elbow; and b.) S-shaped double elbow. Cross-plane velocity magnitude contours at a distance of 8 diameters from the exit plane of c.) Single elbow; and d.) S-shaped double elbow.

The presence of two pairs of counter-rotating vortices in the S-shaped double elbow aids in the cross-stream transfer of momentum. In the elbow, the scalar is primarily in the mid region of the cross section due to the midpoint release of the scalar. The transfer of momentum in the mid region due to the secondary flow vortices is from the inner side to the outer side. In the S-shaped double elbow as the inner and outer sides are on opposite ends in the first and second elbows, the secondary flow changes direction in the mid region from the first to the second elbow. This leads to a more uniform velocity profile downstream of the elbow compared to a geometry with a single

elbow. This can be seen from the comparison of the cross-plane velocity magnitude contours at a distance of eight diameters downstream of the exit plane of the single elbow and the S-shaped double elbow, which are shown in Figure 4.10c and Figure 4.10d respectively. The bias of momentum towards a single side (the outer side of the elbow; refer to Figure 4.3) can be clearly seen from Figure 4.10c. There is no such stacking of momentum in the S-shaped double elbow, which instead has a more symmetric profile tending towards the fully developed flow profile.

RANS/LES mixed approach

LES simulations take large time and resources due to the fine nature of the grid and the small time steps involved. In comparison RANS simulations take a lot lesser time and resources than LES simulations. The RANS models were found to be inadequate for predicting flow in complex geometries (e.g. when there is curvature in the flow). Striking a trade-off between the enormous time and resource usage of the LES model and the inadequacy of the RANS models for complex geometries is the hybrid RANS/LES technique. In the hybrid RANS/LES technique, parts of the geometry in which we expect complex flow will be solved using LES and other parts of the geometry in which the flow pattern is fairly straightforward will be solved using a RANS model.

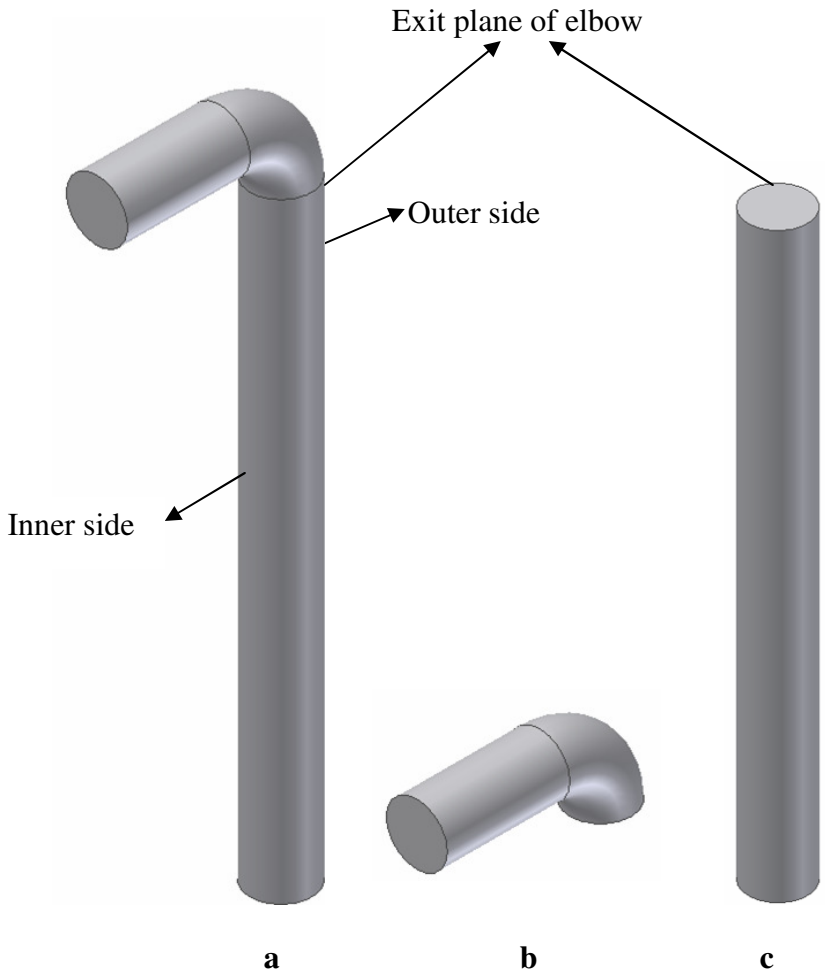

Figure 4.11: The geometries through which the flow was modeled. a.) The whole model; b.) The part modeled using LES and c.) The part modeled using RANS.

The aim of the current study was to validate the use of a RANS model downstream of the elbow and compare the results we obtain from such a simulation with the results from the LES simulation. The parts of the elbow where the RANS and LES models should be employed are shown in Figure 4.11. Though we would stop at the exit of the elbow for the LES simulation, to prevent the boundary conditions from having an

effect, it is better to at least model an extra two diameters downstream of the exit plane of the elbow. We use the statistics obtained from the LES simulation at the exit plane of the elbow to provide entrance boundary conditions for the RANS simulation. In the current study the boundary condition for the RANS simulation was obtained from existing LES simulations where 10 diameters downstream of the elbow were modeled.

The mean velocity and mean concentration at the exit plane of the elbow were obtained from the LES simulations. The contours of mean velocity and concentration are shown in Figure 4.12. In Figure 4.12 and Figure 4.13 the left hand side of the contour plot is the inner side of the elbow and the right hand side is the outer side of the elbow. The contours from the LES simulation are compared with similar contours obtained from an independent RANS (k-ε RNG) simulation. It can be seen from Figure 4.12 that the gradients of velocity and concentration are lower for the RANS simulation when compared to the LES simulations.

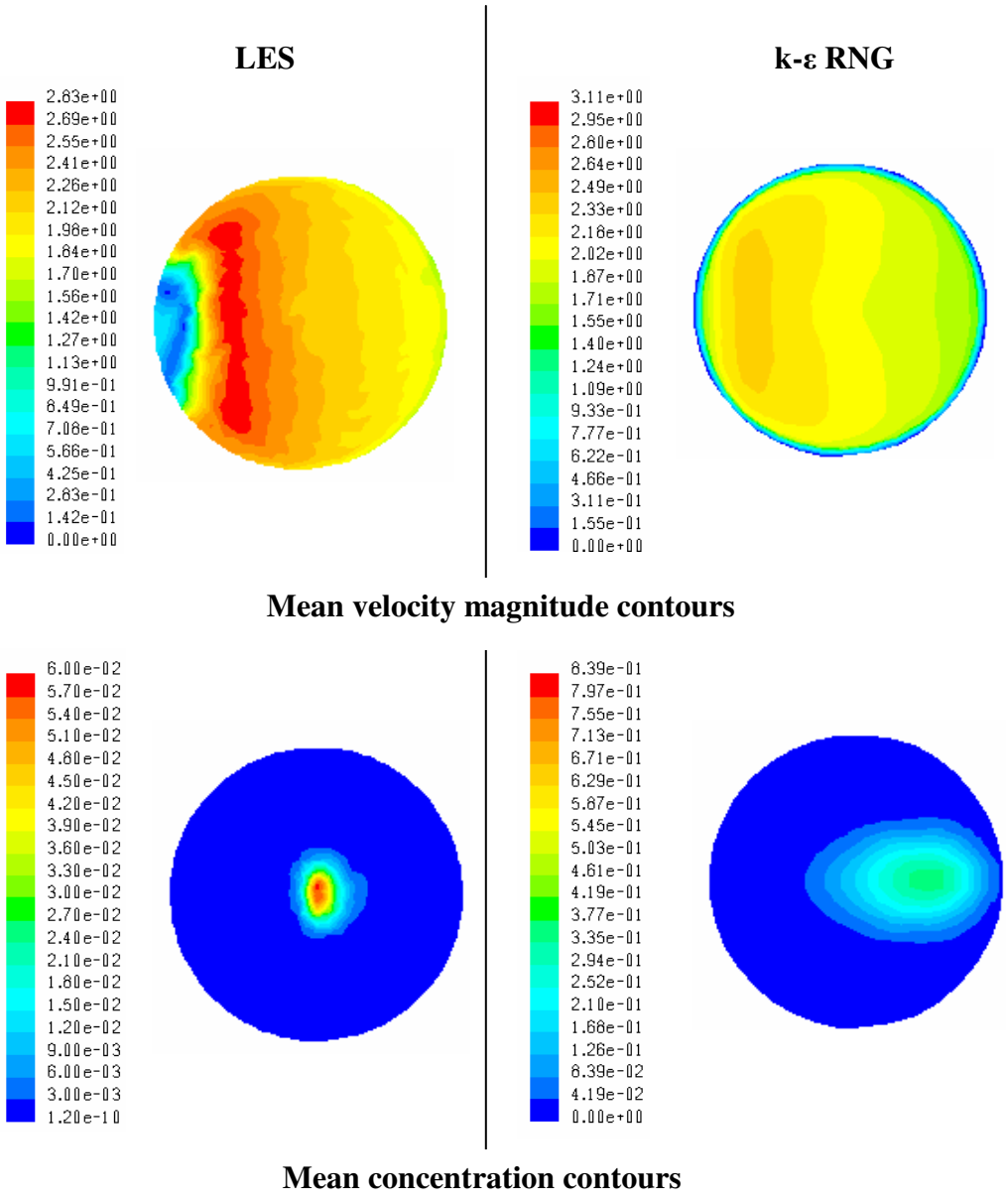

Figure 4.12: The contours of mean velocity magnitude and concentration from LES and RANS (k-ε RNG) simulations at the exit plane of the elbow are compared.

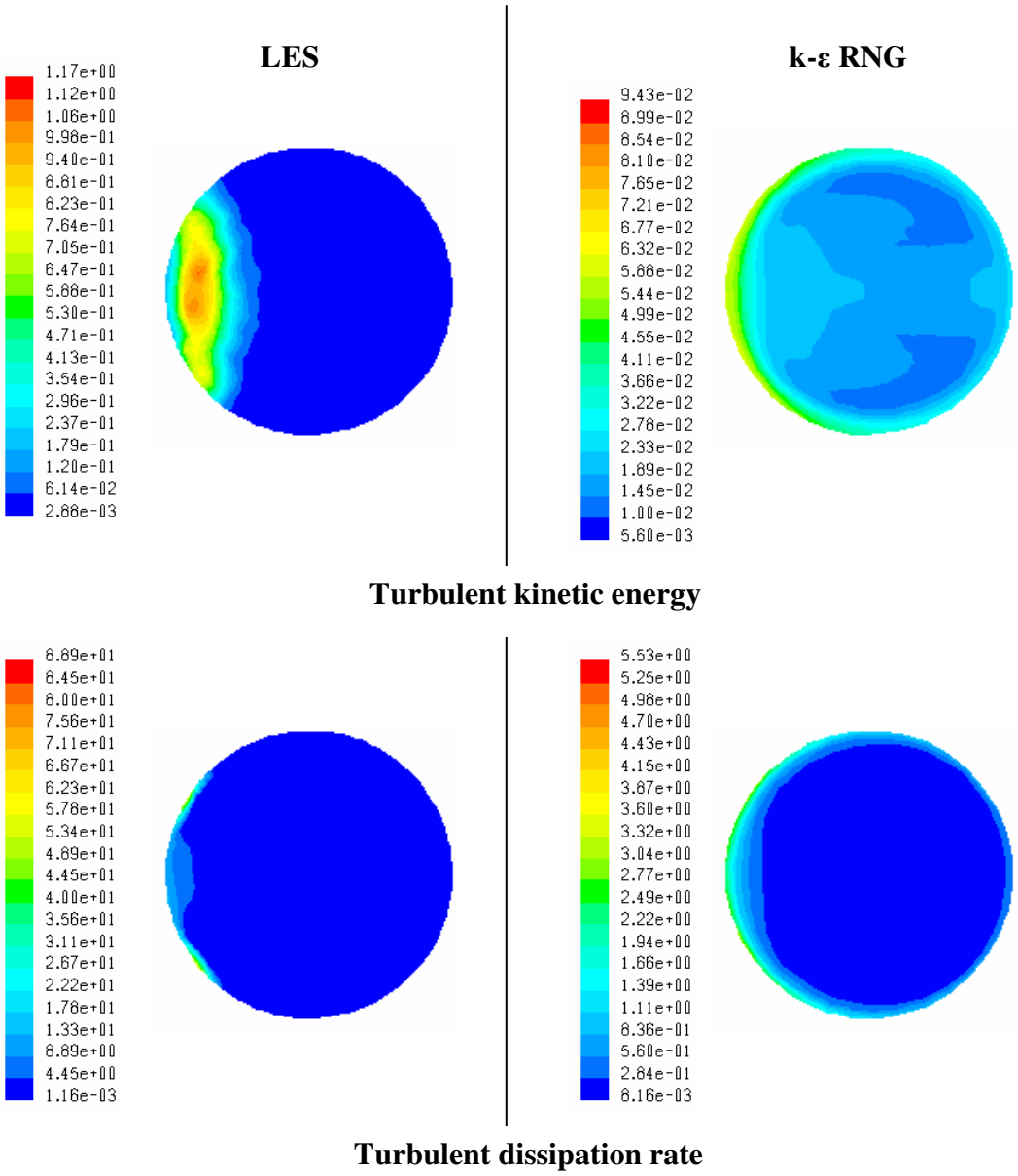

Figure 4.13: The contours of turbulent kinetic energy and turbulent dissipation rate from LES and RANS (k-ε RNG) simulations at the exit plane of the elbow are compared.

In Figure 4.13 the turbulent kinetic energy and turbulent dissipation rates at the exit plane of the elbow from the LES and RANS simulations are compared. We can see that the structure of turbulent kinetic energy and dissipation rate are significantly different for the LES and RANS simulations. For both turbulent kinetic energy and turbulent dissipation rate there are two symmetric pockets of maxima in the inner side of the elbow from the LES simulations whereas these quantities are uniformly high in the inner side of the elbow for the RANS simulations.

The turbulent kinetic energy and turbulent dissipation rate are obtained from the LES simulations using Equations [4.1] and [4.2] respectively. In Fluent ™ (version 6.1.22) there is no straight forward method to calculate the kinetic energy and dissipation from the results of the LES simulation. Turbulent kinetic energy was calculated using *rms* value of velocity fluctuations. A custom variable, $U_{i,k}U_{i,k}$ was defined and from the mean of this variable and the mean value of the velocities the turbulent dissipation rate was obtained using Equation [4.2].

$$\text{Tubulent kinetic energy, } k = \frac{1}{2}\left(\overline{u_i u_i}\right) = \frac{1}{2}\left(\overline{U_i U_i} - \overline{U}_i \overline{U}_i\right) \qquad [4.1]$$

$$\text{Tubulent dissipation rate, } \varepsilon = \nu\left(\overline{\frac{\partial u_i}{\partial x_k}\frac{\partial u_i}{\partial x_k}}\right) = \nu\left(\overline{U_{i,k}U_{i,k}} - \overline{U}_{i,k}\overline{U}_{i,k}\right) \qquad [4.2]$$

The velocity and concentration COV predictions from the hybrid RANS/LES simulation as well as RANS and LES simulations are shown in Figure 4.14 and Figure 4.15 respectively. It can be seen from Figure 4.14 that up to a distance of about 4 diameters downstream of the exit plane of the elbow, the prediction of the hybrid RANS/LES scheme is the closest to the experimental value. Further downstream of the elbow, the RANS predictions for the velocity COV are closer to the experimental value than either the LES or the hybrid RANS/LES schemes.

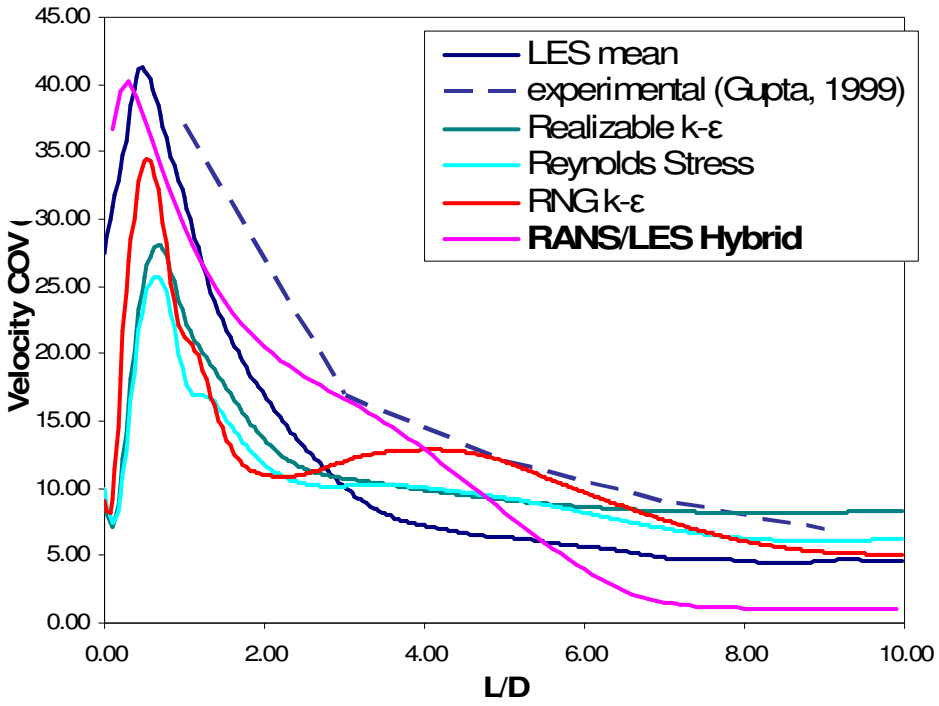

Figure 4.14: The velocity COVs downstream of a 90° elbow for different turbulence models is plotted against the non-dimensional distance downstream of the elbow.

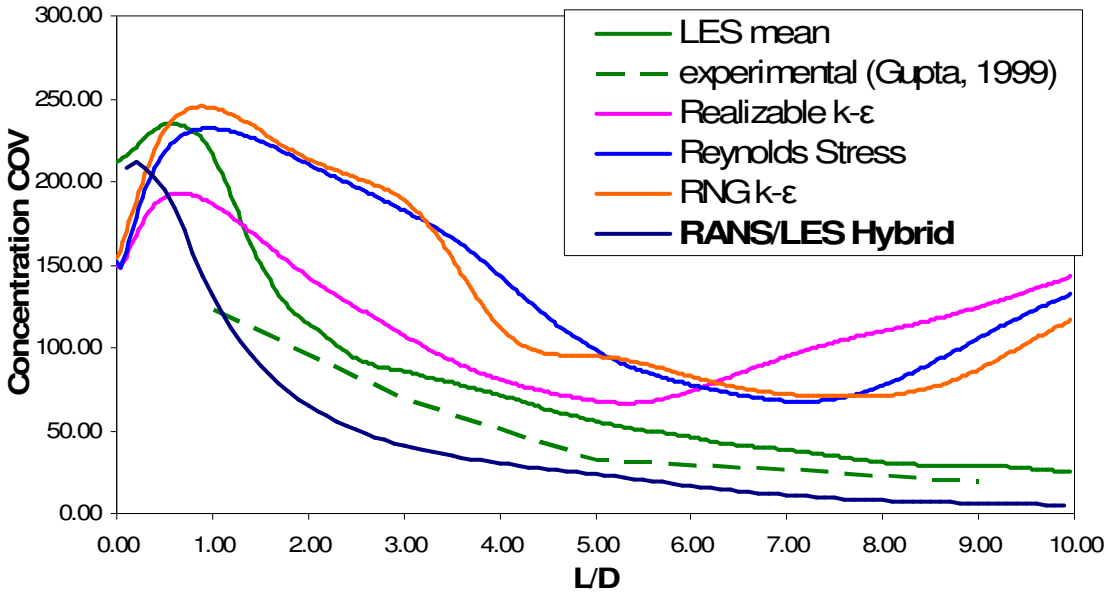

Figure 4.15: The concentration COVs downstream of a 90° elbow for different turbulence models is plotted against the non-dimensional distance downstream of the elbow.

Comparison between a static Smagorinsky sub-grid scale model and a dynamic Smagorinsky sub-grid scale model

The contour plots of velocity magnitude in the symmetric plane of the elbow for static and dynamic subgrid scale models are shown in Figure 4.16 and Figure 4.17. From the contour plots it can be seen that there is not a considerable difference in the prediction of the two models in development of momentum downstream of the elbow.

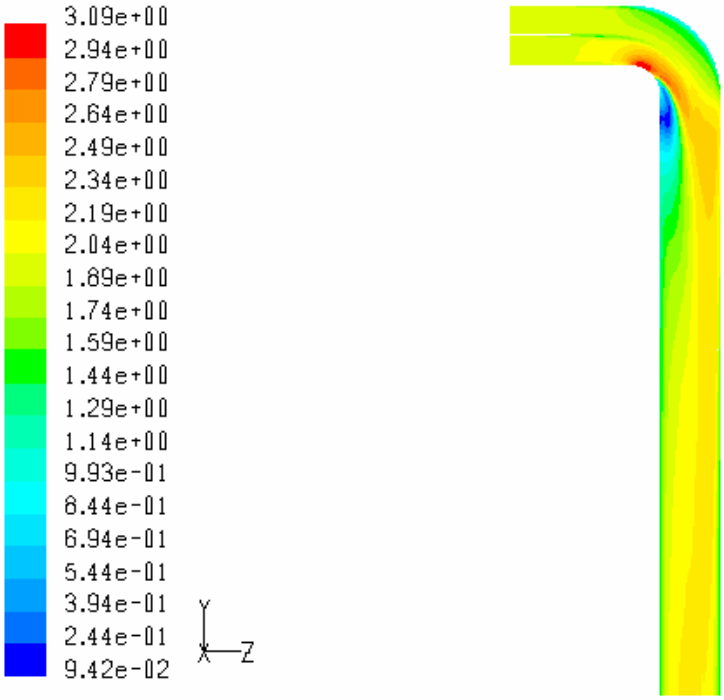

Figure 4.16: Velocity magnitude contours (Static sub-grid scale model).

The main difference in velocity contours between the two models can be seen in the inner region of the elbow and the inner region just downstream of the elbow. The development of momentum is similar in all other regions. Due to significant secondary flow, the momentum from the inner region is transferred to the outer region. The outer region has a larger momentum than the inner region for a significant distance downstream of the elbow, until finally due to turbulent dispersion, the velocity profile tends to the fully developed flow profile.

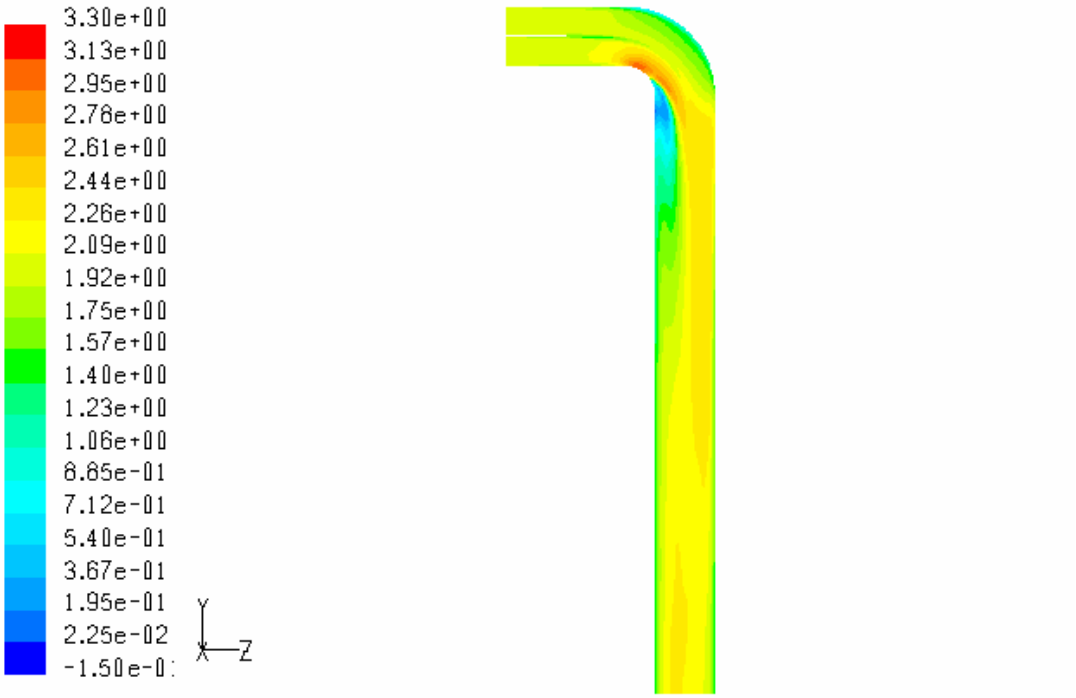

Figure 4.17: Velocity magnitude contours (Dynamic sub-grid scale model).

Figure 4.18 through Figure 4.22 plot the mean and *rms* profiles for velocity magnitude, x, y and z velocity and concentration. The profiles are plotted on lines in the symmetric mid-plane running from the inner to outer edge in the z-direction. The profiles are plotted on four different lines at a distance 0, 3, 6 and 9 diameters from the exit plane of the elbow.

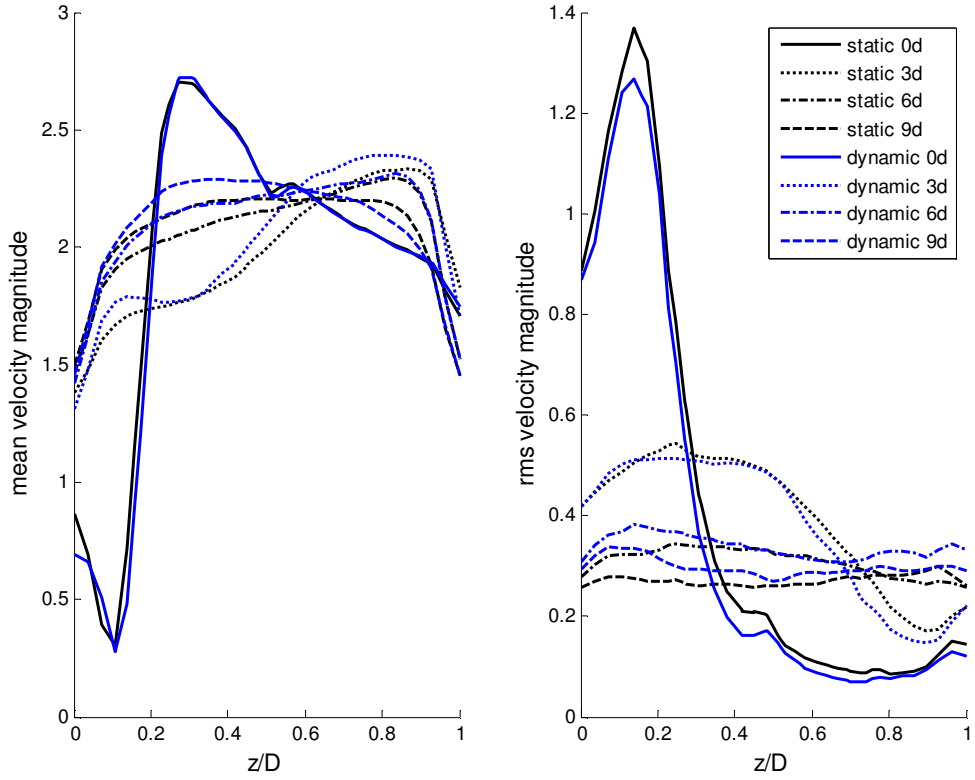

Figure 4.18: Mean and *rms* velocity magnitude for static and dynamic sub-grid scale models at distances of 0, 3, 6 and 9 diameters downstream of the exit plane of the elbow. Velocity is given in m/s.

In Figure 4.18 we can see that as the distance from the elbow increases the variation in the velocity profile decreases and the turbulence intensity also decreases. At the exit plane of the elbow, there is considerable turbulence in the inner side of the elbow compared to the outer side. The predictions of the static and dynamic sub-grid scale models are close to each other in the highly turbulent region and they match less closely as we go further downstream. This is because in the elbow region, there is a formation of larger scales and as the larger scales dominate the influence of smaller

scales is less. Therefore the choice of sub-grid scale model does not matter much. But as we start going further downstream, due to cascading smaller scales are formed and their influence increases. Therefore the choice of sub-grid scale model becomes more important. The dynamic sub-grid scale model predicts a larger dispersion of momentum and therefore lesser variation in the velocity profile as we go further downstream from the exit plane of the elbow.

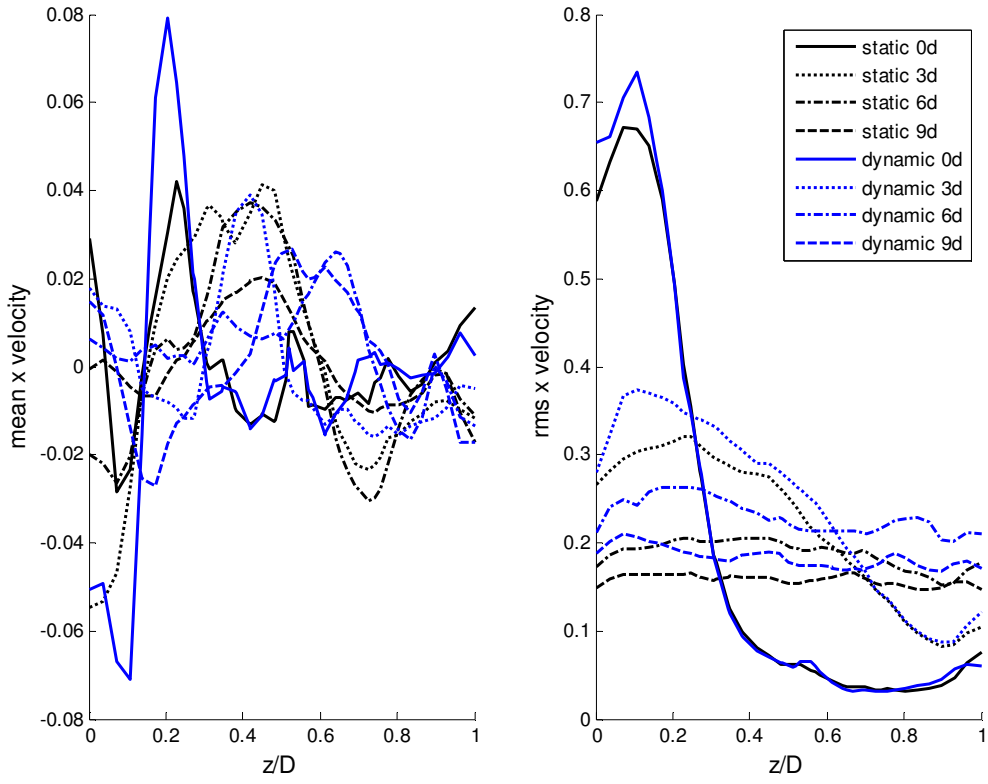

Figure 4.19: Mean and *rms* x-velocity for static and dynamic sub-grid scale models at distances of 0, 3, 6 and 9 diameters downstream of the exit plane of the elbow. Velocity is given in m/s.

From Figure 4.19 it can be seen that the two models do not compare well as we get further downstream from the elbow. As explained earlier this is due to the production of smaller scales due to cascading.

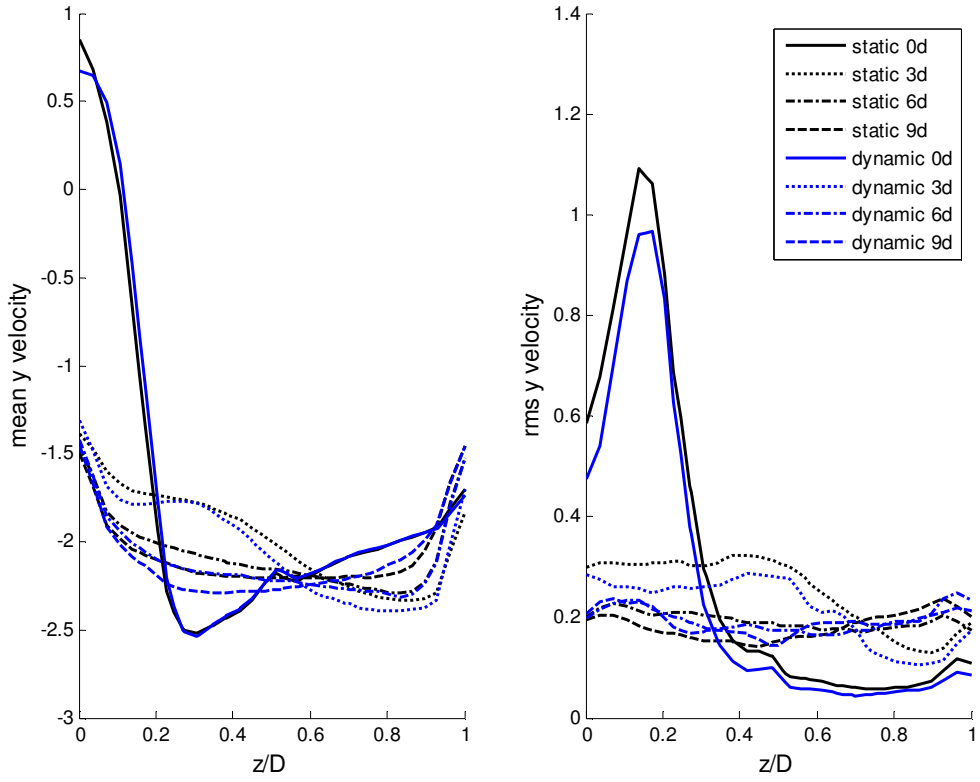

Figure 4.20: Mean and *rms* y-velocity for static and dynamic sub-grid scale models at distances of 0, 3, 6 and 9 diameters downstream of the exit plane of the elbow. Velocity is given in m/s.

Figure 4.20 and Figure 4.21 are similar to Figure 4.18, except for the fact that the static and dynamic sub-grid scale models show better agreement for the y and z-velocities than they did for the x-velocity. The y-velocity is opposite to the direction of the bulk flow near the inner region of the elbow at the exit plane of the elbow. This is due to the presence of a vortex in the inner region of the elbow. This vortex causes flow switching to occur.

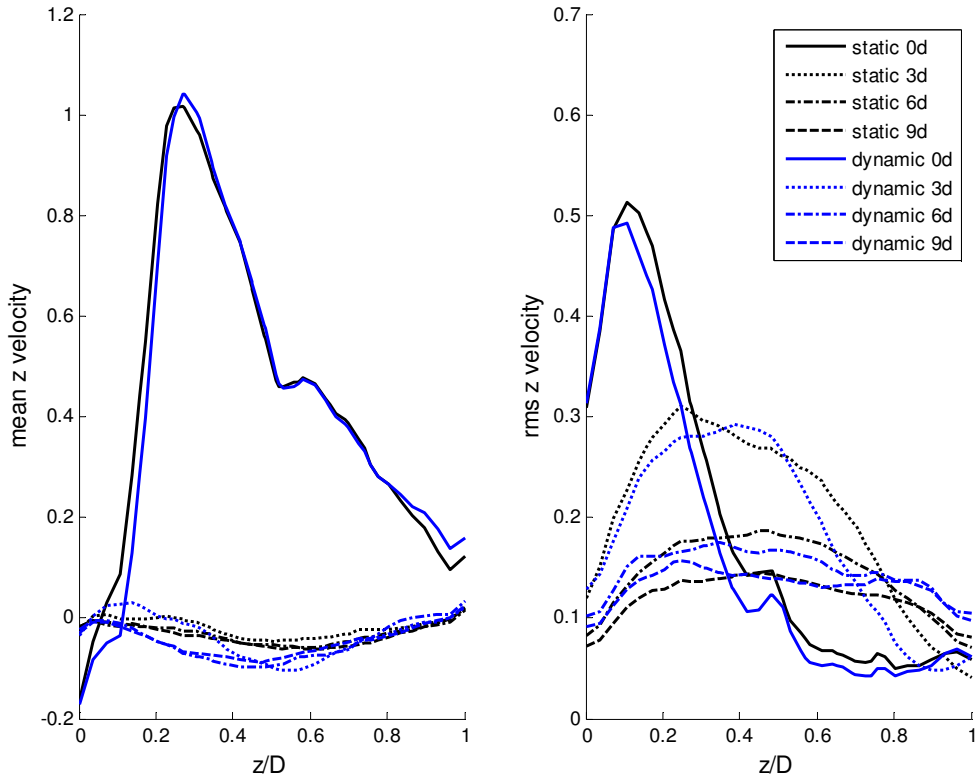

Figure 4.21: Mean and *rms* z-velocity for static and dynamic sub-grid scale models at distances of 0, 3, 6 and 9 diameters downstream of the exit plane of the elbow. Velocity is given in m/s.

From Figure 4.21, the z-velocity at the exit plane of the elbow is much higher compared to the z-velocity downstream of the exit plane of the elbow. This can be explained by the presence of a dominant secondary flow at the exit plane of the elbow.

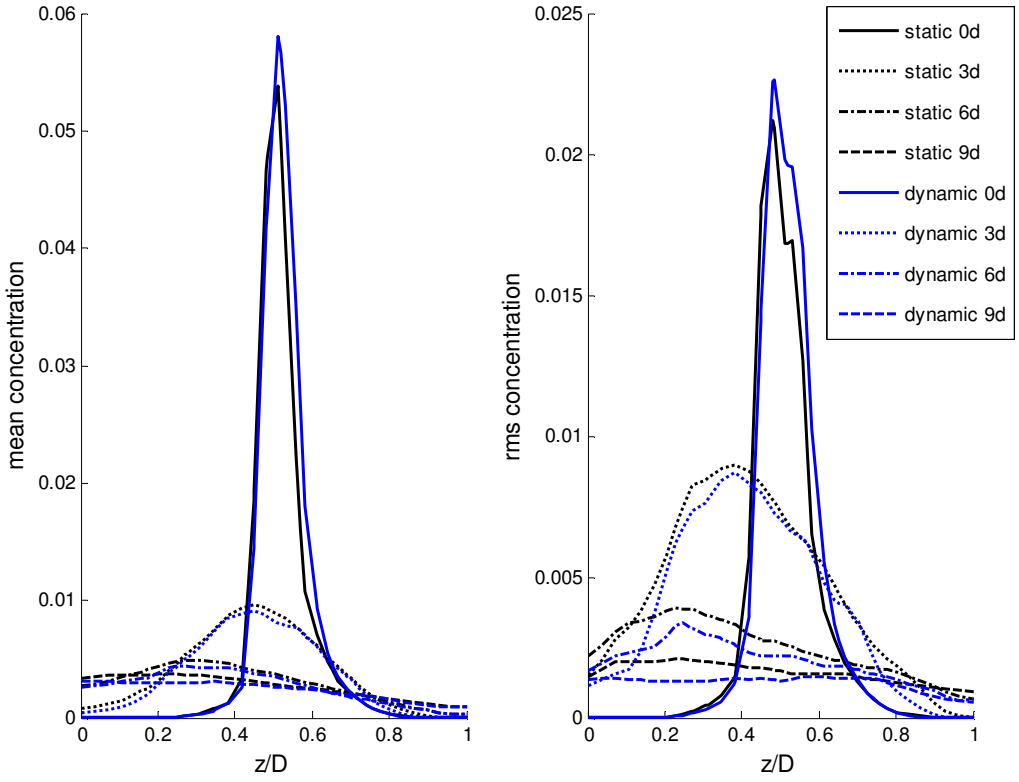

Figure 4.22: Mean and *rms* concentration for static and dynamic sub-grid scale models at distances of 0, 3, 6 and 9 diameters downstream of the exit plane of the elbow. Concentration is specified as species mass fraction.

From Figure 4.22 it can be seen that the concentration is fairly uniform at a distance of 9 diameters from the exit plane of the elbow. Also in general, the higher the

mean concentration, the higher is the *rms* value of the concentration. From Figure 4.18 through Figure 4.22 it can be seen that in most cases the comparison between the two models is fairly good. This is mainly due to the fact that the larger scales are more important for the bulk transfer of momentum and species compared to the smaller scales.

Animations of concentration and velocity magnitude contours were obtained at the exit plane of the elbow and the symmetric mid plane. A still picture from the animations is shown in Figure 4.23. From the concentration animation at the exit plane of the elbow, the fluctuation in the flow can be observed. From the animation of velocity magnitude at the exit plane of the elbow, the occurrence of flow switching sides can be observed. From the concentration animation in the mid plane, the structures of turbulence and vortices can be seen. The development of the concentration is similar to the dye visualization done experimentally. The development of momentum can be seen from the velocity magnitude animation at mid plane of the elbow. Notice the low velocity region in the inner region downstream of the elbow indication separation of flow.

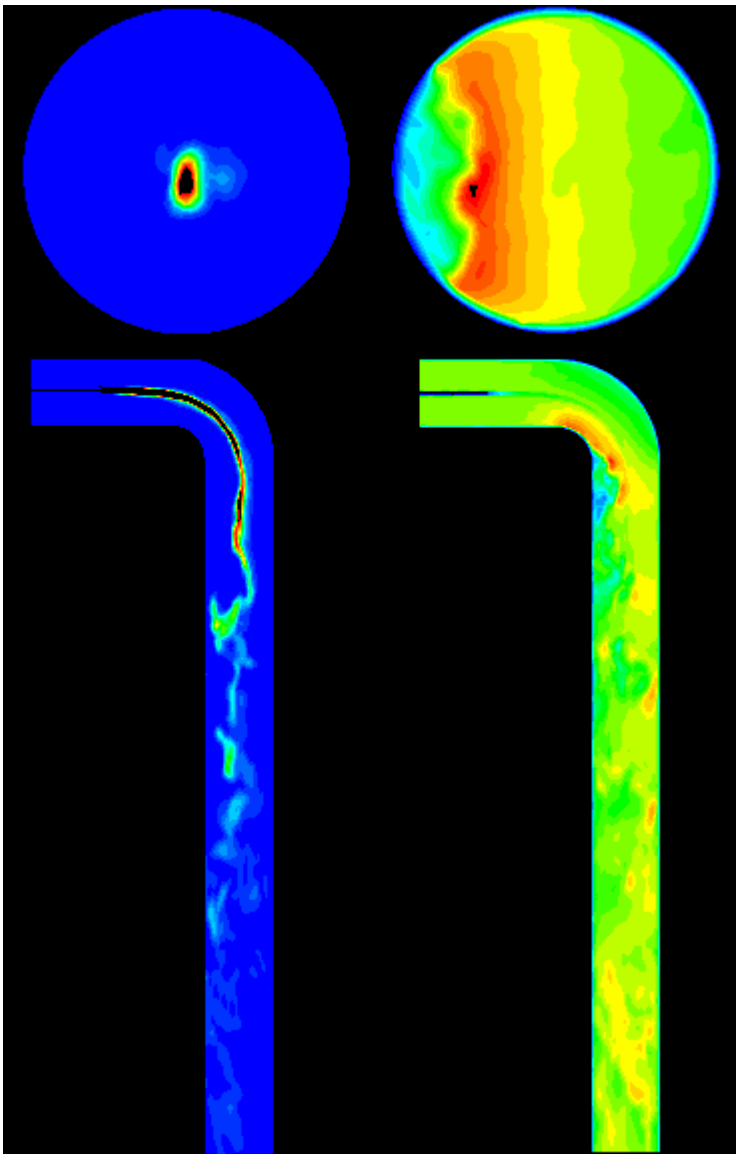

Figure 4.23: A frame from concentration and velocity contour animations.

Flow visualization

Flow visualization experiments using a dye (blue food coloring) released from a needle was performed for the flow of water through a straight tube.

1 2

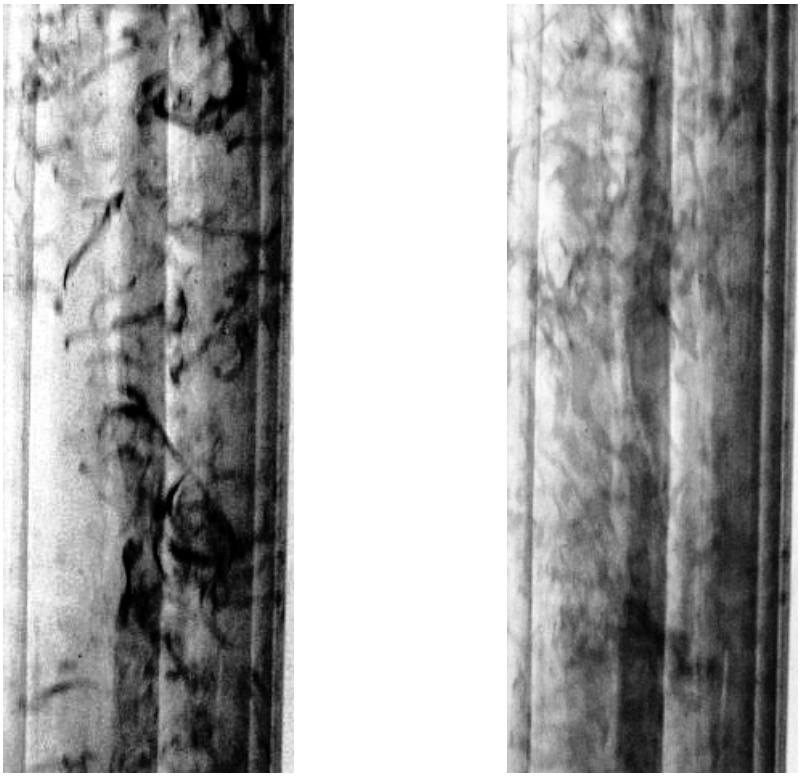

Figure 4.24: The instantaneous (1) and mean (2) dye profiles are shown (before subtracting the background, with glare).

Figure 4.24 shows the processed instantaneous and mean dye profiles. The image processing was done by converting the color image to a gray scale image, and then scaling the gray scale so that it spans the entire range from 0 to 255. The photos were cropped to include only the tube.

Figure 4.25 shows the COVs (calculated based on the data on a line across the cross-section of the tube) along the direction of the flow. The mean dye profile was

actually a mean of 5 different instantaneous values. That is why the mean profile is non-uniform, but compared to the instantaneous dye profile we can see that the mean profile is more uniform.

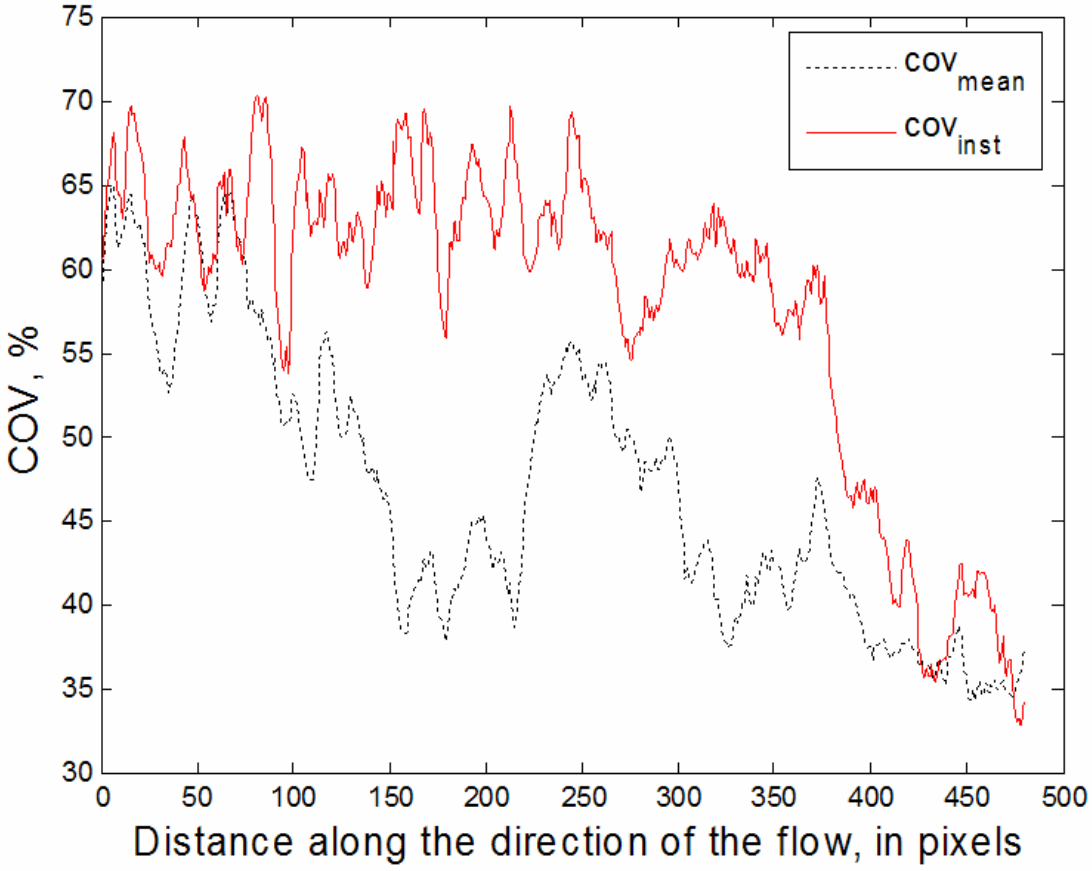

Figure 4.25: The instantaneous (1) and mean (2) COV profiles are shown (before subtracting the background, with glare).

1 2

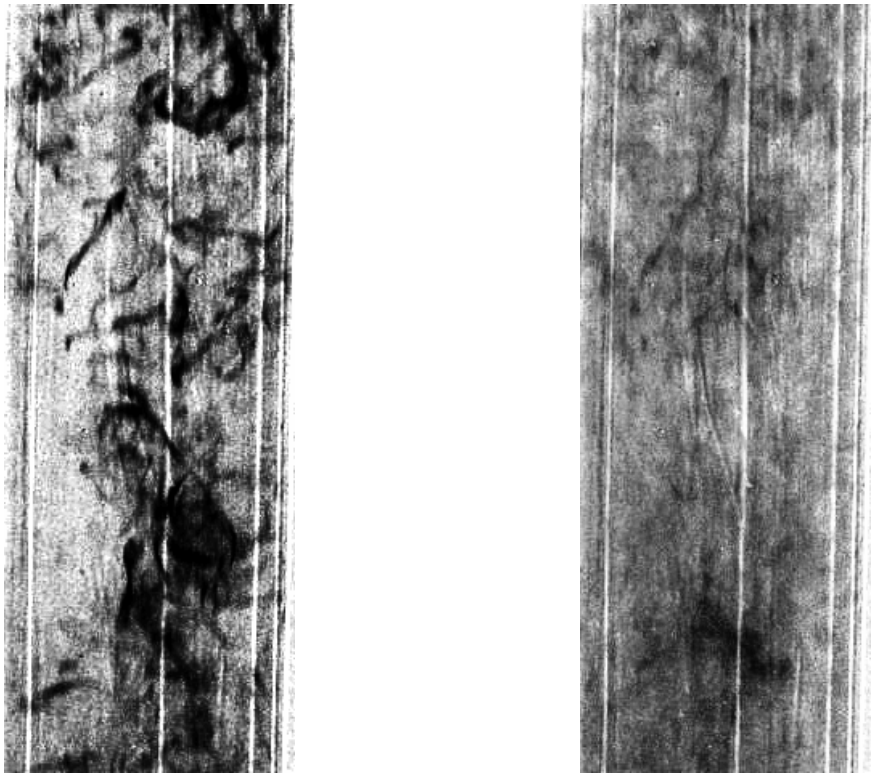

Figure 4.26: The instantaneous (1) and mean (2) dye profiles are shown (after subtracting the background, without glare).

Figure 4.26 and Figure 4.27 are similar to Figure 4.24 and Figure 4.25 respectively, except that the background (with no dye in the flow) has been subtracted from the dye profiles. We can see that subtracting the background has removed the glare from the glass to some extent.

Nevertheless, we do see artifacts (the vertical white lines) which are caused due to light reflection from the glass. To prevent these artifacts, we are planning to use a polarizing filter, along with more uniform backlighting.

Normally, the COV is calculated using two dimensional data across a cross section. In these experiments we are able to get only one dimensional data across cross sections. Therefore, one way to address this would be to use two perpendicular cameras and translucent dye, the details of this approach is still being worked out.

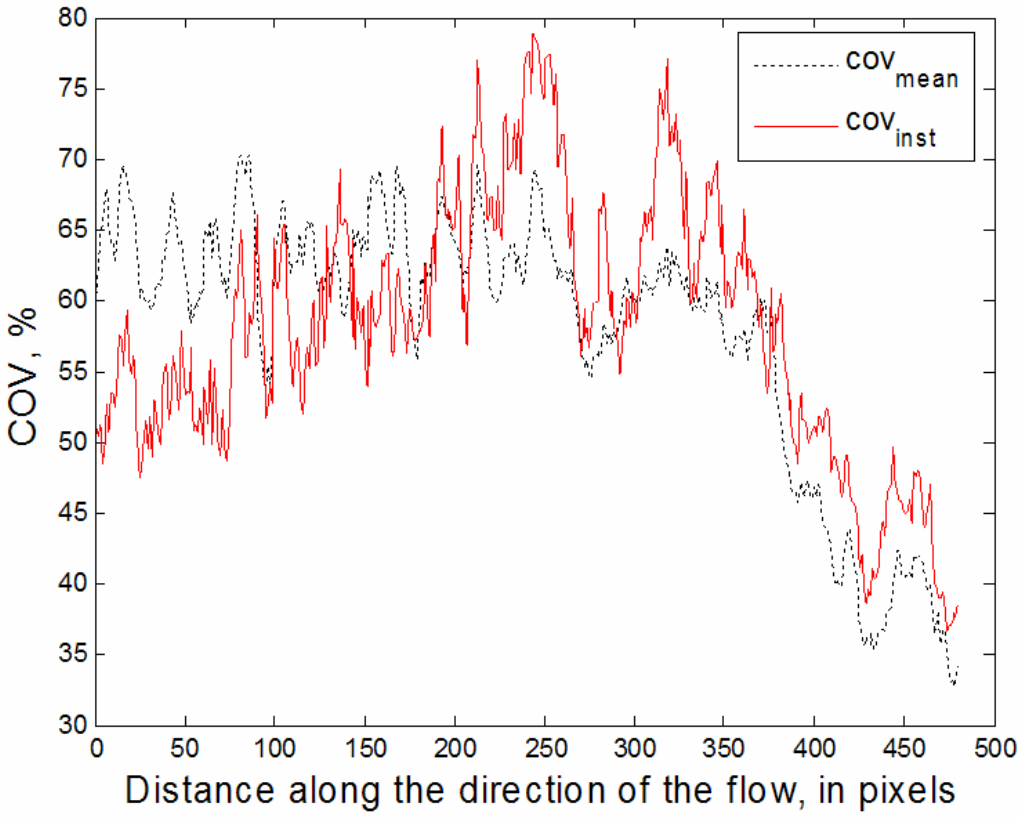

Figure 4.27: The instantaneous (1) and mean (2) COV profiles are shown (after subtracting the background, without glare).

The lighting issues for the experiment need to be addressed. The lighting has to be uniform to prevent the dye intensity values from being affected because of the lighting. One of the ways to achieve this is to conduct the experiment in a dark room and use a uniform backlight (probably phosphorescent lighting). The glare created in the photos is one of the main concerns. Polarizing filters are to be used to prevent the glare, while taking photos or videos. A way to correlate the COV with 'two dimensional cross-sectional intensity data collapsed to one dimension line data' is to be developed. For this approach to be effective, I believe that we need to use translucent dye instead of an opaque dye. The larger the number of translucent layers, the more opaque it will look in one dimension. Therefore we can use the opacity (or intensity) to correlate it with COVs.

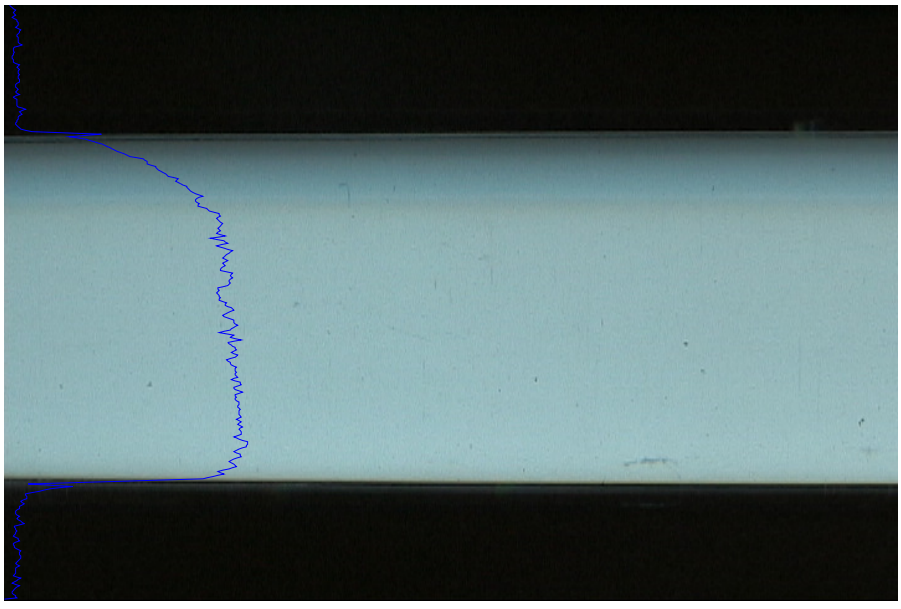

Figure 4.28: The intensity of the backlight is plotted as a function of the cross stream position.

To improve the contrast of the dye against the background a white fluorescent light was used to provide backlighting. Backlighting, to large extent eliminated the problem of glare and provided a uniform background for studying the mixing of the dye. We can see from Figure 4.28 that the intensity of the backlight is fairly uniform across the cross-section. The exception to this uniformity is the intensity distribution near the top edge of the tube. Due to the glare and other refraction effects the gradient of the light intensity near this edge is not as high as we would like it to be. But the light intensity curve has a steep gradient along the lower edge of the tube.

The dye used has a bluish-green (turquoise) color. The way the dye optically obtains its color is by absorbing all other wavelengths of light except those in the bluish-green range. Therefore if we filter the color image into its RGB components, the R component is the most affected because of the light. This can be seen in Figure 4.29, where the R component is much darker compared to the G and B components of the image. The background light has nearly an equal distribution of the R, G and B components (pure white light). Due to the above reason, we will use only the R-component of light for our quantification purposes.

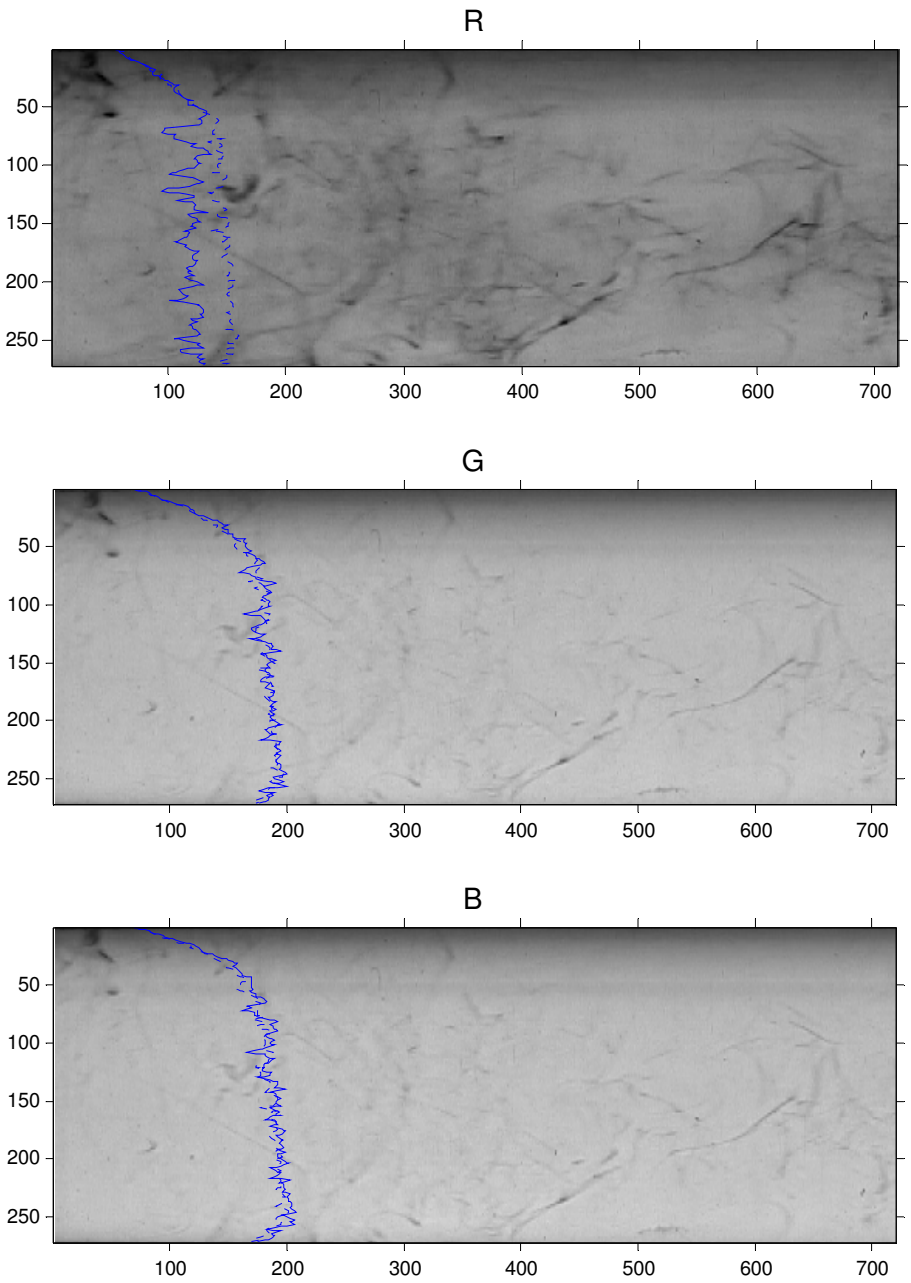

Figure 4.29: The intensity of the image with the dye (solid lines) introduced for the R, G and B is plotted. The background intensity is plotted as dotted lines for comparison.

Figure 4.30 plots the background intensity, the intensity with the dye and the difference between the two intensities. From Figure 4.30 we can see that though the intensity spread of the background light (mean = 148.2, stdev = 5.7) is lesser than that of the image with the dye (mean = 119, stdev = 8.2), the intensity spread of the background light is still significant and cannot be ignored. Therefore we will need to find a more uniform lighting or check to see if the variation in light intensity can be included in the correlation with the dye concentration.

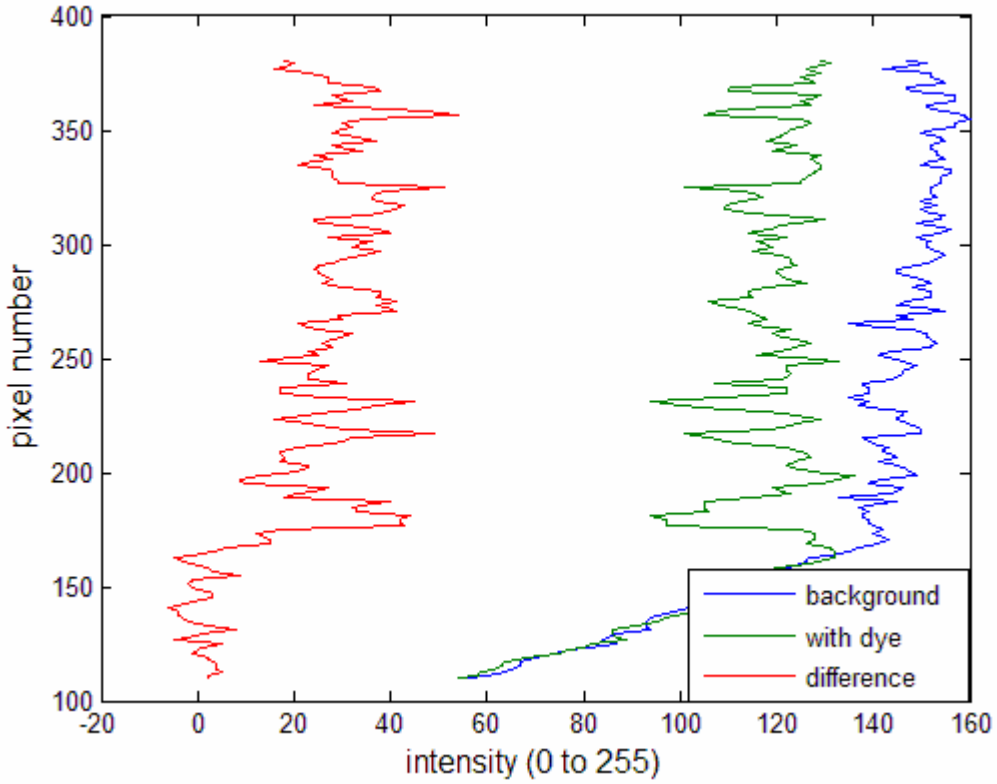

Figure 4.30: The background intensity, the intensity with the dye and the difference between the two intensities are plotted.

5. EFFECT OF PARTICLE CHARGE AND TRANSPORT LINE CONDUCTIVITY ON PARTICLE DEPOSITION

Introduction

This study describes the design and testing of a prototype aerosol transport system intended to collect two continuous equal flow rate aerosol samples from separate aspiration plenums placed over the primary pinch-points of two mail sorting machines, combine the samples into a single aerosol stream, and then deliver the combined sample to a biological detection system (BDS). Of prime importance to the design of the aerosol transport system was the need to locate the BDS adjacent to one of the two mail sorting machines, yet require no active control to ensure that the two extracted samples would be of (nominally) equal flow rate. For this reason, the transport system design called for a flow combiner to be placed at the midpoint between the two sorting machines, allowing the transport system to be symmetric with respect to the two sample legs, thus providing high probability that the two extracted sub-samples would be of equal flow rate when a single vacuum pump was used for aspiration of the combined sample at the BDS location (Figure 5.1). The design flow rates for each sub-sample were selected to be 200 L/min so the combined flow rate delivered to the BDS location would be 400 L/min.

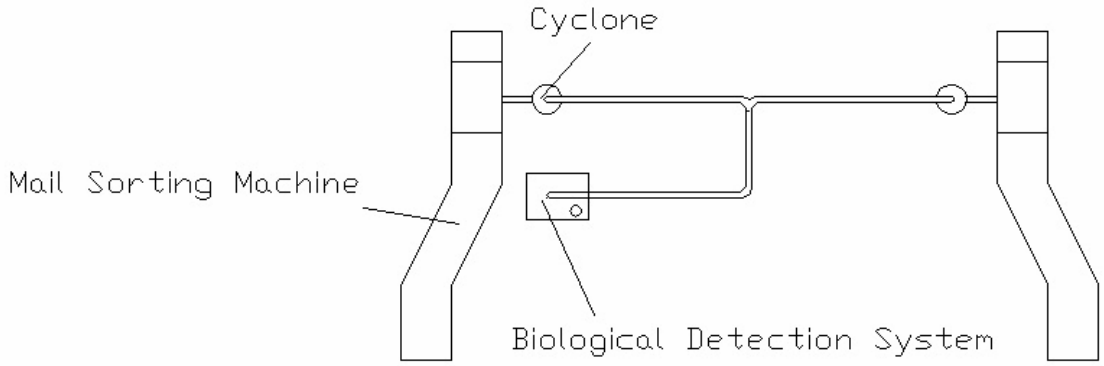

Figure 5.1: Schematic of the transport system.

A primary consideration for the design of an aerosol transport system is selection of the particle size range of interest for the combined sampling and detection system. For the present study, the size range of interest was taken to be all particles up to a size of 10 μm aerodynamic diameter (AD), the largest size that particle that can effectively penetrate into the thoracic region of the human lung and the upper size limit associated with most air quality research. Although 10 μm AD is a size significantly larger than that associated with single bacteria spores, previous studies have shown that a relatively small number of large spore clusters can represent a significant fraction of the total bacteria released from a piece mail in a sorting machine (Richardson 2003).

To prevent clogging of the transport components or the BDS, it was assumed that it would be necessary to exclude unwanted large particles (>10 μm AD) and debris from the aerosol sample. To facilitate the removal of debris, the transport system was expected to incorporate one or more aerosol fractionating cyclones for removal large particles. Additional constraints on the system design were that the system should use

low-cost tubing and materials where possible, and that the system be simple to transport, assemble, install and maintain.

The studies reported below describe the procedures used to select the component dimensions as well as the results of the aerosol transport efficiency experiments. Here, an aerosol transport component is taken as any distinct tube, bend, connector, combiner or cyclone that is part of the overall aerosol transport system.

Selection of transport tubes

Theoretical calculation of optimum tube diameter

In general, the transport efficiency of an aerosol sampling system decreases with increasing particle size, thus the transport system should be optimized for the largest particle size of interest. For the theoretical analysis of this study, a particle cutpoint size of 11 μm AD was selected in order to prevent significant loss of the sample of interest in the transport lines or cyclone fractionators. In a hypothetical transport system shown in Figure 5.1 having both bends and horizontal tube segments, significant losses of particles of this size can be expected due to particle collisions with the transport tube walls. Particles that contact the tube walls will remain attached to the wall surface due to the overwhelming van der Waals force and are 'lost' from the sample. Two primary mechanisms for particle losses in aerosol transport lines are gravitational sedimentation in tubes with a horizontal directional component, which increases as the transport tube diameter increases for a fixed sample flow rate, and inertial deposition which increases as the transport tube diameter is made smaller. Although in general it is not possible to have a non-horizontal passive aerosol transport line without loss of 10 μm AD particles,

these losses can be minimized for a fixed sample flow rate by selection of an optimum transport tube diameter.

The Aerosol Technology Laboratory of the Texas A&M University System has developed a software package, Deposition 2001a (McFarland et al. 2001), that provides predictions of particle losses in aerosol transport lines. Deposition (McFarland et al. 2001) is able to determine an optimum tube diameter for a given transport line configuration to maximize the transport efficiency of a given particle size. However, such an analysis is valid only for a single flow rate. Because the proposed configuration of the dual collection system involves flow rates of both 200 L/min and 400 L/min, a separate Deposition (McFarland et al. 2001) analysis was performed for the respective segments of the transport system. Segment 1 having a flow rate of 200 L/min was taken to be the portion of the sampling system from the outlet of the fractionating cyclone (if present) to the flow combiner. Segment 2 having a flow rate of 400 L/min was taken as the portion of the sampling system from the outlet of the combiner to the inlet of the BDS. Note that a dual collection system would have two Segment 1 sample lines followed by the combiner. Diagrams and descriptions of the inputs to the Deposition (McFarland et al. 2001) modeling of the two segments are given in Figure 5.2 and Figure 5.3 and Table 5.1 and Table 5.2.

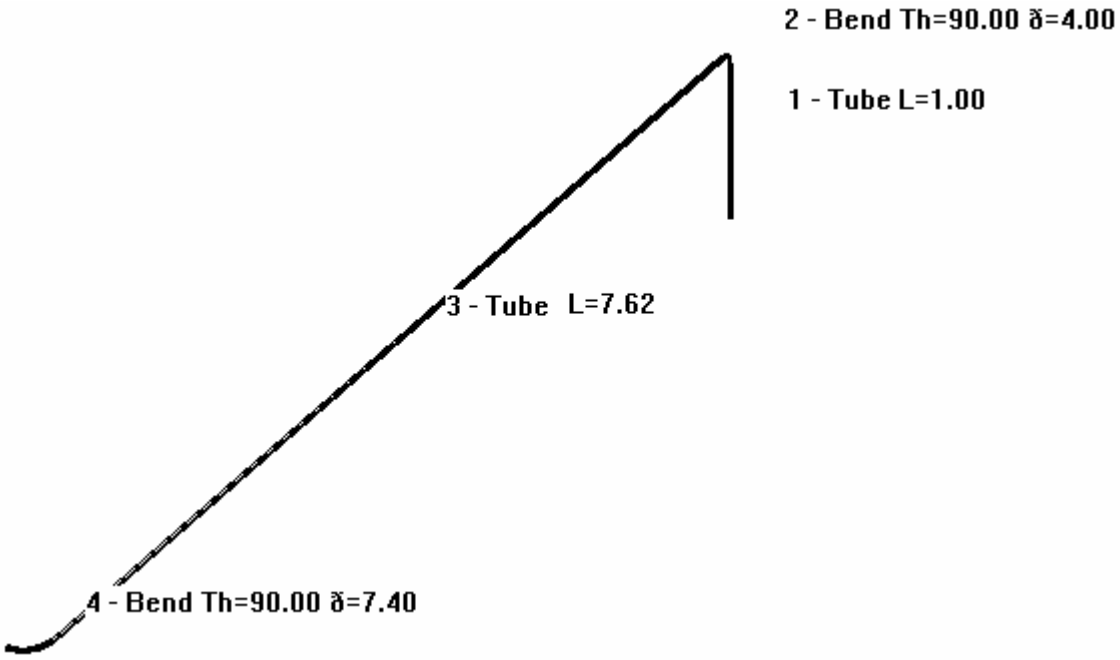

Figure 5.2: Deposition (McFarland et al. 2001) software rendering of Segment 1 of the aerosol transport system.

Table 5.1: Deposition (McFarland et al. 2001) software Transport System Components used for modeling of particle deposition in Segment 1 of the aerosol transport system.

Segment 1: Flow rate = 200 L/min				
Component #	**Component**	**Length (m)**	**Curvature Ratio**	**Orientation**
1	**Tube**	1	--	Vertical
2	**Bend**	--	4	--
3	**Tube**	7.6	--	Horizontal
4	**Bend**	--	7.4	--

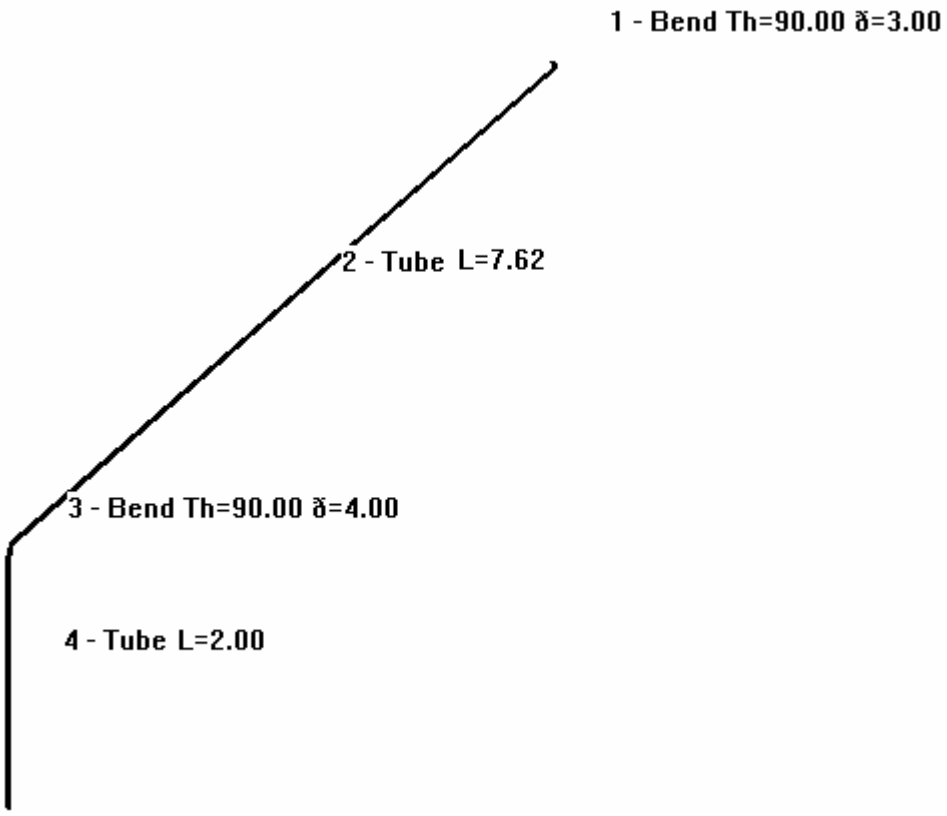

Figure 5.3: Deposition (McFarland et al. 2001) software rendering of Segment 2 of the aerosol transport system.

Table 5.2: Deposition (McFarland et al. 2001) software Transport System Components used for modeling of particle deposition in Segment 2 of the aerosol transport system.

Segment 2: Flow rate = 400 L/min				
Component #	**Component**	**Length (m)**	**Curvature Ratio**	**Orientation**
1	**Bend**	--	3	--
2	**Tube**	7.6	--	Horizontal
3	**Bend**	--	4	--
4	**Tube**	2	--	Vertical

The two transport segments were analyzed using Deposition 2001a (McFarland et al. 2001) to obtain the optimum tube diameter for maximum penetration, and the results are given in Figure 5.4 and Figure 5.5. The optimum tube diameter for transport of 11 μm AD particles for Segments 1 and 2 were 40 mm and 55 mm, respectively. The transport efficiency for 11 μm AD particles for the optimum tube diameters was predicted to be 66.9% and 76.2% for the two segments.

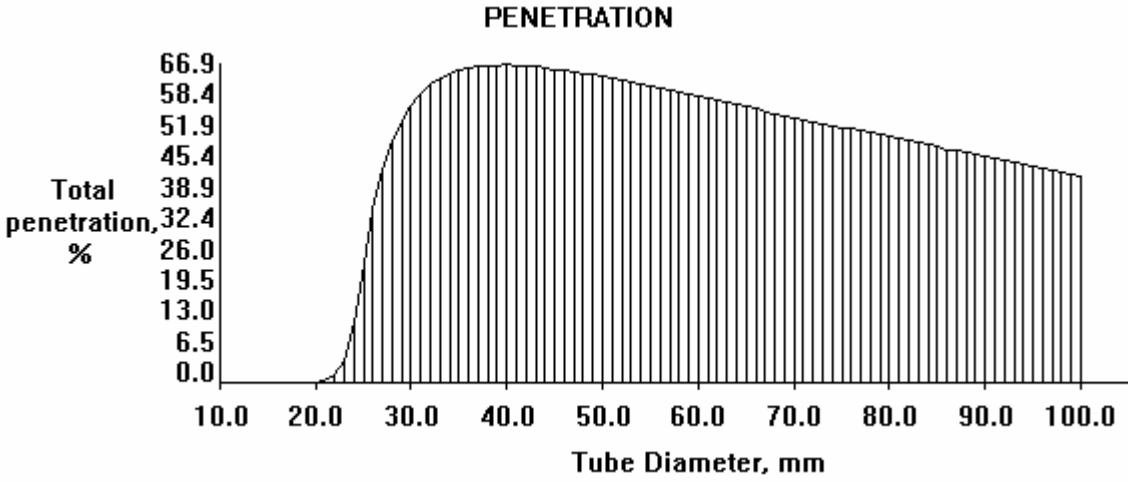

Figure 5.4: Deposition (McFarland et al. 2001) prediction of particle penetration through Segment 1 for different tube diameters (Flow rate = 200 L/min, Particle size = 11 μm AD, Optimum tube diameter = 40 mm, Penetration of particles at optimum tube diameter = 66.9%).

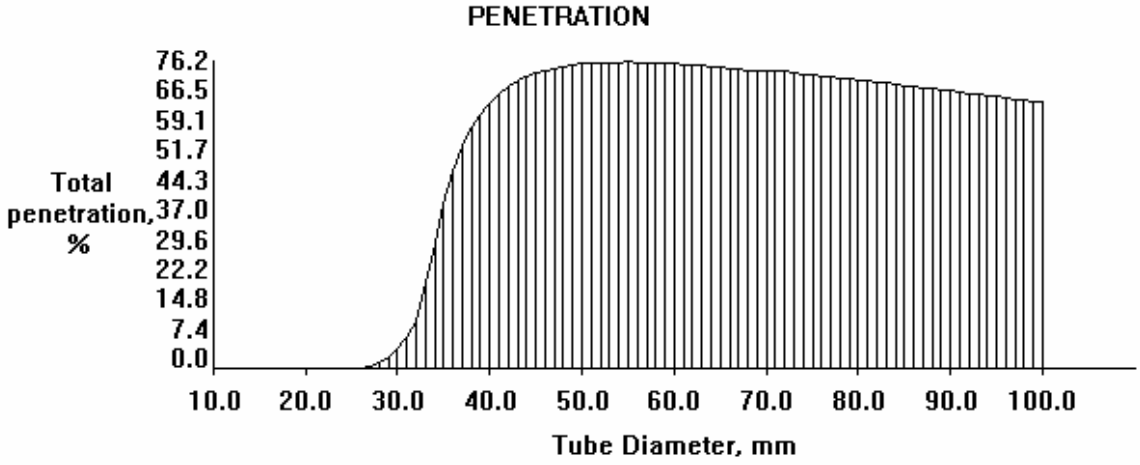

Figure 5.5: Deposition prediction of particle penetration through Segment 2 for different tube diameters (Flow rate = 400 L/min, Particle size = 11 μm AD, Optimum tube diameter = 55 mm, Penetration of particles at optimum tube diameter = 76.2%).

Selection of commercially available transport tubes

With determination of the optimum tube diameter for the two segments, a survey of commercially available tube and conduit was conducted to determine products that may be suitable for use in the aerosol transport system. Four candidate materials were procured for testing:

1. Super Flexible Gray PVC Vacuum Hose (Models 5500K32/33, McMaster-Carr Supply Co., Elmhurst, IL)
2. Clear-View General Purpose PVC Dry-Food Hose with Antistatic Wire (Models 5179K24/25, McMaster-Carr Supply Co., Elmhurst, IL)
3. Rigid aluminum conduit (UL Standard 6)
4. Rigid schedule 40 PVC conduit (UL Standard 651)

For each commercial product, the size having internal diameter nearest the optimum diameter was selected for testing. Because the standards that control tolerances on electrical conduits are based upon the product outside diameter, it was not possible to obtain an exact match of the inner diameter for the vacuum hose and conduit products.

Prediction of transport efficiency for commercially available transport tubes

Once the candidate commercial products were identified, the Deposition (McFarland et al. 2001) analysis for 11 μm AD particle penetration for the two segments were re-computed based upon the actual diameters of commercial products selected for study. Also, estimates for the total penetration through the combined system (Segment 1

and 2) were calculated for each tube material by taking the product of the respective transport efficiencies. With reference to Table 5.3, the total penetration for 11 μm AD particles was expected to be approximately 50% for each of the candidate materials.

Table 5.3: Deposition (McFarland et al. 2001) prediction of particle penetration for the different tube materials/sizes selected for study.

Material	Segment 1			Segment 2			Total Penetration (%)
	Nominal Diameter (inches)	Actual I.D. (inches)	Penetration (%)	Nominal Diameter (inches)	Actual I.D. (inches)	Penetration (%)	
Flexible Vacuum Hose	1.5	1.5	66.8	2.0	2.0	75.9	50.7
Aluminum Conduit	1.5	1.624	66.8	2.0	2.083	76.2	50.9
Schedule 40 PVC Conduit	1.5	1.59	66.9	2.0	2.047	76.1	50.9

It should be noted that the Deposition (McFarland et al. 2001) analysis does not account for enhancement of particle losses due to electrostatic deposition, irregularities of tube surface (e.g. the ribbing common to vacuum hose) or losses due to changes in tube cross-section in fittings and joints. Furthermore, this calculation does not consider losses of the sample in the large particle removal cyclones. Thus, the Deposition (McFarland et al. 2001) modeling provides a 'best case' scenario for prediction of transport efficiency.

Design of large particle fractionation cyclone

Considerable effort has been expended in the design and testing of cyclones for the removal of large particles from gas flows in industrial applications. A standard design, the Stairmand-Lapple High Efficiency Cyclone establishes the design for a sharp-cut cyclone that has the desirable properties of a steep collection efficiency curve and relatively low sensitivity to dust loading. The steep fractional efficiency curve allows the cyclone to be designed to have a cutpoint near the upper bound of the size range of interest without creating additional losses to the sample of interest. Because of these properties, the Stairmand-Lapple design was considered the best choice for use as a large particle fractionator for the aerosol transport system.

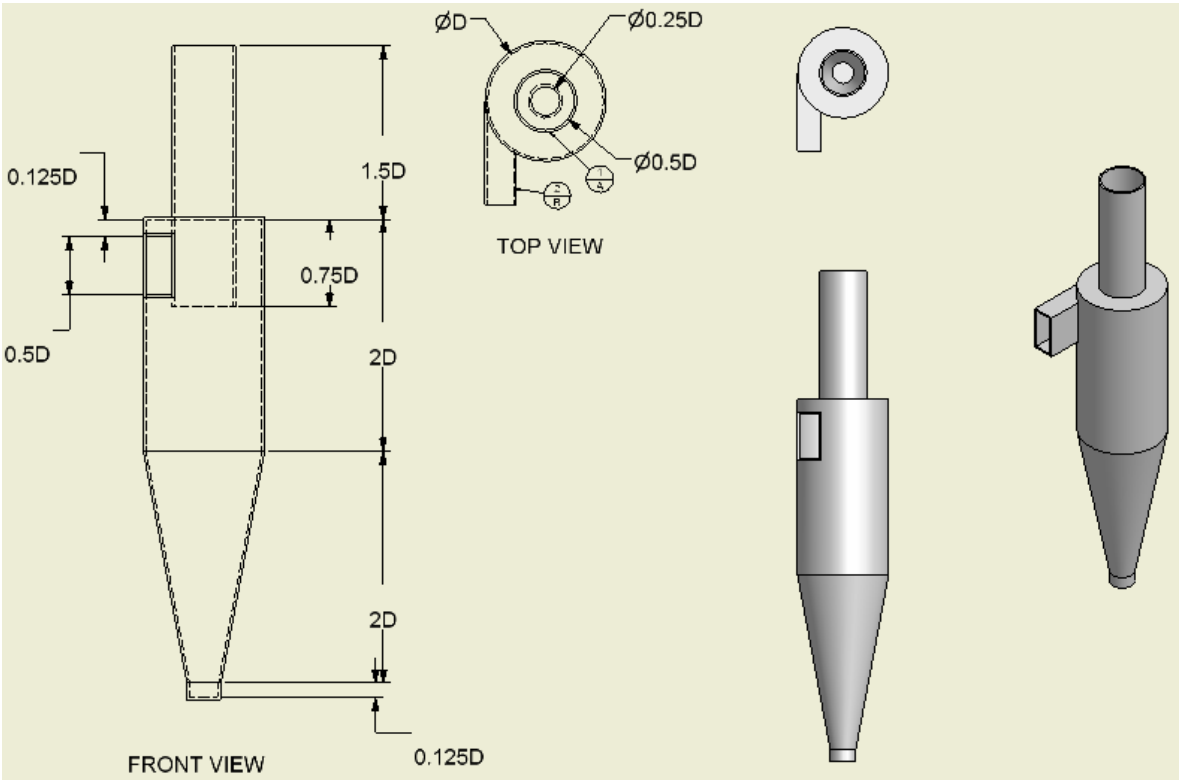

Figure 5.6: Dimensions of the Stairmand High-Efficiency Cyclone.

Moore and McFarland (1993) presented a model allowing for design of arbitrary cutpoint of single inlet cyclones. The diameter, *D*, of the cyclone body is calculated from Equation [5.1]:

$$D = \left[\frac{D_{0.50}}{a} \left(\frac{\mu}{2\rho Q} \right)^{b} \right]^{\frac{1}{1-b}} \qquad [5.1]$$

where the cutpoint, $D_{0.50}$ is 11 μm AD, the flow rate, Q is 200 L/min, the constant, a is 0.053, the constant, b is -0.817, the dynamic viscosity, μ is 1.84e-5 Pa.s and the air density, ρ is 1.19 kg/m^3. Substituting the above values into Equation [5.1] gives the value of cyclone body diameter, D = 0.144 m = 5.65 inches. The dimensions of the cyclone relative to the cyclone body diameter are shown in Figure 5.6.

Experimental methodology

Particle deposition in transport lines

Tests with monodisperse test aerosols were conducted to experimentally characterize the transport efficiency for system components. All transport efficiency tests for the present study were conducted using liquid monodisperse test aerosol droplets generated with a vibrating orifice aerosol generator (VOAG Model 3450, TSI Inc., Shoreview, MN). A solution of ethanol and non-volatile oil (oleic acid) was used in the VOAG for generation of the test aerosols. For the present study, the ratio of ethanol to non-volatile liquid was approximate 10:1, allowing for the generation of 10 μm aerodynamic diameter (AD) aerosol droplets using a 50 μm orifice. The non-volatile liquid was tagged with approximately 10% sodium fluorescein tracer for subsequent determination of relative aerosol mass concentration. The size of the aerosol droplets was determined by impacting them on a glass slide coated with an oil-phobic film.

The droplets were then measured with an optical microscope. From knowledge of the degree of flattening of the oil droplets on the slide, the original spherical size of the droplets was calculated (Olanfigueroa et al. 1982). An Aerodynamic Particle Sizer (APS Model 3320, TSI, Inc., Shoreview, MN) was used to confirm that the size distribution of the test aerosol was near-monodisperse for all tests conducted in this study.

The aerosol thus generated was delivered into a mixing plenum (Figure 5.7) maintained at vacuum and constant aerosol concentration by exhausting excess test aerosol through a vacuum blower at a flow rate of 400 L/min. The test aerosol particles were usually not neutralized prior to introduction to the mixing plenum. However, some tests were conducted with the charge neutralizer to investigate the effect of enhancement of particle deposition due to electrostatic effects for different transport tube materials. Charge neutralization was done using a Kr-85 static charge neutralizer placed at the outlet of VOAG. Unless otherwise noted, tests were conducted with the non-neutralized aerosol particles.

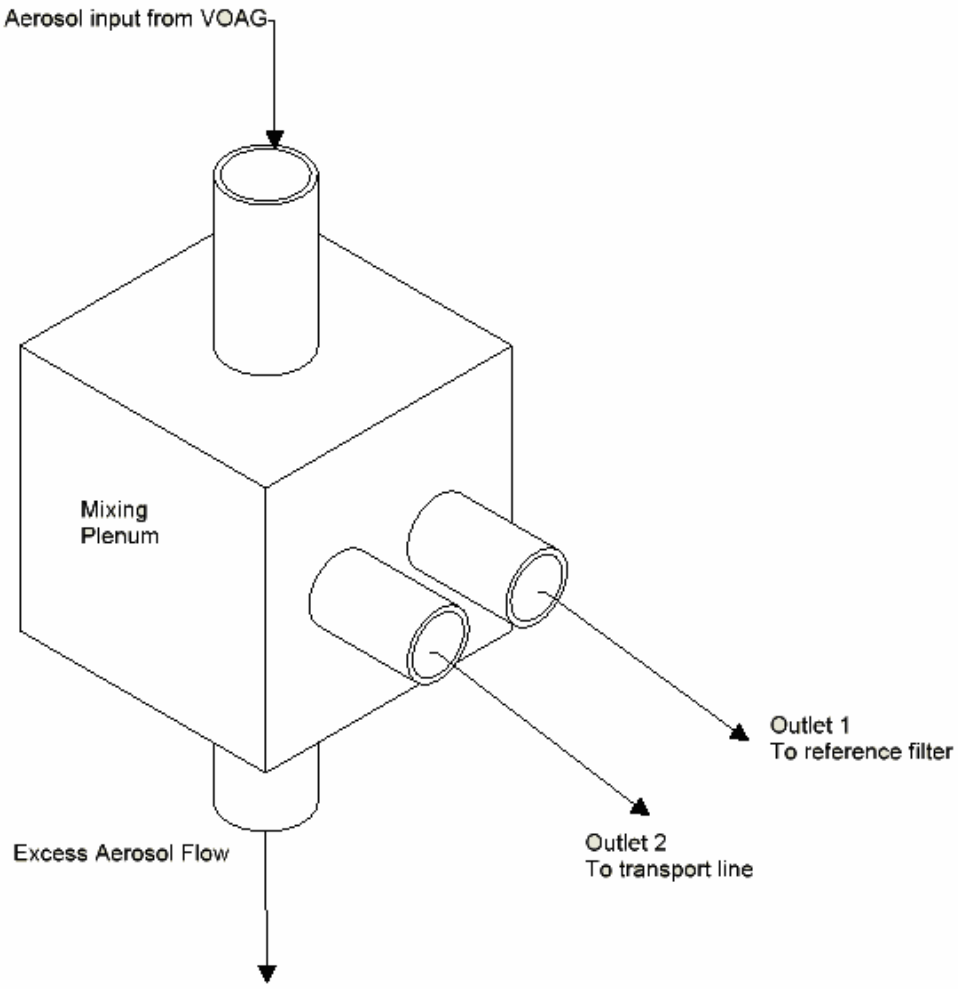

Figure 5.7: Schematic of the aerosol mixing plenum. The size of the mixing plenum was 10” (length) x 10” (width) x 15” (height).

During a test, aerosol was simultaneously drawn from the mixing plenum to a reference filter and through the transport line section under testing. Glass fiber filters (Type A/E or A/D Glass Fiber Discs, Pall Corporation, East Hills, NY) were placed at the outlet of the test section component and the reference outlet for collection of the test aerosol (mixing plenum outlets 2 and 1, respectively). By maintaining symmetry in the

mixing plenum with respect to outlets 1 and 2, and by setting the flow rate of the reference filter equal to that of the test section, the number concentration of particles collected on the reference filter should be equal to the number concentration entering the aerosol transport tube being tested. The transport efficiency was established by comparison of the relative aerosol mass collected on the filter placed at the outlet of the test component with that collected on the reference filter. A minimum of three replicate measurements were conducted to verify repeatability of each result.

The relative aerosol mass on each filter was determined by eluting the tracer from the filters in an alcohol/water solution and subsequent analysis of the fluorescent tracer concentration. The filters were allowed to soak a minimum of four hours in the solution to ensure complete dissolution of the fluorescent tracer prior to analysis. The relative concentrations of fluorescent tracer in the solutions were measured with a fluorometer (Model 450, Sequoia-Turner Corp., Mountain View, CA). By determination of the ratio of the relative concentration of the test filter solution by the relative concentration of the reference filter solution, the percentage of particulate mass penetrating through the transport line component was determined.

Particle charge measurement

Tests were performed to determine the average charge of particles generated by the vibrating orifice aerosol generator. Monodisperse oleic acid particles were generated using a VOAG (TSI Model 3450). The schematic of the experimental setup is shown in Figure 5.8. The particles were then passed through a drying column (with or without a neutralizer) and a mixing plenum.

A constant flow through the mixing plenum was maintained using a dilution air flow. The aerosol is drawn from the mixing plenum into the electrometer and the optical particle counter (OPC). The electrometer measures the net charge of the particles depositing on the filter inside the electrometer. The optical particle counter is used to measure the particle concentration. The flow rate through the optical particle counter was 58.6 L/min (2 cfm). The sampling volume was 0.2 cubic foot. The flow rate through the electrometer was around 30 L/min. Based on the net charge and the particle concentration, the average net charge on a particle can be found.

The experiment was run with no aerosol output from the VOAG to check for the background. The experiment was also run with only ethanol output from the VOAG at different frequencies of operation to estimate the effect of ethanol on particle charge. Finally, the experiment was run with different oleic acid particle sizes (4 to 15 μm AD) at two different dilution air flow rates.

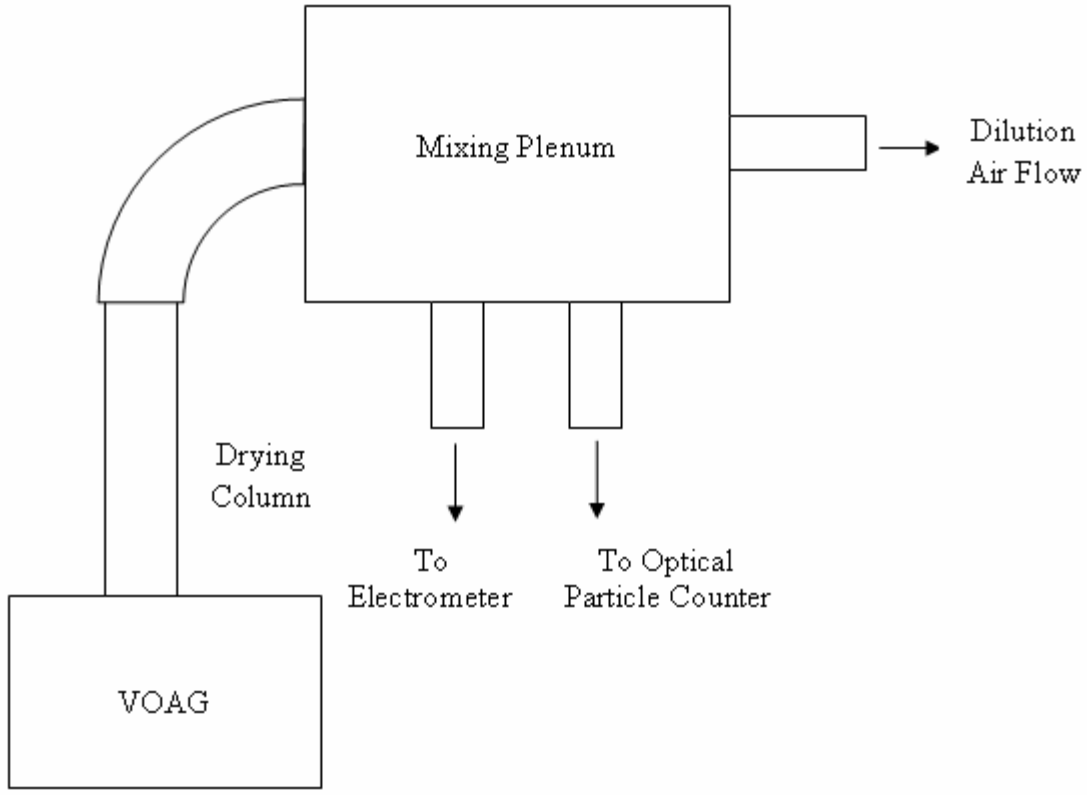

Figure 5.8: Schematic of the experimental setup for particle charge measurement.

Validation of equality of the aerosol output rate from test and reference ports of the aerosol mixing plenum

As described above, the penetration of aerosol through the transport components was calculated as the ratio of the aerosol concentration at the end of the transport line to the aerosol concentration on the reference filter. This calculation assumed that the aerosol concentration delivered from mixing plenum outlets 1 and 2 was equal. To verify equality of the aerosol concentration in the two outputs, tests were conducted with

10.5 µm AD particles. Nine test runs were conducted to measure the ratio of the aerosol collected from outlet 2 over outlet 1. The results show the ratio to be within experimental uncertainty of unity (Figure 5.9). For these comparison tests, the flow rate through both the outlets was 200 L/min.

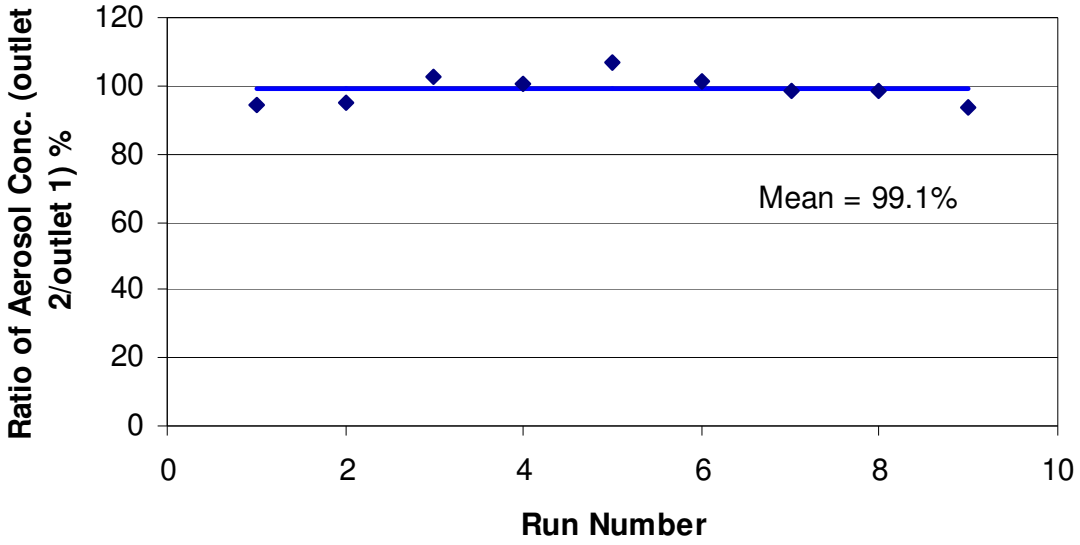

Figure 5.9: The ratio of the aerosol concentration through outlets 2 and 1 at a flow rate of 200 L/min through both outlet tubes.

Although it was desired to maintain equal flow rates in the test and reference outlets for all tests conducted, some exploratory experiments were conducted using non-equal flow rates in the interest of accelerating the collection of results. Situations arose in the course of the study in which the opportunity to conduct additional tests on either 200 or 400 L/min test components became available in which it was not possible to change the reference filter flow system without stopping the experiment. Because the

transport efficiency from the mixing plenum to the respective outlets should be near unity for either flow rate, it was expected that the ratio of aerosol mass delivered by each outlet to be very nearly proportional to flow rate. To confirm this assumption, additional tests were conducted to measure the aerosol concentration delivered by outlets 1 and 2 when the flow rates on either tube were reduced from 400 to 200 L/min. The results show that the concentration ratio to be near unity even when the flow rates were imbalanced (Table 5.4). However, the reference filter flow rate was set equal to the test component flow rate unless otherwise noted for all test results reported in this study.

Table 5.4: Comparison of the aerosol concentration delivered by outlets 1 and 2 for non-equal flow rates.

Flow Rate (L/min)		**Ratio of aerosol concentration (Outlet 2/Outlet 1)**	
Outlet 1	**Outlet 2**	**Mean (%)**	**Std. Dev. (%)**
200	200	99.1	4.3
400	400	99.1	3.7
200	400	99.0	4.7

Aerosol transport lines

Experiments were performed to determine the penetration of aerosols through a tube followed by an elbow (see Figure 5.10). The aerosol from outlet 1 entered into a 7.62 m (25 ft) horizontal tube followed by a 90° elbow. A filter was placed after the exit section of the elbow. The penetration of (nominally) 10 μm AD particles through four different types of tubing was determined viz., standard PVC, electrical conduit, aluminum conduit, and flexible vacuum hose with and without antistatic spiral wire. Experiments were conducted for different tube sizes at flow rates of 200 and 400 L/min.

The diameter of the tubing was chosen as described above; i.e. a nominal tube diameter of 1.5" was chosen for the flow rate of 200 L/min and a nominal diameter of 2" was used for the flow rate of 400 L/min. Also, additional tests were conducted with 1.25" nominal diameter flexible antistatic vacuum hose at both flow rates. These later experiments were conducted in order to estimate the transport efficiency of the dual collection system for a prior (non-optimized) configuration.

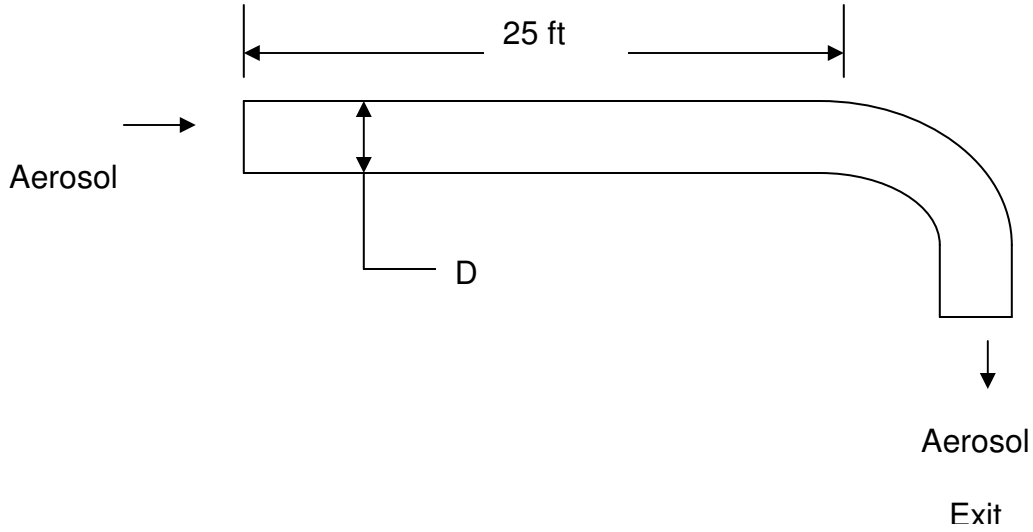

Figure 5.10: Schematic for the configuration of the tube setup for comparing penetration through tubes made of different materials.

For most of the tube materials, experiments were conducted both with and without a charge neutralizer to isolate the effect, if any, of residual static charge on transport efficiency. Using the charge neutralizer has the effect of neutralizing electrostatic charges on the test aerosol particles and therefore minimizes any enhancement of deposition due to electrostatic effects. As conducting tubes cannot support internal electric fields, it was anticipated that such tubes would show no difference in aerosol penetration with or without the charge neutralizer, but that non-conducting tube materials would have the possibility to show such an effect. The aim of these experiments was to determine if the use of non-conducting tube materials would be suitable for use as aerosol transport lines.

The results for penetration of 10 μm AD particles through tubes at 200 L/min are shown in Table 5.5. For the experiments without the charge neutralizer, 1.5" aluminum conduit had the highest penetration, 64 %, which was close to the theoretical penetration value of about 60% predicted by Deposition (McFarland et al. 2001) for Segment 1. Next highest was the 1.5" flexible vacuum hose with antistatic wiring (60%). The non-conducting tube materials all had lower particle penetration values: 1.5" flexible hose without the antistatic wiring (57 %), 1.25" flexible hose with antistatic wiring (50%) and 1.5" PVC tube (39%). For the experiments conducted with the charge neutralizer, the particle penetration through all the 1.5" nominal diameter tube materials collapsed to a value close to the theoretical prediction (around 60 %). The penetration through the 1.5" aluminum conduit and the 1.25" flexible hose with the antistatic wiring remained nearly the same whether or not the neutralizer was employed.

The penetration of 10 μm AD particles through the tubes at 400 L/min is shown in Table 5.6. As for the 200 L/min tests, the aluminum conduit and antistatic vacuum hose had the highest particle penetration when the test aerosols were not charge-neutralized at 66% and 69%, respectively. The 2" flexible vacuum hose without antistatic wiring had a penetration value of 49%, and the 1.25" flexible hose with antistatic wire had a penetration of only 5%. This later result underscores the need to use tube of sufficient diameter to prevent losses of particles due to inertial impaction.

Table 5.5: The penetration of 10 μm AD particles through the different tubes at a flow rate of 200 L/min with and without a neutralizer is tabulated.

Nominal size/material of tube	Penetration (%)				
	Without neutralizer		With Neutralizer		Deposition 2001a (McFarland et al. 2001)
	Mean	Std. Dev.	Mean	Std. Dev.	Mean
1.5" PVC	39	3.5	59	1.2	63.0
1.5" Flexible Hose	57	1.6	65	5.7	62.3
1.5" Aluminum	64	3.0	62	2.3	63.1
1.25" Flexible Hose	50	3.8	48	3.3	56.3
1.5" Flexible Hose with antistatic wire	60	1.1			62.3

Table 5.6: The penetration of 10 μm AD particles through the different tubes at a flow rate of 400 L/min with and without a neutralizer is tabulated.

Nominal size/material of tube	Penetration (%)				
	Without neutralizer		With Neutralizer		Deposition 2001a (McFarland et al. 2001)
	Mean	Std. Dev.	Mean	Std. Dev.	Mean
2" Flexible Hose	49	4.1			71.0
2" Aluminum	66	2.5			71.6
1.25" Flexible Hose	5	0.7	4	0.3	12.4
2" Flexible Hose with antistatic wire	69	3.9			71.4

It was concluded from the transport tube tests that conducting tube materials (i.e. either aluminum conduit or flexible vacuum hose with antistatic wiring) are necessary to prevent enhanced deposition of particles on tube wall due to electrostatic effects. Although it was not possible in this study to explore whether such effects would be actually realized in a postal sampling application, the conservative decision was made to consider only conducting or antistatic transport tube materials for further study.

As the dual collection transport system has no active control regulating the two sample inputs, there exists the possibility for the flow in the Segment 1 to be either above or below the design value of 200 L/min. To investigate the particle penetration at off-design conditions, the penetration through the 1.5" aluminum tubing and the 1.5" flexible vacuum hose with antistatic wiring was experimentally determined at flow rates of 100 and 300 L/min in addition to the design value. Figure 5.11 shows the penetration of 10.5 μm particles through 1.5" aluminum conduit and flexible vacuum hose with antistatic wire at flow rates of 100, 200 and 300 L/min.

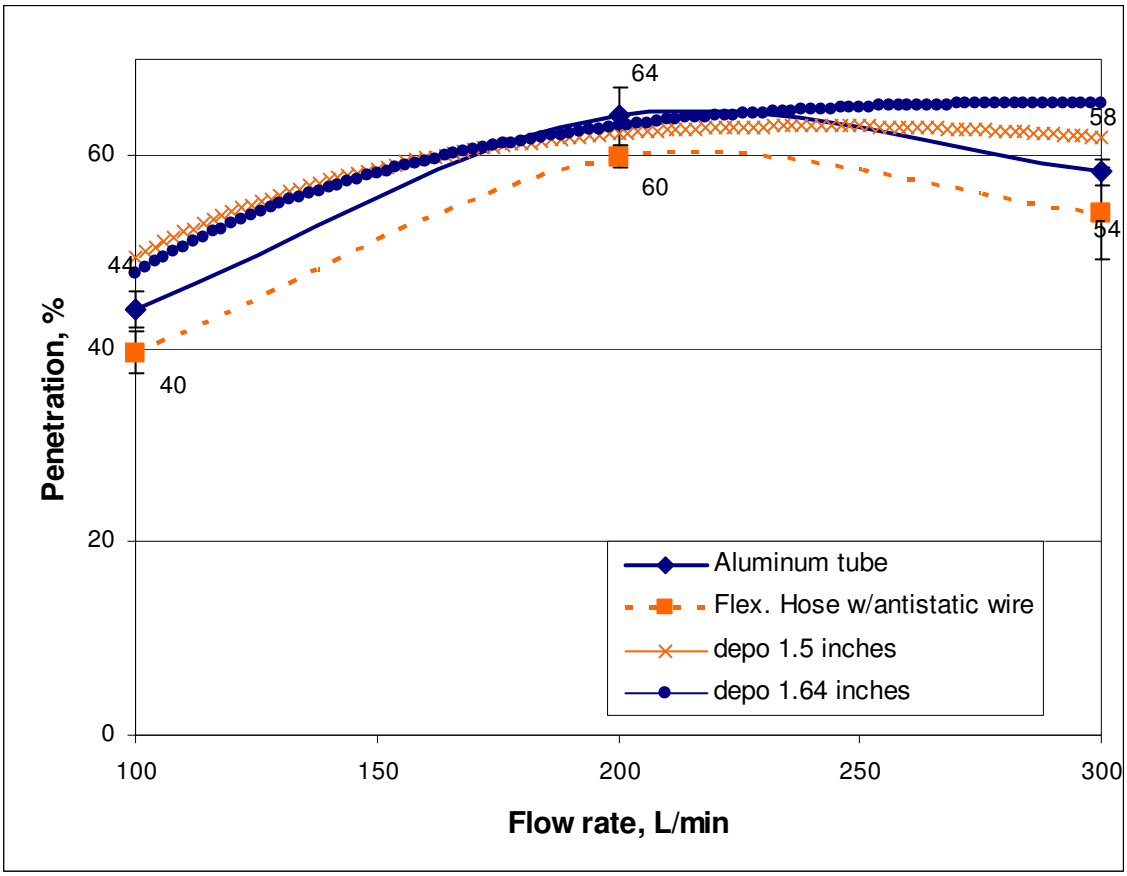

Figure 5.11: Particle penetration through 1.5" tubes for flow rates of 100, 200 and 300 L/min.

A sample of the 1.25" flexible antistatic vacuum hose used in field sampling at the downtown Houston, TX USPS facility was provided by Northrop Grumman for testing at the Aerosol Technology Laboratory. When this tube sample was examined upon arrival at Texas A&M University, it was found to exhibited significant, visible surface deposition of postal dust. Gravimetric analysis was performed on segments of the dirty tubing, and the mean areal density of the surface deposition was determined to

be 0.5 mg/cm^2 with a standard deviation of ± 0.03 mg/cm^2 for three samples of tubing analyzed.

Experiments were performed to study the effect of the described dust accumulation by comparison of particle penetration through 'clean' and 'dirty' condition 1.25" flexible hose. Two different configurations of the tube were studied: a U-bend and the second configuration and a straight horizontal tube (Figure 5.12). Both configurations had a total tube length of 1.52 m (5 ft) and had a quick-disconnect fitting at the entrance section.

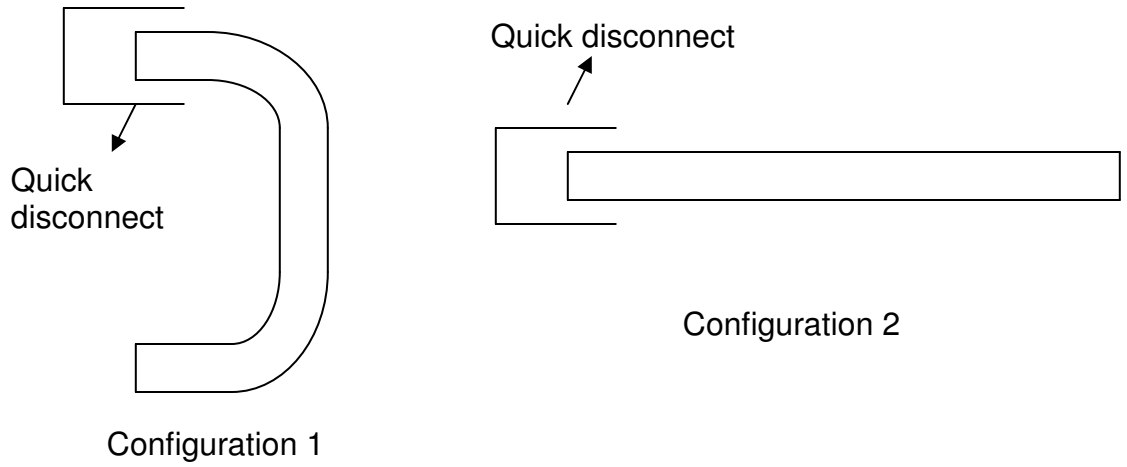

Figure 5.12: Tube configurations for testing clean and dirty tubes.

Configuration 1 was tested for a flow rate of 400 L/min and configuration 2 was tested at 200 L/min. Tests were conducted both with and without a charge neutralizer

with the results shown in Table 5.7. The results show that the particle penetration through the 'clean' tube was marginally higher than that for the 'dirty' tube, but the relatively small difference in penetration values and the fact that the dust accumulation on the test piece may represent only a light coating relative to heavier accumulations that may occur in the field situation suggest that it can only be concluded that dust accumulation can reduce the transport efficiency of the tubes.

Table 5.7: Results from testing clean and dusty tubes.

Serial #	Description	Component	Penetration (%)		Particle Size	Flow Rate
			Mean	Std. Dev.	µm	L/min
1	Configuration 1	Clean Tube	16	0.8	10.4	400
2		Dusty Tube	10	0.1		400
3		Dusty Tube	8	0.4	10.6	400
4		Dusty Tube w/ neutralizer	7	0.3		400
5	Configuration 2	Clean Tube	75	1.6	10.2	200
6		Dusty Tube	63	1.9		200
7		Dusty Tube w/ neutralizer	67	2.5		200

Characterization of cyclone cutpoints

MRI-designed cyclone

In addition to the Stairmand High-Efficiency cyclone described above, another cyclone variant based upon an MRI design currently in use in the postal sampling application was studied. This cyclone was originally intended for use at 400 L/min operation, and in order to modify the cyclone for use at 200 L/min while maintaining the same cutpoint, the MRI cyclone was Stoke-scaled for use at the lower flow rate. Upon inspection at the Aerosol Technology Laboratory, the MRI-designed cyclone was observed to have disproportionately small inlet and outlet tubes, and Deposition (McFarland et al. 2001) calculations of particle losses on these tubes suggested that it is the entrance and exit sections of the MRI cyclone that control the particle cutpoint rather than the cyclone body diameter.

In order to explore the possibility that the MRI cyclone could be modified to produce the desired cutpoint and regional deposition properties, retrofit inlet and outlet tubes of either 1.5” or 2.0” (depending upon whether the cyclone was interfaced to the 200 or 400 L/min flow) were fabricated for testing on the MRI cyclones (Figure 5.13).

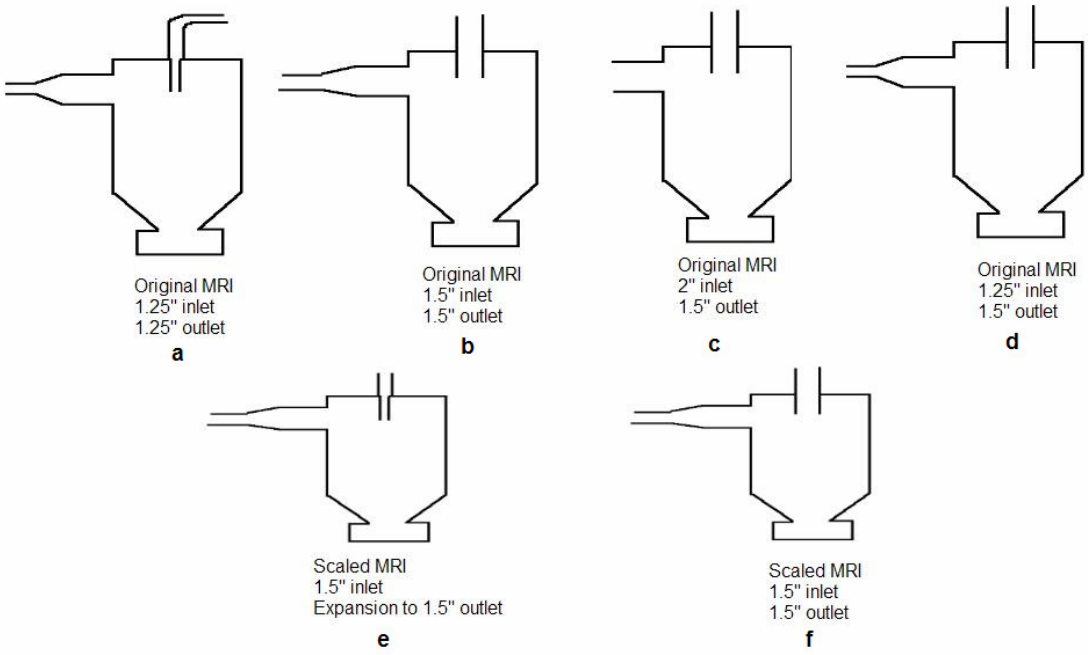

Figure 5.13: Schematic for the MRI cyclones with variant inlet/outlet connections.

Tests were conducted on different configurations of the MRI cyclones with monodisperse test particles. The results (Table 5.8) show that without any modification to the inlet or outlet, for both the original and scaled versions of the MRI cyclone (configurations a and e respectively), the cutpoint was well below 10 μm AD when the cyclone was operated at the design flow rate. However, when the outlet tube was replaced with the modified 1.5" diameter outlet, both the scaled and original MRI cyclones (configurations c and f respectively) had approximately a 10 μm AD cutpoint at the design flow rate.

Table 5.8: Particle penetration for the different variations of the MRI cyclone.

Label (ref. to Figure 12)	Cyclone	Particle Size (µm)			Flow Rate (L/min)
		5.6	10.7	15.3	
		Average penetration, % (stdev, %)			
a	**Original MRI**	13 (0.4)	9 (2.4)	--	400
a	**Original MRI**	--	11 (0.2)	--	200
d	**Original MRI 1.5" Outlet**	--	71 (1.1)	--	200
b	**Original MRI 1.5" Outlet 1.5" Inlet**	94 (0.9)	75 (1.3)	48 (1.7)	200
c	**Original MRI 1.5" Outlet 2" Inlet**	--	82 (4.3)	--	200
c	**Original MRI 1.5" Outlet 2" Inlet**	--	58 (2.1)	--	400
e	**Scaled MRI**	--	5 (0.4)	--	200
e	**Scaled MRI**	--	1 (0.1)	--	400
f	**Scaled MRI 1.5" Outlet**	100 (0.9)	50 (1.1)	20 (0.5)	200

Stairmand high-efficiency cyclone

The Stairmand cyclone described above was tested at a flow rate of 200 L/min for five different particle sizes from 5.1 to 13.8 µm AD. The experimentally determined cutpoint was calculated by performing a sigmoid curve-fit of the experimental data and

found to be 9.3 µm. A comparison of experimental results and the theoretical prediction is seen in Figure 5.14.

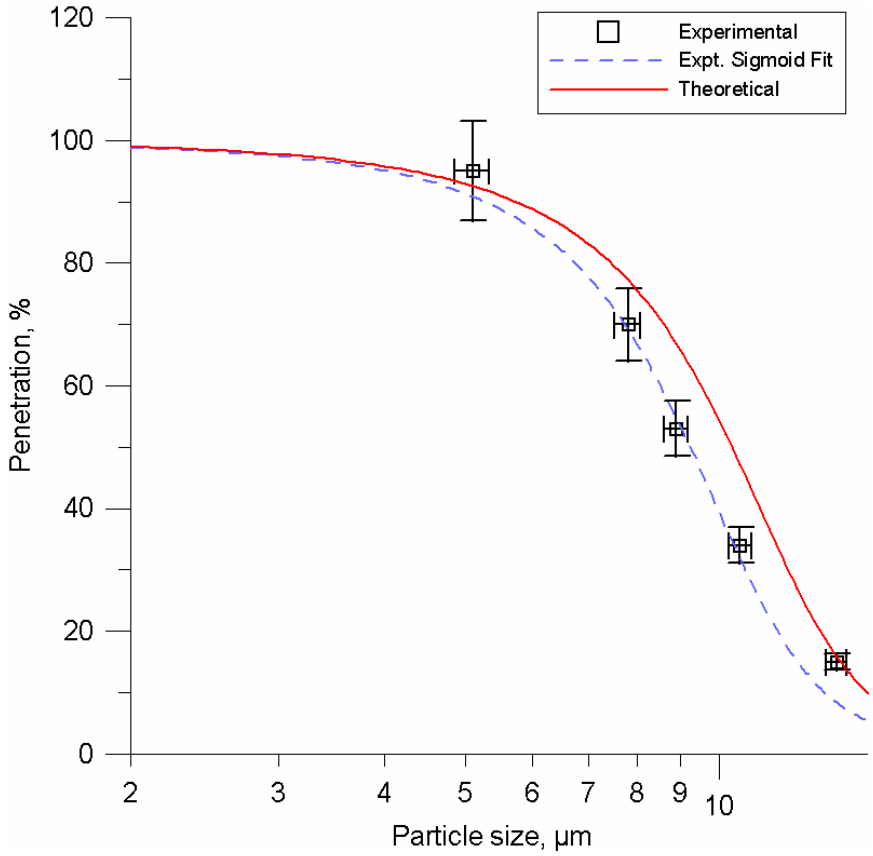

Figure 5.14: The penetration through the Stairmand High Efficiency Cyclone (Flow rate = 200 L/min).

Methods to increase the cyclone cutpoint

Two ways to increase the cutpoint of the Stairmand high-efficiency without significantly altering the geometry were investigated. The two methods to increase the cutpoint were changing the inlet expansion and the outlet tube diameter. It was found

that changing the inlet expansion does not significantly alter the cutpoint of the cyclone. The cutpoint of the cyclone can be changed to the desired value by changing the outlet tube diameter. To achieve a cutpoint of 10.5 μm, the cyclone outlet diameter has to be changed to 3.5" from the current value of 2.88".

The objective of this study was to suggest methods to increase the cutpoint of the high-efficiency Stairmand cyclone without significantly altering the cyclone geometry. The current cutpoint of the cyclone based on experimental results is 9.3 μm. The characteristic curve of the cyclone based on experimental results is shown in Figure 5.14. The dashed blue line is the sigmoid curve that has been fit to the experimental data. The solid red line is the theoretically predicted curve. The experimental data points and the error bars are also shown in the figure. The error bars were obtained using a Kline and McClintock error analysis. It is desired to increase the cutpoint of the cyclone to a value of about 10.5 μm. Two possible methods to increase the cutpoint of the Stairmand cyclone have been identified. They are:

1. Changing the half-angle of the inlet expansion
2. Changing the outlet tube diameter of the cyclone

The inlet expansion and the outlet tube have been identified in a schematic of the cyclone in Figure 5.15.

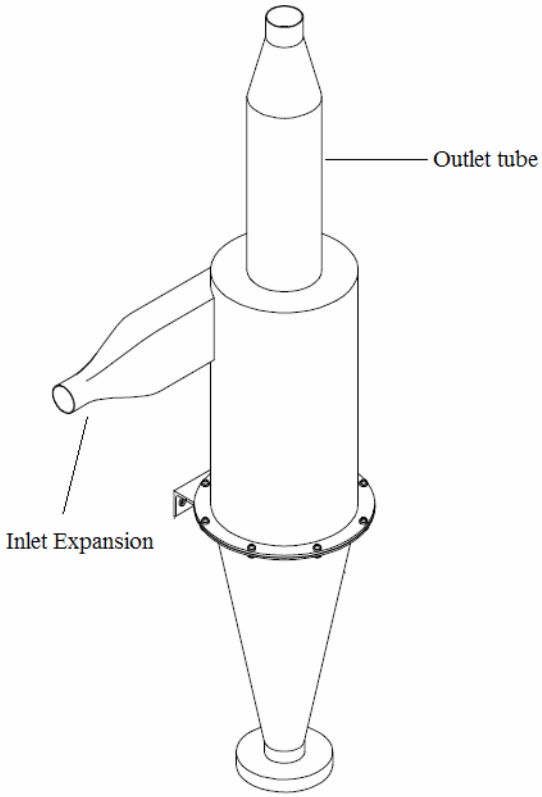

Figure 5.15: The Stairmand cyclone with the inlet expansion and outlet tube labeled.

The inlet expansion geometries are shown in Figure 5.16a – Figure 5.16c. Figure 5.16a shows the current expansion geometry. The inlet of the expansion has a circular geometry and the outlet of the expansion has a rectangular geometry as the inlet to the Stairmand cyclone is rectangular. The correlation developed for deposition in an expansion (Muyshondt 1995) was developed for expansions with circular inlets and outlets. Therefore the analysis for particle deposition in the expansion was done using a circular cross-section at the outlet. Figure 5.16b shows the analogical expansion, with a circular cross-section at the outlet of the expansion and diameter equal to the actual

hydraulic diameter at the outlet of the expansion. The half angle of expansion based on this geometry was 7.27°. The penetration through the expansion at a half-angle of 7.27° for a particle size of 10 μm AD is 87 %. The flow rate through the expansion is 200 lpm.

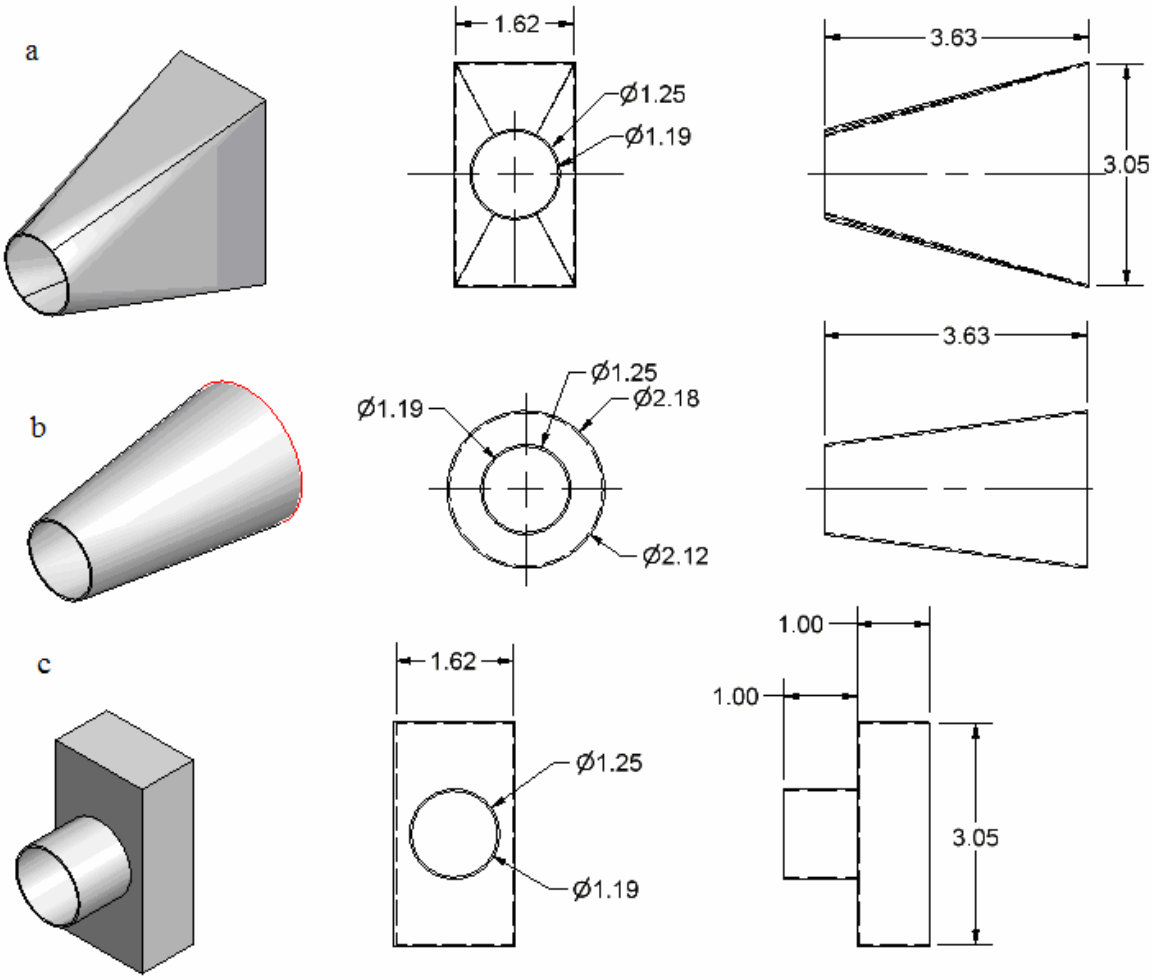

Figure 5.16: Inlet expansion geometries.

The penetration as a function of the half-angle of expansion has been plotted in Figure 5.17. The particle size is 10 μm, the flow rate is 200 lpm and the inlet and outlet diameters for the expansion are the same as for the geometry shown in Figure 5.16b. The penetration through the expansion has a minimum at a half-angle of expansion of about 12°. The penetration through the expansion increases as the half-angle increases for half-angle values lower than 12°. The opposite trend is seen for half-angle values higher than 12°. The penetration increases as the half angle value increases. Therefore to increase the penetration through the expansion we have two options, we can either decrease the half angle of expansion or we can increase the half angle of expansion. At a half-angle value of 90° (i.e. sudden expansion), the value of penetration is 89.7%. To achieve the same level of penetration with lower values of half-angles of expansion, the half-angle of expansion should be slightly less than 2°. At a half angle of expansion of 2°, the length of expansion is 13.3", which is not practical from a manufacturing and compactness perspective. Therefore, using a sudden expansion (see Figure 5.16c) might help improve the cutpoint of the cyclone.

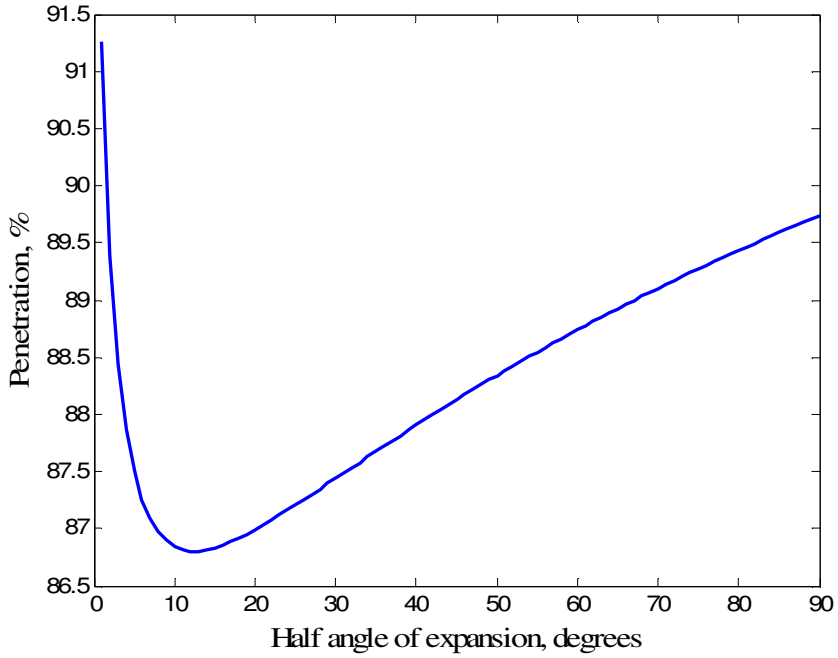

Figure 5.17: The penetration through the expansion at different half-angles of expansion.

The shift in the characteristic curve when we use the sudden expansion as opposed to the half-angle of expansion of 7.27° is shown in Figure 5.18. The cutpoint for the modified expansion is 9.35 μm. We do not get a significant increase in the cutpoint by modifying the inlet expansion.

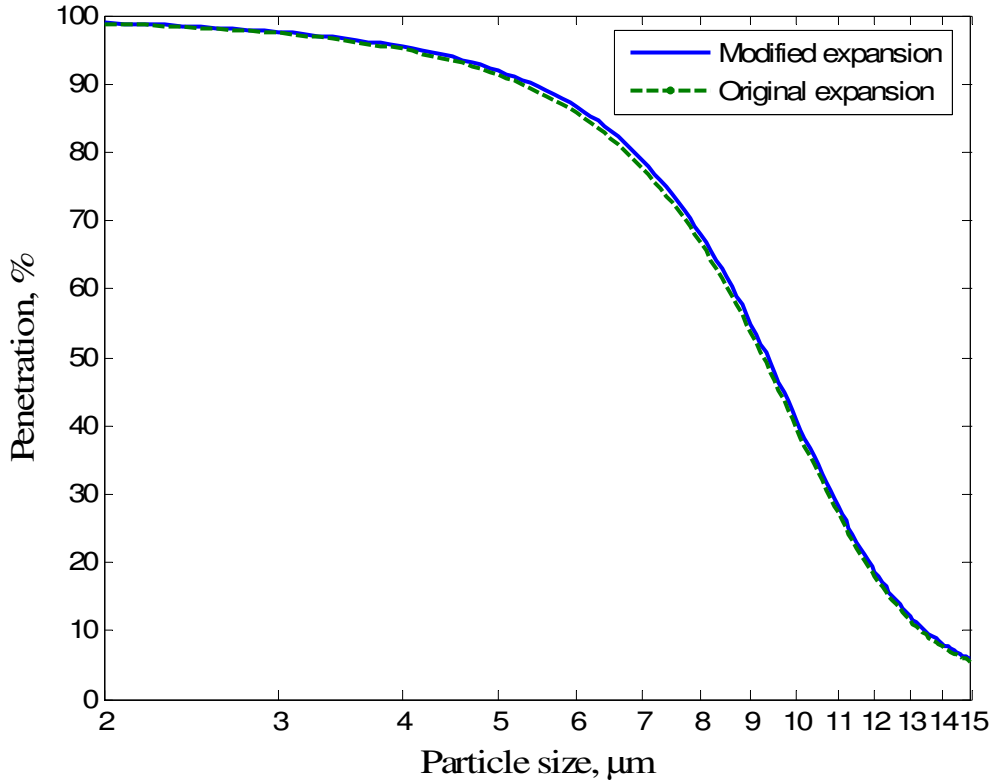

Figure 5.18: The cyclone characteristic curve for the modified and unmodified inlet expansion.

The effect of changing the outlet tube diameter on the cutpoint particle diameter (Moore 1991) is shown in Figure 5.19. The solid line is for the sudden expansion at the inlet and the dashed line is for the unmodified expansion at the inlet. To obtain a cutpoint diameter of 10.5 µm the outlet tube diameter has to be around 3.5".

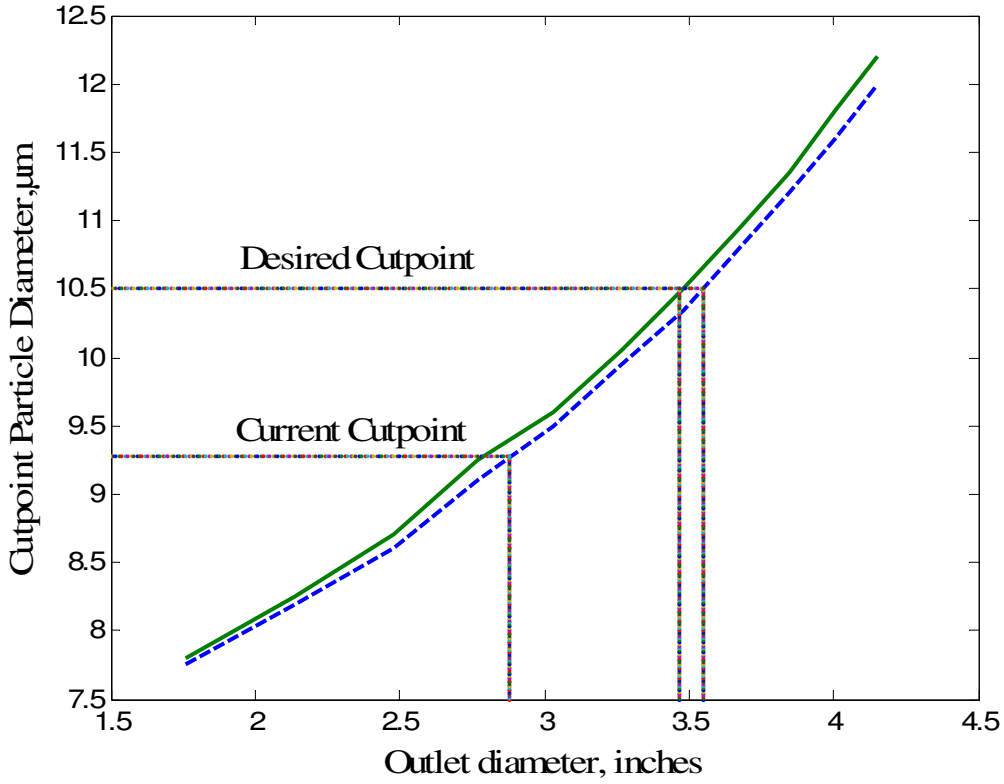

Figure 5.19: Cyclone cutpoint particle diameter as a function of the outlet diameter. The solid line is for the sudden expansion and the dashed line is for the unmodified expansion.

The schematics of the cyclone with the current and proposed outlet tube diameters are shown in Figure 5.20. The shift in the characteristic curve is shown in Figure 5.21.

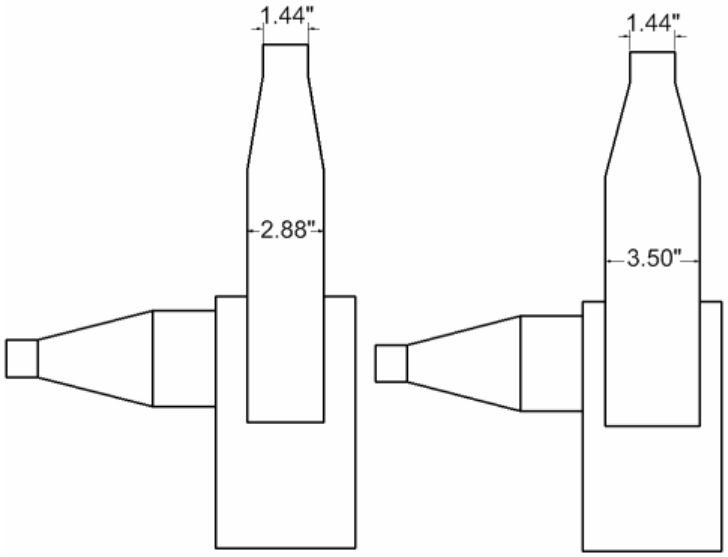

Figure 5.20: Current and proposed outlet tube diameters.

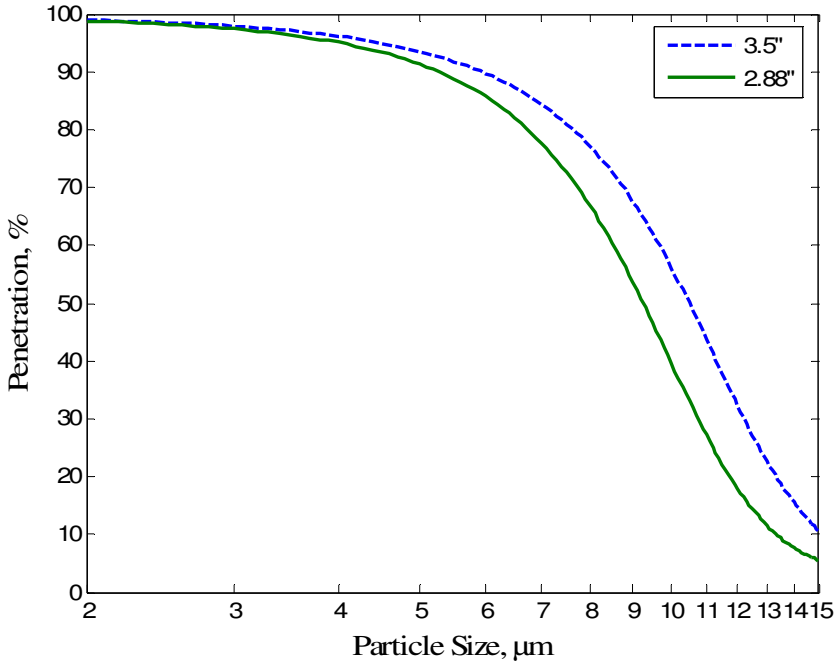

Figure 5.21: The cyclone characteristic curve for the current outlet diameter of 2.88” and the proposed outlet diameter of 3.5”.

Based on the study, the ideal way to increase the cyclone cutpoint is to increase the outlet tube diameter. To achieve a cutpoint of 10.5 μm, the outlet tube diameter has to be increased to 3.5" from 2.88".

Uncertainty analysis for Stairmand cyclone characteristic curve

The Kline and McClintock (Kline and McClintock 1953, Holman 2001) uncertainty analysis is discussed for the experiment to characterize the Stairmand high efficiency cyclonic filter. The aerodynamic particle diameter, D_a is calculated using Equation [5.2].

$$D_a = \frac{D_m}{f}\left(\frac{\rho_p}{\rho_0}\right)^{\frac{1}{2}} \qquad [5.2]$$

where D_m is the size measured using the microscope, f is the flattening factor, ρ_p is the particle density and ρ_0 is the reference density, i.e. 1 g/cm^3. The equation for the calculation of penetration through the cyclone is given by Equation [5.3].

$$P = \left(\frac{FV}{Qt}\right)_{cyclone} \Big/ \left(\frac{FV}{Qt}\right)_{reference} \qquad [5.3]$$

where F is the reading from the fluorometer, V is the volume of the solution used to dissolve the fluorescein, Q is the flow rate and t is the time for each run of the experiment.

The uncertainty values for all the parameters are given in Table 5.9. When the uncertainty is given as a percentage it denotes the relative uncertainty. All other uncertainties are absolute values. The uncertainty values for the individual parameters were either obtained from precision of the measuring instrument or from previous literature.

Table 5.9: Uncertainty values for the parameters.

Parameter	**Uncertainty**	**Parameter**	**Uncertainty**
D_m (Haglund 2003)	± 0.2 μm	F	± 5 % (Gupta 1999)
f (Olanfigueroa et al. 1982)	± 0.03	V	± 1 ml[1]
ρ_p (Haglund 2003)	± 0.01 g/cm^3	Q	± 3 %[2]
		t	± 1 s[3]

[1]Least count of measuring jar
[2]Manufacturer specified accuracy
[3]Operator response time

Based on the Kline and McClintock uncertainty analysis the relative uncertainty in the measurement of the particle size is given by Equation [5.4] and the relative uncertainty in the penetration through the cyclone is given by Equation [5.5]. In Equations [5.4] and [5.5] ε refers to the absolute uncertainty in each of the parameters.

$$\frac{\varepsilon_{D_a}}{D_a} = \left[\left(\frac{\varepsilon_{D_m}}{D_m} \right)^2 + \left(\frac{\varepsilon_f}{f} \right)^2 + \left(\frac{1}{2} \frac{\varepsilon_{\rho_p}}{\rho_p} \right)^2 \right]^{\frac{1}{2}} \qquad [5.4]$$

$$\frac{\varepsilon_P}{P} = \left\{ \begin{array}{l} \left[\left(\frac{\varepsilon_F}{F} \right)^2 + \left(\frac{\varepsilon_V}{V} \right)^2 + \left(\frac{\varepsilon_Q}{Q} \right)^2 + \left(\frac{\varepsilon_t}{t} \right)^2 \right]_{cyclone} \\ + \left[\left(\frac{\varepsilon_F}{F} \right)^2 + \left(\frac{\varepsilon_V}{V} \right)^2 + \left(\frac{\varepsilon_Q}{Q} \right)^2 + \left(\frac{\varepsilon_t}{t} \right)^2 \right]_{reference} \end{array} \right\}^{\frac{1}{2}} \qquad [5.5]$$

Substituting the uncertainty values from Table 5.9 into Equations [5.4] and [5.5], we can obtain the uncertainty in the measurement of penetration and aerodynamic particle size at the experimental data points. These uncertainty values are given in Table 5.10. The penetration data obtained at different particle sizes is the mean of at least three separate runs. The standard deviation of this data is also tabulated in Table 5.10. It can be seen that the experimental scatter in the data is lesser than the uncertainty in the measurement. For example, the uncertainty in penetration at 5.1 μm AD is ±8 % whereas the measurement standard deviation is only ±1.5 %. The experimental data points, the sigmoid curve fit for the experimental data points and the theoretical prediction for the cyclone characteristic curve has been plotted in Figure 5.14. The error bars represent the uncertainties in the measurement. We can see that the uncertainties in penetration decrease and the uncertainties in the particle size increase as the particle size increases. The penetration decreases as the particle sizes increases. This behavior can be explained by the fact that relative uncertainties remain fairly constant.

Table 5.10: Uncertainty in the measurement of penetration and aerodynamic particle size at the experimental data points.

Particle Size *µm AD*	**Uncertainty in particle size** *µm AD*	**Penetration** *%*	**Uncertainty in penetration** *%*	**Penetration Measurement Standard Deviation** *%*
5.1	±0.3	95	±8	±1.5
7.8	±0.3	70	±6	±2.0
8.9	±0.3	53	±5	±0.2
10.6	±0.4	34	±3	±1.1
13.8	±0.4	15	±2	±1.3

From the uncertainty values of penetration and particle size at the different data points, let us attempt to obtain the bounds for the cutpoint. The cutpoint of the cyclone (including the inlet expansion and outlet contraction) has been experimentally determined to be 9.3 µm AD. The slope of the characteristic curve at the cutpoint is -13.77 %/µm. We do not have the uncertainty values for the penetration and particle size at the cutpoint particle size. Therefore, let us assume that the uncertainties in penetration and particle size at the cutpoint particle size are the same as those at 8.9 µm AD; *viz.* ±0.3 µm AD for the particle size and ±5 % for the penetration.

The point A in Table 5.11 and Figure 5.22 is the experimentally measured cutpoint for the cyclone. Let us consider the worst case scenarios; the particle size could have been 9.0 µm AD and the penetration at this particle size could have been 45%. This is represented by point B. At the other extreme, the particle size could have been 9.6 µm AD and the penetration at this particle size could have been 55%. This is represented by point C.

Table 5.11: Bounds for the cyclone cutpoint.

Point	**A**	**B**	**C**	**D**	**E**
Particle Diameter, *μm AD*	9.3	9.0	9.6	10.0	8.6
Penetration, %	50	45	55	50	50

If we assume that the characteristic curve is linear in a small region around the cutpoint, then the slope of this line is -13.77 %/μm AD. The dashed lines in Figure 5.22 are lines with this slope passing through points A, B and C. From points B and C if we trace a path along the corresponding lines to a penetration value of 50 %, we will obtain the bounds for the cyclone cutpoint. From point B we obtain point E and from point C we obtain point D. The lower bound (point E) for the cyclone cutpoint is 8.6 μm AD and the upper bound (point D) for the cyclone cutpoint is 10.0 μm AD. Therefore the uncertainty in the cyclone cutpoint measurement is ±0.7 μm AD or ±8 % of the cutpoint size.

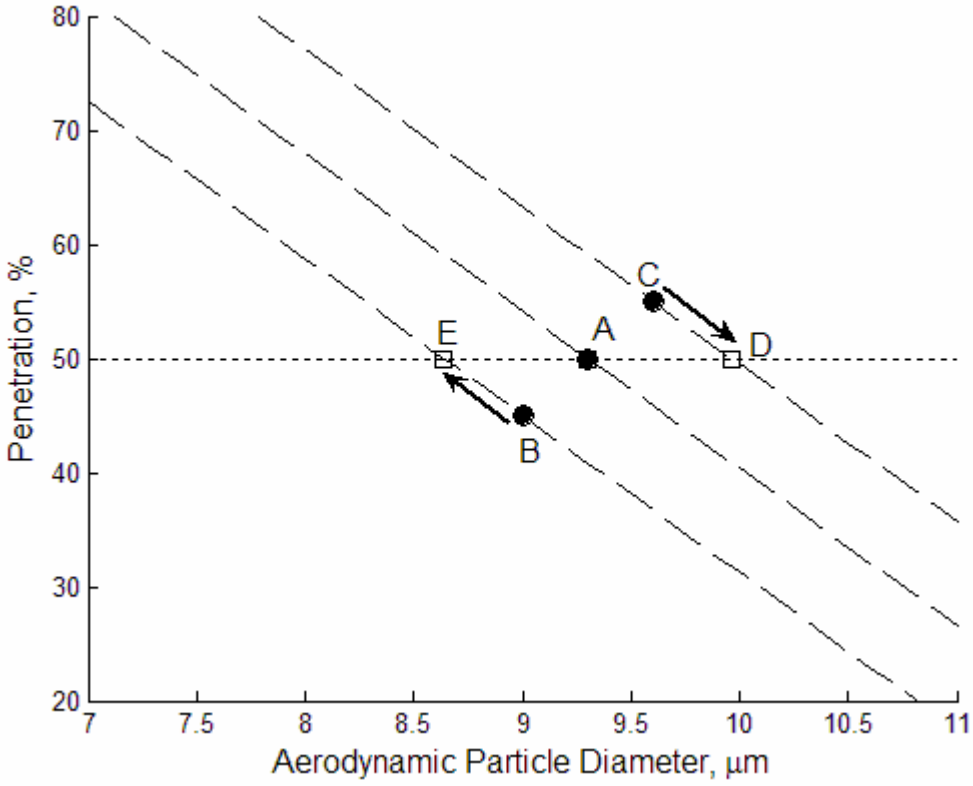

Figure 5.22: Graphical representation of the bounds for the cyclone cutpoint.

Characterization of flow combiner

A block-style flow combiner was fabricated and delivered by Northrop Grumman to the Aerosol Technology Laboratory for testing and (Figure 5.23). The block-style flow combiner had two, near-parallel 1.5" diameter inlet tubes that were joined internally into a single 2.0" diameter outlet tube. Because the cross-section changes are small and the flow combiner has no major changes in the gas flow direction (for this style of flow combiner, the elbows directing the sample flows into and out of

the combiner were analyzed as parts of the transport tubes), it was not expected that the combiner would contribute significant losses of the sampled particles.

The penetration through the block-type flow combiner was determined for 10.2 μm AD particles at a flow rate of 200 L/min through each of the two inlets. For this test, aerosol was input through only one of the two intake ports. The total penetration through the flow combiner was 95% with a standard deviation of ±1.8%.

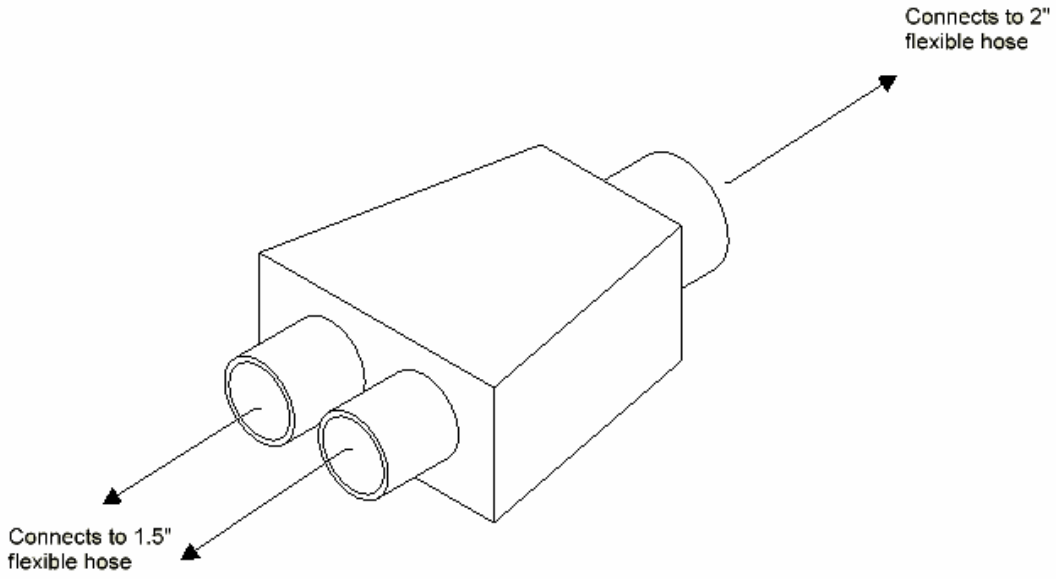

Figure 5.23: Schematic of the block-type flow combiner.

Particle penetration through the complete transport system

Transport efficiency of system without cyclones

Following testing of the individual components, experiments were conducted to characterize the transport efficiency of the combined Segment 1 and Segment 2 system using both aluminum conduit and antistatic flexible vacuum hose (Figure 5.24). In these experiments, the test aerosol was introduced into one of the two 200 L/min sample legs and the second sample leg flow rate was directly controlled with a regulated supply of forced air. This configuration allowed for testing at conditions of flow imbalance in the two Segment 1 sample lines.

Tests were conducted on the proposed transport system without the Stairmand cyclone to clearly measure and compare differences in the performance the tube sizes/materials selected for the transport system. The penetration through the complete transport system with aluminum conduit transport lines was determined to be 44% (± 0.9%) for 10.6 μm AD particles, only marginally lower than the theoretical value of 50% predicted by the Deposition (McFarland et al. 2001) calculation. The total penetration was slightly lower (38%) when antistatic vacuum hose was used for the transport lines, however the greater expense in material and installation costs probably may not warrant the use of rigid conduit over flexible vacuum hose in a field installation.

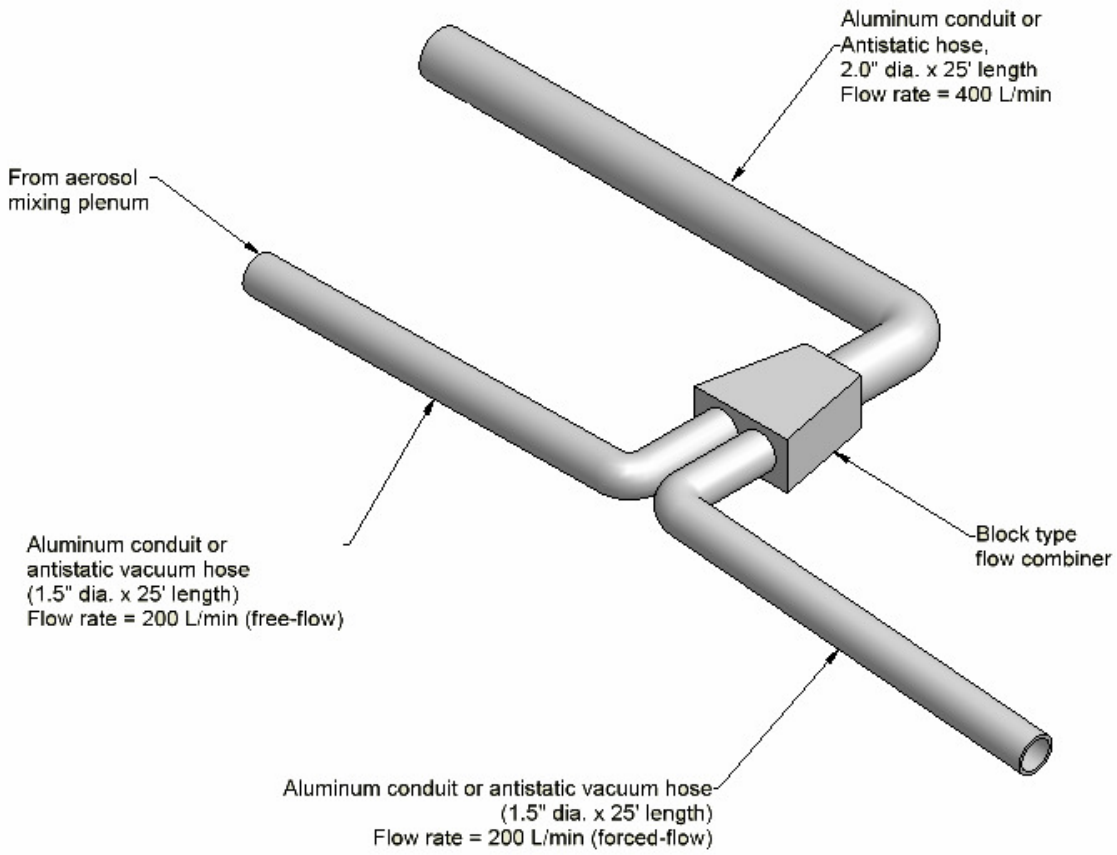

Figure 5.24: Schematic of transport system for aluminum conduit and flexible vacuum hose with antistatic wire.

Additional studies were conducted at off-design flow conditions and the results are shown in Table 5.12. There was only a marginal drop-off in transport efficiency when the sampling rate through a single leg of the system was increased or decreased by 100 L/min. Also, a set of tests was conducted in which the original MRI design cyclone was placed at the entrance of the system to demonstrate the influence on net transport efficiency of 10 μm AD particles. The results showed the net penetration to be only 1%

for this configuration, underscoring the need to design the debris removal cyclone with sufficiently high cutpoint to prevent loss of the sample of interest.

Table 5.12: Transport efficiency of 10 μm AD particles for the complete transport system using antistatic flexible vacuum hose for Segments 1 and 2 for off-design flow rates and prediction from Deposition 2001a (McFarland et al. 2001).

Serial #	**Configuration**	**Sample flow rate[1] (L/min)**	**Penetration (%)**		**Penetration (%)**
			Mean	**Standard Deviation**	**Deposition 2001a (McFarland et al. 2001)**
1	Whole Transport system w/o cyclones	100	30	1.1	33
2		200	38	2.7	42
3		300	34	2.1	41
4	Whole Transport System with Original MRI cyclone	200	1	0.03	

[1]The flow rate in Segment 1; the total flow rate through Segment 2 was 400 L/min for all tests

Transport efficiency of complete system with Stairmand High Efficiency Cyclone

In the final configuration, additional 1.25" antistatic flexible vacuum hose was added to the system to reflect the changes that would be necessary in a field installation to allow interface of the proposed transport system with the existing aspiration plenum

and the BDS. The schematic of the final transport system showing the types/sizes of antistatic flexible vacuum hose used in the different segments is shown in Figure 5.25. The transport system was tested both with and without a 1.25" antistatic vacuum hose at the outlet of Segment 2 (at the time of testing it was not known if the BDS could be interfaced directly with the 2" diameter outlet of Segment 2, desirable from the standpoint of maximum transport efficiency). The results are given in Table 5.13.

Table 5.13: Results for the transport system with the 2" to 1.25" contraction and the 1.25" tubing and without both of these components at the outlet of Segment 2.

Particle Size	**4.9 µm**		**10.2 µm**	
Configuration	**Penetration, %**		**Penetration, %**	
	Mean	**Standard Deviation**	**Mean**	**Standard Deviation**
With 1.25" flexible hose at the end	59	2.0	3	0.1
Without 1.25" flexible hose or contraction at the end	69	1.5	7	0.2

Comparison of the transport efficiency of the proposed, previous, and custom aerosol transport systems

The results for the original transport system with MRI cyclone (Figure 5.26) and the proposed transport system with Stairmand cyclone (Figure 5.25), with the contraction

fitting from 2" to 1.25" at the outlet of Segment 2, but not with the 1.25" tube itself) are tabulated in Table 5.14. In addition, tests were conducted with a system using antistatic vacuum hose that replicates the configuration used for tests conducted by Northrop Grumman at the ECBC test facility (Figure 5.27 and Table 5.15).

Table 5.14: Results for the final and the original transport system configuration.

Particle Size µm	**Penetration, %**			
	Original transport system with MRI cyclone		**New proposed transport system with Stairmand cyclone**	
	Mean	**Std. Dev.**	**Mean**	**Std. Dev.**
2.7	25	0.8	68	1.2
5.1	7	0.02	63	1.6
7.2			44	0.7
10.0			11	0.2

Table 5.15: Results for the transport system used during testing at ECBC.

Particle Size µm	**Penetration, %**	
	ECBC transport system with Stairmand Cyclone	
	Mean	**Std. Dev.**
2.6	73	3.3
5.1	68	2.6

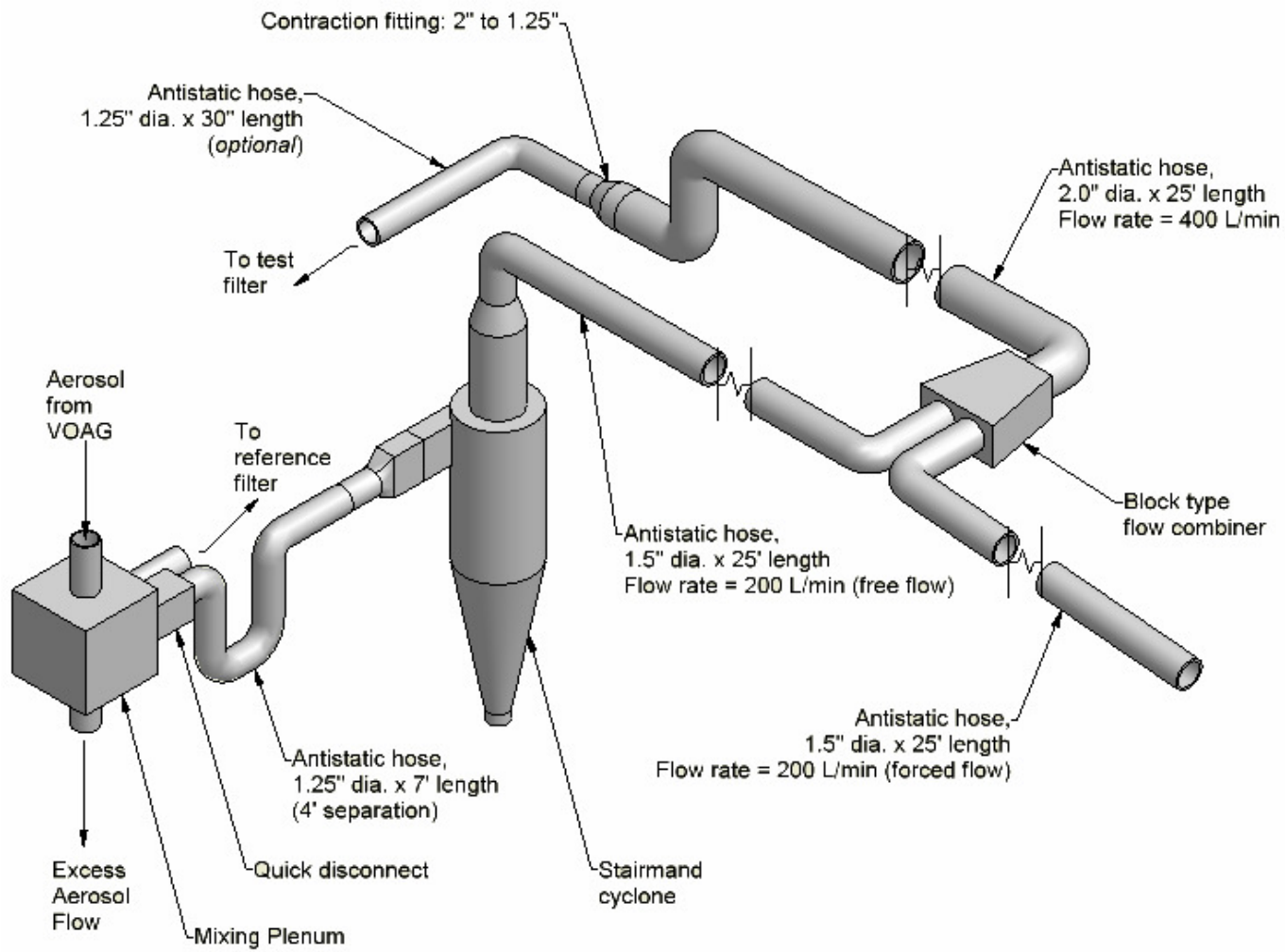

Figure 5.25: Schematic for the final proposed transport system.

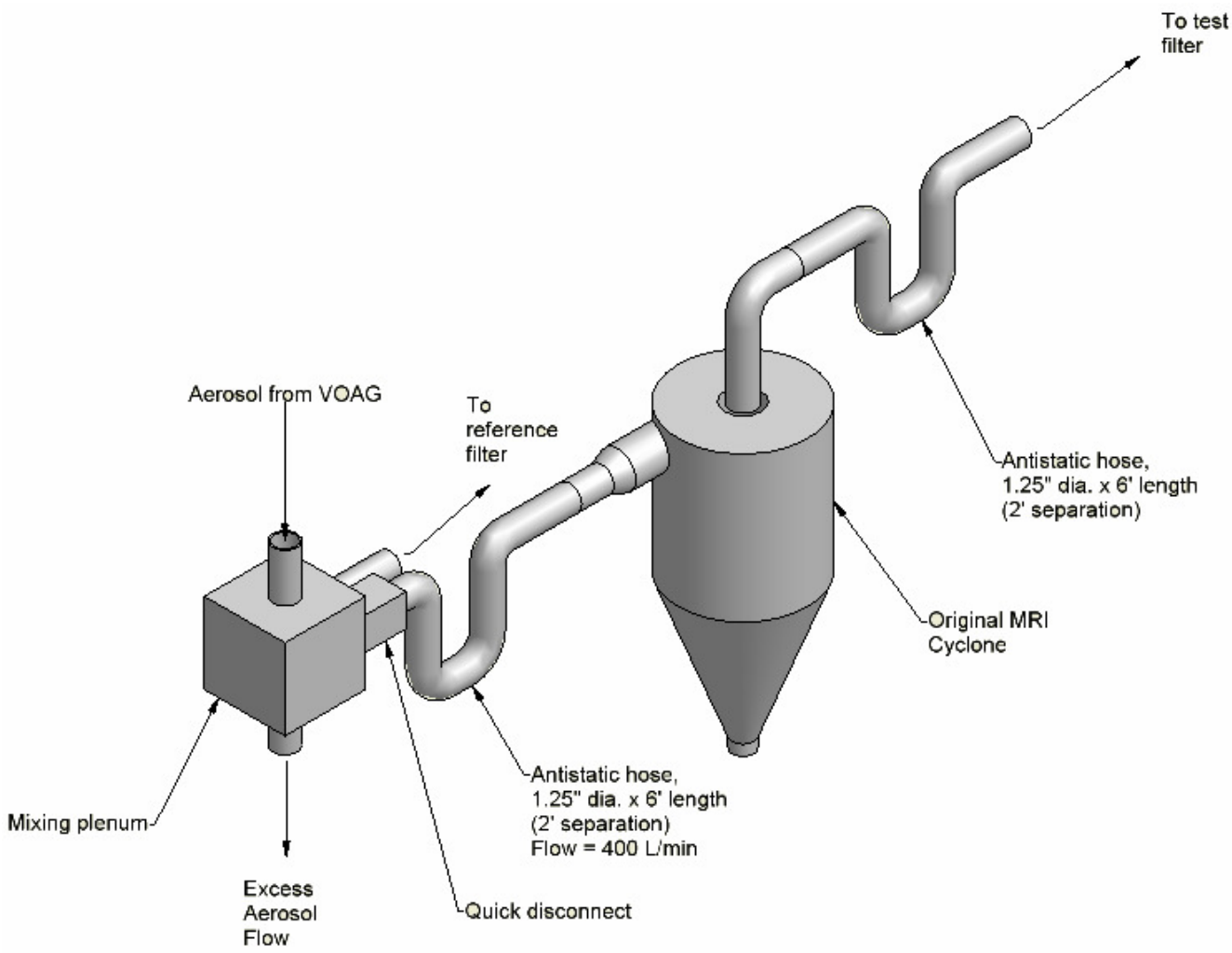

Figure 5.26: Schematic of the original MRI transport system.

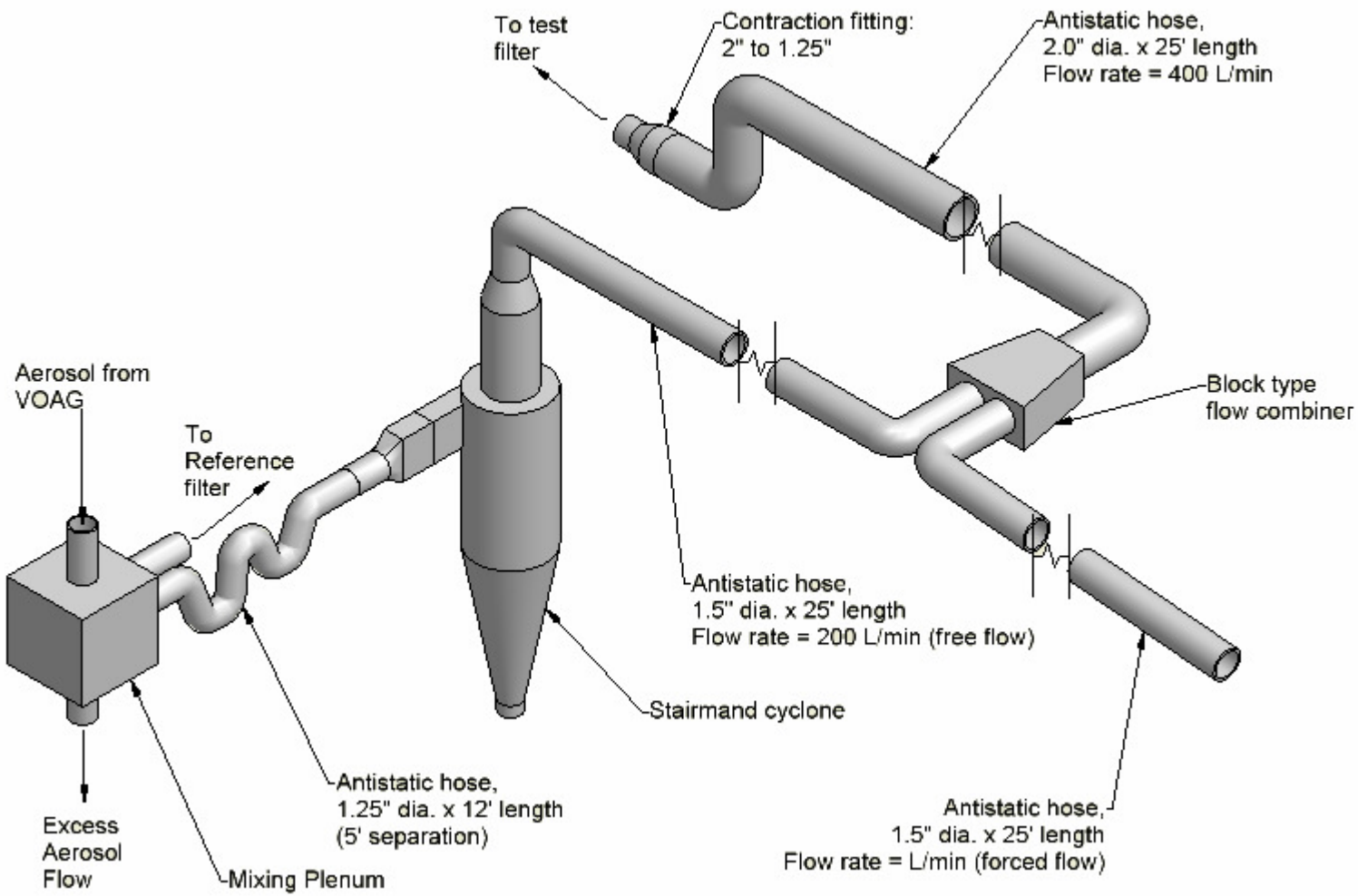

Figure 5.27: Schematic of the final ECBC test configuration.

Conclusions

The optimum diameter for different sections of the transport system was determined using Deposition 2001a (McFarland et al. 2001). A particle size of 11 µm AD was used for the analysis. The complete transport system was split into two segments. Segment 1 was the portion of the transport system from the outlet of the fractionation cyclone to the flow combiner. Segment 2 extended from the outlet of the flow combiner to the inlet of the BDS. The nominal flow rates through segments 1 and 2 were 200 L/min and 400 L/min respectively. The optimum diameter for the first segment was found to be 40 mm and the optimum diameter for the second segment was 55 mm. The corresponding optimum penetration values were 66.9% and 76.2% for the first and second segments respectively.

Commercially available tubes with the internal diameters closest to the optimum diameters were chosen. Four different pipe materials were selected for comparative testing, *viz.*, aluminum, PVC and flexible hose with and without antistatic wiring. The tubes were tested for the penetration of 10 µm AD particles at nominal flow rates of 200 L/min and 400 L/min. The 1.5" aluminum conduit had the maximum penetration (64%) at a nominal flow rate of 200 L/min followed by the 1.5" flexible tube with anti-static wiring; which had a penetration of 60%. At a nominal flow rate of 400 L/min the 2" flexible hose with antistatic wiring had the maximum penetration (69%), followed by the 2" aluminum tube with a penetration of 66%. The tubes were also tested with and without a charge neutralizer to study the effect of particle charges on penetration. While the penetration through the aluminum tube and flexible hose remained unaffected by

particle charge, the penetration through the PVC hose was highly dependent on the presence or absence of the neutralizer. Based on the amount of penetration and the effect of neutralizer on the penetration, aluminum and flexible hosing with antistatic wiring are ideal candidates for the transport system tubing. The flexible hose with antistatic wiring was ultimately chosen for the transport system due to the relative ease of its deployment and maintenance.

The 1.5" aluminum and flexible hose (with antistatic wiring) were tested at flow rates of 100 L/min and 300 L/min to cover for the possibility of off-design flow conditions. The penetration values at 100 and 300 L/min were lower than the penetration value at 200 L/min. For the flexible hose with antistatic wire, the penetration at 100, 200 and 300 L/min were 40%, 60% and 54% respectively. In the field, after a period of usage there is a layer of dust within the tubes in the transport systems. Comparison was made between tubes with a layer of dust inside and clean tubes. The results suggest that there is a reduction of transport efficiency with accumulation of dust inside the tubes.

A Stairmand/Lapple high-efficiency cyclone was designed for a cut-point diameter of 11 μm AD at a flow rate of 200 L/min. The cyclone body diameter was calculated to be 5.65" for the required cutpoint. The cutpoint of this cyclone and variants of the MRI designed cyclones were characterized experimentally. Non-scaled and scaled versions of the MRI designed cyclone with different inlet and outlet configurations were tested at 200 L/min and 400 L/min. The scaled MRI designed cyclone with 1.5" outlet had a cutpoint close to the desired cutpoint of 11 μm AD at 200 L/min. The Stairmand high efficiency cyclone was characterized experimentally at a flow rate of 200 L/min and the

cutpoint was found to be 9.3 μm AD. The cutpoint was lower than the design value of 11 μm AD due to particle losses at the inlet expansion and outlet contraction. The penetration through the flow combiner was also determined experimentally and was found to 95% for balanced flow of 200 L/min through each of the two inlets.

The particle penetration through the different variants of the complete transport system was experimentally determined for a number of particle sizes. The transport systems were tested in the presence and absence of a fractionating cyclone. For testing purposes, there was aerosol transport only through one of two legs joining at the flow combiner. The penetration through the transport system without cyclones was 44% for aluminum conduit transport lines and 38% when the flexible hose with antistatic wiring was used. The transport system with the flexible hose (antistatic wire) lines was also tested at off-design flow conditions. For flow rates of 100, 200 and 300 L/min through the particle carrying leg the penetration through the transport system for 10 μm particles was 30%, 38% and 34% respectively. The transport efficiency through a replica of the ECBC testing transport configuration was found to be 73% for 2.6 μm particles and 68% for 5.1 μm particles. The penetration through the original transport system with the MRI cyclone for 2.7 μm and 5.1 μm particles was 25% and 7% respectively. In comparison the proposed transport system with the Stairmand cyclone had a penetration of 68%, 63%, 44% and 11% for particles of size 2.7 μm, 5.1 μm, 7.2 μm and 10.0 μm respectively. The proposed transport system has better transport efficiency for a given particle size compared to the original MRI transport system.

Although the proposed transport system has optimized transport line diameters and a high efficiency Stairmand cyclone, there is a possibility to further increase the transport efficiency by incorporating minor changes. One such change would be to increase the diameter of the hose entering the BDS cabinet to 2” from 1.25”. This would prevent the transport losses associated with the small diameter of the tube and that due to the contraction form 2” to 1.25”. Another candidate for the increase in tube diameter (1.25” to 1.5”) is the section of the transport system from the mail sorting machine to the fractionating cyclone. There are also significant losses in the quick disconnect at the beginning of this section, which could be eliminated by using a different connector. We can altogether eliminate transport line losses if we employ a hydrosol transport system instead of an aerosol transport system. Such an arrangement would necessitate an aerosol to hydrosol transfer stage followed by the hydrosol transport system.

6. SUMMARY

Scalar mixing in straight tube and elbow geometries

One of the requirements for single point sampling of nuclear air emissions to demonstrate compliance with American National Standards N13.1 is the uniformity of momentum and effluent concentration in the sampling plane. The *a priori* prediction of the degree of uniformity for different flow geometries would be a useful tool for industries that need to demonstrate compliance with the standards. Presently, experiments with scaled models of the actual flow geometry are used for this purpose. Numerical simulations potentially offer a faster, more economical and accurate alternative for the *a priori* prediction of the amount of mixing. In a step towards this goal, numerical simulations were performed to study the turbulent mixing of a scalar species in single and double elbow flow configurations. The double elbow configurations studied included S and U shaped double elbows in a single plane. Different Reynolds Averaged Navier Stokes (RANS) and Large Eddy Simulation (LES) models were used to model the turbulence in the flow. The RANS models used for the simulation included standard, realizable, Renormalization Group (RNG) k-ε models and the Reynolds Stress Models. Conventional and dynamic Smagorinsky sub-grid scale models were used for the LES simulations. Wall functions were used to resolve the near wall boundary layer. These simulations were run with both two-dimensional and three-dimensional geometries. All the RANS simulations were steady simulations, while by definition the LES simulations were unsteady. The velocity and tracer gas concentration

Coefficient of Variations (COVs) were compared with experimental results. The COV, defined as the ratio of the standard deviation to the mean for a set of data, is a measure for the degree of uniformity of the data. The results from the LES simulations compared better with experimental results than the results from the RANS simulations. For example, at a distance of 10 diameters downstream from the exit plane of the single elbow, the concentration COV of 29% predicted using LES is closer to the experimentally predicted value of 20% than the value of 86% predicted using RNG k-ε. In addition, the level of mixing downstream of a S-shaped double elbow was higher than either the single elbow or the U-shaped double elbow due to the presence of counter rotating vortices. It can be concluded from the comparison of numerical results with experiments that, while LES may be an acceptable way to demonstrate compliance with standards, the present RANS models used for scalar mixing may not be acceptable.

Effect of particle charge and transport line conductivity on particle deposition

Penetration of neutralized and non-neutralized 10 μm aerosol particles through three different types of tubing was studied. The tubing used included standard PVC pipes, aluminum conduit and flexible vacuum hose. Two nominal tube sizes, *viz.* 1.25" (actual internal diameter (ID): 1.25” flexible hose) and 1.5" (actual ID: 1.62” aluminum conduit, 1.59” PVC tube, 1.5” flexible hose) were used in the study. A vibrating orifice aerosol generator was used to generate monodisperse oleic acid particles. A Kr-85 radioactive beta source was used to neutralize the particle charge. The particles neutralized using this method achieve a Boltzmann equilibrium charge distribution. The test section was a 25' long horizontal straight tube followed by an elbow. Tests were performed at a

nominal flow rate of 200 L/min. Penetration through the aluminum conduit was unaffected by the presence or absence of charge neutralization, whereas particle penetrations through the PVC pipe and the flexible hosing were affected by the amount of particle charge. Penetration through the 1.5” aluminum conduit for non-neutralized particles was 64% and penetration for neutralized particles was 62%. Penetration of non-neutralized particles through the 1.5” PVC tube and 1.5” flexible hose was 39% and 57% respectively. The penetration increased to 59% for the 1.5” PVC tube and the penetration increased to 65% for the 1.5” flexible hose after the particles were neutralized. The electric field in a space enclosed by a solid conductor is zero. Therefore charged particles within the conducting aluminum conduit do not experience any force due to ambient electric fields, whereas the charged particles within the non-conducting PVC pipe and flexible hose experience forces due to the ambient electric fields. This increases the deposition of charged particles compared to neutralized particles within the 1.5” PVC tube and 1.5” flexible hose. Particle charge did not have any effect on the penetration through the 1.25” flexible hose as the penetration was 50% without particle neutralization and nearly the same (48%) with particle neutralization. Effects responsible for particle deposition include inertial and electrostatic effects. As the tube internal diameter decreases velocity increases and inertial effects become more dominant than electrostatic effects. This can be observed in the reducing importance of particle charge in particle penetration through 1.5” PVC tube, 1.5” flexible hose and 1.25” flexible hose, in that order.

REFERENCES

Anand M, McFarland AR, Rajagopal KR. Gas mixing for achieving suitable conditions for single point aerosol sampling in a straight tube: Experimental and numerical results. Health Physics 84: 82-91; 2003.

ANSI/HPS-N13.1-1999. Sampling and monitoring releases of airborne radioactive substances from the stacks and ducts of nuclear facilities. New York: American National Standards Institute / Health Physics Society; 1999.

Biswas G, Eswaran V. Turbulent Flows: Fundamentals, Experiments and Modeling. New Delhi: Narosa Publishing House; 2002.

Buelow PEO, Venkateswaran S, Merkle CR. The effect of grid aspect ratio on convergence. AIAA Computational Fluid Dynamics Conference Pt. 2: 751-764; 1993.

Eggels JGM, Unger F, Weiss MH, Westerweel J, Adrian RJ, Friedrich R, Nieuwstadt FTM. Fully developed turbulent pipe flow: A comparison between direct numerical simulation and experiment. Journal of Fluid Mechanics 268: 175-209; 1994.

Fox RW, McDonald AT. Introduction to Fluid Mechanics. 5th ed. New York: John Wiley & Sons, Inc.; 2001.

Gupta R. Turbulent mixing and depostion studies for single point aerosol sampling. Ph.D. Dissertation, Department of Mechanical Engineering. College Station: Texas A&M University; 1999.

Gupta R, McFarland AR, Anand NK. Design and evaluation of the actinide packaging and storage facility (APSF) at Savannah River for compliance with EPA single-point aerosol sampling. College Station: ATL Report 3874/01/01/98/RG; 1998.

Haglund J. Two linear slot nozzle virtual impactors for concentration of bioaerosols. Ph.D. Dissertation, Department of Mechanical Engineering. College Station: Texas A&M University; 2003.

Han T, Ortiz CA, O'Neal DL, McFarland AR. Application of single-point representative air sampling to the Remote Handling Waste Facility (RHWF) stack. College Station: ATL Report 6833/05/15/03; 2003.

Han TW, O'Neal DL, McFarland AR, Haglund J, Ortiz CA. Evaluation of mixing elements in an L-shaped configuration for application to single-point aerosol sampling in ducts. HVAC&R Research 11: 657-672; 2005.

Holman JP. Experimental Methods for Engineers. 7th ed. Singapore: McGraw Hill; 2001.

Kline SJ, McClintock FA. Describing uncertainties in SingleSample experiments. Mechanical Engineering 75: 38; 1953.

Laufer J. The structure of turbulence in fully developed pipe flow. NACA Report 1174: 417-434; 1954.

Lin CH, Chang LFW. Evaluation of k-epsilon turbulence models in predicting developing turbulent flow in the inlet region of a pipe. Journal of the Chinese Institute of Engineers, Transactions of the Chinese Institute of Engineers,Series A/Chung-kuo Kung Ch'eng Hsuch K'an 19: 131-144; 1996.

McFarland AR, Anand M, Ramakrishna N, Rea JL, Thompson J. Deposition 2001a: An Illustrated User's Guide. College Station: ATL Report 6422/03/01/ARM; 2001.

McFarland AR, Anand NK, Ortiz CA, Gupta R, Chandra S, McManigle AP. A generic mixing system for achieving conditions suitable for single point representative effluent air sampling. Health Physics 76: 17-26; 1999a.

McFarland AR, Gupta R, Anand NK. Suitability of air sampling locations downstream of bends and static mixing elements. Health Physics 77: 703-712; 1999b.

Monclova LA, Forney LJ. Numerical simulation of a pipeline tee mixer. Industrial & Engineering Chemistry Research 34: 1488-1493; 1995.

Moore ME. Parametric study of air sampling cyclones. Ph.D. Dissertation, Department of Mechanical Engineering. College Station: Texas A&M University; 1991.

Moore ME, McFarland AR. Performance modeling of single-inlet aerosol sampling cyclones. Environmental Science & Technology 27: 1842-1848; 1993.

Muyshondt A. Aerosol deposition in transport lines. Ph.D. Dissertation, Department of Mechanical Engineering. College Station: Texas A&M University; 1995.

Olanfigueroa E, McFarland AR, Ortiz CA. Flattening coefficients for dop and oleic-acid droplets deposited on treated glass slides. American Industrial Hygiene Association Journal 43: 395-399; 1982.

Ramakrishna N, Das R, Chandra S, McFarland AR. Evaluation of an air sampling location in the HDB-8 stack of the Savannah River site. College Station: ATL Report 6242/01/01/NR; 2001.

Ramaprian BR. Review of experiments in periodic turbulent pipe flow. 12: 1-16; 1984.

Richardson M. A system for the continuous sampling of bioaerosols generated by a postal sorting machine. M.S. Thesis, Department of Mechanical Engineering. College Station: Texas A&M University; 2003.

Richman JW, Azad RS. Developing turbulent flow in smooth pipes. Applied Scientific Research (The Hague) 28: 419-441; 1973.

Rodgers JC, Fairchild CI, Wood GO, Ortiz CA, Muyshondt A, McFarland AR. Single point aerosol sampling: Evaluation of mixing and probe performance in a nuclear stack. Health Physics 70: 25-35; 1996.

Rudman M, Blackburn HM. Large eddy simulation of turbulent pipe flow. Second International Conference on CFD in the Minerals & Process Industries: 503-508; 1999.

U.S.EPA. Method 1 - Sample and velocity traverses for stationary sources, 40CFR60, Appendix A. Washington, DC: U.S. Government Printing Office; 2001.

Vijiapurapu S, Cui J. Large eddy simulation of fully developed turbulent pipe flow. ASME Heat Transfer / Fluids Engineering Summer Conference 2 A: 675-679; 2004.

Wang YQ, Derksen RW. Prediction of developing turbulent pipe flow by a modified k-epsilon-gamma model. AIAA Journal 37: 268-270; 1999.

VITA

Vishnu Karthik Vijayaraghavan was born in Trichy, India. He received his Bachelor of Technology degree in mechanical engineering from the Indian Institute of Technology, Madras, India in May 2001. He entered the mechanical engineering program at Texas A&M University in September 2001, and he received his Master of Science degree in August 2003. The author may be contacted at C-8-2, 5th Cross Road, IIT Madras, Chennai-600036, India.

The typist for this dissertation was Vishnu Karthik Vijayaraghavan.